Timescales and Characteristics of Magma Generation in Earth and Exoplanets

by

Karalee K. Brugman

A Dissertation Presented in Partial Fulfillment
of the Requirements for the Degree
Doctor of Philosophy

Approved April 2020 by the
Graduate Supervisory Committee:

Christy B. Till, Chair
Maitrayee Bose
Steven J. Desch
Richard L. Hervig
Everett L. Shock

ARIZONA STATE UNIVERSITY

August 2020

ABSTRACT

Volcanic eruptions are serious geological hazards; the aftermath of the explosive eruptions produced at high-silica volcanic systems often results in long-term threats to climate, travel, farming, and human life. To construct models for eruption forecasting, the timescales of events leading up to eruption must be accurately quantified. In the field of igneous petrology, the timing of these events (e.g. periods of magma formation, duration of recharge events) and their influence on eruptive timescales are still poorly constrained.

In this dissertation, I discuss how the new tools and methods I have developed are helping to improve our understanding of these magmatic events. I have developed a method to calculate more accurate timescales for these events from the diffusive relaxation of chemical zoning in individual mineral crystals (i.e., diffusion chronometry), and I use this technique to compare the times recorded by different minerals from the same Yellowstone lava flow, the Scaup Lake rhyolite.

I have also derived a new geothermometer to calculate magma temperature from the compositions of the mineral clinopyroxene and the surrounding liquid. This empirically-derived geothermometer is calibrated for the high FeO^{tot} (Mg# = 56) and low Al_2O_3 (0.53–0.73 wt%) clinopyroxene found in the Scaup Lake rhyolite and other high-silica igneous systems. A determination of accurate mineral temperatures is crucial to calculate magmatic heat budgets and to use methods such as diffusion chronometry. Together, these tools allow me to paint a more accurate picture of the conditions and tempo of events inside a magma body in the millennia to months leading up to eruption.

Additionally, I conducted petrological experiments to determine the composition of hypothetical exoplanet partial mantle melts, which could become these planets' new crust, and therefore new surface. Understanding the composition of an exoplanet's crust is the first step to understanding chemical weathering, surface-atmosphere chemical interactions, the volcanic contribution to any atmosphere present, and biological processes, as life depends on these surfaces for nutrients. The data I have produced can be used to predict differences in crust compositions of exoplanets with similar bulk compositions to those explored herein, as well as to calibrate future exoplanet petrologic models.

DEDICATION

For my grandfather, Harlan E. Sharer, who was clever, gentle, honorable, and kind. I hope I can one day bring the same curiosity and patience to my everyday life that he modeled for me. He once told me I gave him something to live for—he showed me how to live.

ACKNOWLEDGMENTS

TABLE OF CONTENTS

LIST OF TABLES

LIST OF FIGURES

Chapter 1

INTRODUCTION

Volcanism has been ongoing for $\sim$4 Ga on the rocky bodies of our solar system, even on those bodies not thought to have had Earth-style plate tectonics (Byrne 2019): the Moon, Mercury, and Mars were volcanically active in the past; studies suggest Venus may have experienced hotspot volcanism as recently as 250 ka to the present (Smrekar et al. 2010; Filiberto et al. 2020); and Io likely boasts active lava lakes (Lopes et al. 2018). The variety of volcanic regimes present on these bodies hints at the diversity that may be found on other rocky planets in the galaxy, and further motivates our desire to better understand the timescales and characteristics of magmatic events and reservoirs. This dissertation examines volcanism and magmatic conditions on Earth, as well as beyond our solar system, via three separate studies: development of a geothermometer for clinopyroxene found in high-silica magmatic systems (Ch. 2); modeling timescales of pre-eruptive events for Yellowstone post-caldera lavas, and suggestions for more robust error reporting when using diffusion chronometry (Ch. 3); and empirically determining the composition of magma produced by mantle partial melting in planets orbiting other stars (Ch. 4).

Volcanoes are how planets make new crust, usually at one of the three main types of terrestrial volcanic settings: convergent margin arc volcanoes like Mt. Fuji or Mt. Hood, mid-ocean ridges, or intraplate volcanism aka "hotspots" such as Yellowstone. In most melt-producing processes it is common for the mantle to be only partially melted. These "partial melts" may coalesce, rise towards the surface, and either erupt or stall in the crust. Erupted material cools on the planet surface, either under air or under water. Stalled magma cools more slowly as a plutonic body, but both extrusive and intrusive deposits become new surface or crust. Crucially, Earth-style plate tectonics is not required to produce new crust; for example, crust may also be generated after an impact if the event is large enough to induce melting in the mantle.

Understanding the composition of a planet's crust is fundamental to understanding chemical weathering, surface-atmosphere chemical interactions, and biological processes, as life depends on

these surfaces for nutrients. In order to determine the chemical composition of melts that can become these crusts, petrological experiments may be conducted to simulate melting in depths analogous to the crust and shallow mantle. In Chapter 4, I use these experiments to determine the composition of hypothetical exoplanet partial melts as a first step towards understanding the chemical and petrological relationships we may expect to find on these other worlds.

Volcanic eruptions are serious geological hazards; the aftermath of the explosive eruptions produced at high-silica volcanic systems often results in long-term threats to climate, travel, farming, and human life. One of these systems, Yellowstone caldera, is the site of some of the largest explosive eruptions in history, which blanketed much of North America in ash and produced erupted volumes 1120–9800 times that of the 1980 Mount St. Helens eruption (Christiansen 2001). Yellowstone caldera more commonly generates effusive rhyolitic eruptions—it produced > 20 of these large-volume flows since its last major explosive, caldera-forming eruption at Lava Creek Tuff at 0.63 Ma (Rivera et al. 2014, 2016; Matthews et al. 2015)—and future activity at Yellowstone is likely to also produce effusive rhyolitic eruptions (Christiansen et al., 2007; Girard and Stix, 2012). In the field of igneous petrology, the timing of magmatic events (e.g. periods of magma formation, duration of thermal events) and their influence on eruptive timescales are still poorly constrained but understanding these is necessary to improve hazard monitoring and forecasting. Diffusion chronometry—modeling the diffusive relaxation of chemical zoning to determine timescales of magmatic events—is a method that has gained popularity in the field of igneous petrology in the last decade. In Chapter 3 I use this method to examine the timescales of events recorded by different minerals from the same effusive lava flow, the Scaup Lake rhyolite from Yellowstone Caldera's third post-caldera cycle. I also examine the contribution of various sources of error to this method and make recommendations for error reporting, an aspect of diffusion chronometry that has been underexplored.

There is broad variability in clinopyroxene compositions in igneous systems, but a limited range of these compositions has been investigated experimentally. Scaup Lake clinopyroxene is distinctive in that it is moderately high in FeO^{tot} (Mg# $\approx$ 56) but very low in Al$_2$O$_3$ (0.53–0.73 wt%), a composition not well represented in experimental data, and thus not calibrated for when developing geothermometers. Natural clinopyroxenes of a similar composition are found in the Rattlesnake

Tuff ($\sim$0.35 wt% Al_2O_3), Bandelier Tuff (0.28–0.91 wt% Al_2O_3), Paektu Millenium eruption pumice (0.14–1.78 wt% Al_2O_3), and Pantelleria trachyte (0.25–0.72 wt% Al_2O_3) (Warshaw and Smith 1988; Streck 1994; Civetta et al. 1998; Iacovino et al. 2016). In Chapter 2 I present a new clinopyroxene-liquid geothermometer calibrated for the high-Fe, low-Al clinopyroxene found in high silica magmatic systems. Determination of accurate mineral temperatures is crucial to calculate magmatic heat budgets and to use methods such as diffusion chronometry. My new geothermometer lowers calculated temperatures by an average of over 80°C relative to prior assessments and improves error by more than half. Temperature calculated with this new geothermometer is more consistent with empirical data, modeling, and natural sample relationships, and indicates that clinopyroxene can be stable over a broad temperature range, often down to the solidus.

The final chapter of this dissertation, Chapter 5, suggests future avenues of research in the sub-disciplines discussed herein.

The substantiative chapters in this dissertation are intended to be independent manuscripts; they are published (Ch. 2) or in preparation for submission for publication (Ch. 3 & 4). The corresponding publication reference information is listed below in the order of the chapters presented.

Brugman, K.K., and Till, C.B. (2019) A low-aluminum clinopyroxene-liquid geothermometer for high-silica magmatic systems. American Mineralogist, 104, 996–1004. doi: 10.2138/am-2019-6842.

Brugman, K.K., Till, C.B., and Bose, M. Diffusion chronometry using a proxy to the growth-then-diffusion initial condition: The Scaup Lake rhyolite, Yellowstone. In preparation for Contributions to Mineralogy and Petrology.

Brugman, K.K., Phillips, M.G., and Till, C.B. Experimental determination of rocky exoplanet mantle solidi and melt compositions. In preparation for Journal of Geophysical Research: Planets.

References

Byrne, P.K. (2019) A comparison of inner Solar System volcanism. Nature Astronomy, 4, 321–327.

Christiansen, R.L. (2001) The Quaternary and Pliocene Yellowstone Plateau volcanic field of Wyoming, Idaho, and Montana, 145 p. U.S. Geological Survey, Reston, Va.

Civetta, L., D 'Antonio, M., Orsi, G., and Tilton, G.R. (1998) The geochemistry of volcanic rocks from Pantelleria Island, Sicily Channel: petrogenesis and characteristics of the mantle source region. Journal of Petrology, 39, 1453–1491.

Filiberto, J., Trang, D., Treiman, A.H., and Gilmore, M.S. (2020) Present-day volcanism on Venus as evidenced from weathering rates of olivine. Science Advances, 6, eaax7445.

Iacovino, K., Kim, J.-S., Sisson, T., Lowenstern, J., Ri, K.-H., Jang, J.-N., Song, K.-H., Ham, S.-H., Oppenheimer, C., Hammond, J.O.S., and others (2016) Quantifying gas emissions from the "Millennium Eruption" of Paektu volcano Democratic People's Republic of Korea/China. Science Advances, 2, 1–11.

Lopes, R.M.C., Gregg, T.K.P., Harris, A., Radebaugh, J., Byrne, P., Kerber, L., and Mouginis-Mark, P. (2018) Extraterrestrial lava lakes. Journal of Volcanology and Geothermal Research, 366, 74–95.

Matthews, N.E., Vazquez, J.A., and Calvert, A.T. (2015) Age of the Lava Creek supereruption and magma chamber assembly from combined ^{40}Ar/^{39}Ar and U-Pb dating of sanidine and zircon crystals. Geochemistry, Geophysics, Geosystems, 16, 2508–2528.

Rivera, T.A., Schmitz, M.D., Crowley, J.L., and Storey, M. (2014) Rapid magma evolution constrained by zircon petrochronology and ^{40}Ar/^{39}Ar sanidine ages for the Huckleberry Ridge Tuff, Yellowstone, USA. Geology, 42, 643–646.

Rivera, T.A., Schmitz, M.D., Jicha, B.R., and Crowley, J.L. (2016) Zircon Petrochronology and ^{40}Ar/^{39}Ar Sanidine Dates for the Mesa Falls Tuff: Crystal-scale Records of Magmatic Evolution and the Short Lifespan of a Large Yellowstone Magma Chamber. Journal of Petrology, 57, 1677–1704.

Smrekar, S.E., Stofan, E.R., Mueller, N., Treiman, A., Elkins-Tanton, L., Helbert, J., Piccioni, G., and Drossart, P. (2010) Recent Hotspot Volcanism on Venus from VIRTIS Emissivity Data. Science, 328, 605–608.

Streck, M.J. (1994) Volcanology and Petrology of the Rattlesnake Ash-Flow Tuff, Eastern Oregon. Oregon State University.

Warshaw, C.M., and Smith, R.L. (1988) Pyroxenes and fayalites in the Bandelier Tuff, New Mexico: temperatures and comparison with other rhyolites. American Mineralogist, 73, 1025–1037.

Chapter 2

A LOW-ALUMINUM CLINOPYROXENE-LIQUID GEOTHERMOMETER FOR HIGH-SILICA MAGMATIC SYSTEMS

Abstract

Several geothermobarometric tools have focused on clinopyroxene due to its prevalence in igneous rocks, however clinopyroxene produced in high-silica igneous systems is high in iron and low in aluminum, causing existing geothermometers that depend on aluminum exchange to fail or yield over-estimated temperatures. Here we present a new clinopyroxene-liquid geothermometer recommended for use in natural igneous systems with bulk $SiO_2 \geqslant 70$ wt%, which contain clinopyroxene with Mg# $\leqslant 65$ and $Al_2O_3 \leqslant 7$ wt%.

$$T(^\circ C) = 300 \Big[-1.89 - 0.601(X_{CaTs}^{cpx}) - 0.186(X_{DiHd_{2003}}^{cpx})$$
$$+ 4.71(X_{SiO_2}^{liq}) + 77.6(X_{TiO_2}^{liq}) + 10.9(X_{FeO}^{liq})$$
$$+ 33.6(X_{MgO}^{liq}) + 15.5(X_{CaO}^{liq}) + 15.6(X_{KO_{0.5}}^{liq}) \Big]$$

The new geothermometer lowers calculated temperatures by $\sim$85 $^\circ$C on average relative to Putirka (2008, Eq. 33) and reduces the uncertainty by a factor of two (standard error of estimate $\pm$20 $^\circ$C). When applied to natural systems, we find this new clinopyroxene-liquid geothermometer reconciles many inconsistencies between experimental phase equilibria and preexisting geothermometry results for silicic volcanism, including those from the Bishop Tuff and Yellowstone caldera-forming and post-caldera rhyolites. We also demonstrate that clinopyroxene is not restricted to near-liquidus temperatures in rhyolitic systems; clinopyroxene can be stable over a broad temperature range, often down

5

to the solidus. An Excel spreadsheet and Python notebook for calculating temperature with this new geothermometer may be downloaded from GitHub at http://bit.ly/cpxrhyotherm.

2.1   Introduction

Investigations of igneous systems often begin with an assessment of the temperature during eruption, crystallization, and/or magma storage, and geothermometers are generally calibrated to work with a broad range of rock types and mineral compositions. At least 40 clinopyroxene geothermometers have been developed, and many improve on past geothermometers or build on a previously published activity model. Two-pyroxene geothermometers are the most common type (e.g., Lindsley and Andersen 1983; Anderson et al. 1993; Sack and Ghiorso 1994; Putirka 2008; Liang et al. 2013) and take advantage of the temperature-dependent solvus of the pyroxene system. But these geothermometers necessitate the presence of equilibrium pairs of clinopyroxene and orthopyroxene in the host rock and are almost exclusively calibrated for diopside (Di; $CaMgSi_2O_6$), the low-Fe end-member of calcic clinopyroxene. Another type of geothermometer, clinopyroxene-liquid (e.g., Putirka 2008; Masotta et al. 2013), does not require co-crystallizing orthopyroxene and relies on the equilibria of Di, hedenbergite (Hd; $CaFeSi_2O_6$), and jadeite (Jd; $NaAlSi_2O_6$), the high-Al end-member of sodic clinopyroxene. However, geothermometers dependent on this equilibria are likely to be inaccurate if there is very little Al in the clinopyroxene and thus very little to no Jd component (which is calculated based on the estimated Al^{IV} rather than Na when Al^{IV} is low—see Table A.1). This caveat becomes significant when studying high-silica systems in which clinopyroxene is typically high in Fe (up to 30 wt% oxide) and low in Al ($<$ 2 wt% oxide; Fig. 2.1).

Unfortunately, the high-Fe, low-Al clinopyroxene from high-silica systems are not well represented in experimental data used to calibrate existing geothermometers, as the majority of experimental studies tend to explore Mg-rich augite to diopside, and in mafic rather than silicic systems. In silica-saturated systems, the major phases are Al-bearing plagioclase and alkali feldspar, and clinopyroxene have relatively low CaO; consequently, these clinopyroxene crystallize with almost all tetrahedral sites filled with Si rather than Al (Salviulo et al. 2000). A result of the historical sampling

bias is that in Al_2O_3-Mg# space, there is no overlap between the clinopyroxene found in many natural high-silica magmatic systems and the clinopyroxene used to calibrate two of the most commonly used clinopyroxene geothermometers, the Putirka (2008) clinopyroxene-liquid geothermometer and the MELTS two-pyroxene geothermometer (Sack and Ghiorso 1994) (Fig. 2.1). For many high-Fe, low-Al clinopyroxene, the most popular clinopyroxene-liquid geothermometer (Putirka 2008, Eq. 33) does not successfully calculate a temperature. When it does, it returns systematically high temperatures, up to 170 °C greater than the conditions of high-Fe, low-Al clinopyroxene-saturated experiments, indicating that this geothermometer is not well suited for this restricted mineral composition. Thus, if we wish to utilize clinopyroxene in our thermal investigations of high-silica systems such as Long Valley, Yellowstone, and Valles Calderas, it is prudent to develop a new geothermometer that is calibrated for the clinopyroxene found in these eruptive products.

Here we present a new clinopyroxene-liquid geothermometer, calibrated using data from experiments on high-silica systems that crystallized high-Fe, low-Al clinopyroxene, that is able to consistently calculate temperatures where other geothermometers fail and reproduce experimental temperatures to within 17 °C. Also, for high-silica system experiments below 850 °C—the temperature range of most interest for these systems—the new clinopyroxene-liquid geothermometer offers a fivefold decrease in the deviation between calculated and actual experimental temperatures as compared to the Putirka (2008, Eq. 33) geothermometer (± 20 vs. ± 110 °C). We apply the geothermometer to a series of silicic igneous systems to examine the effect of these adjusted temperatures on our petrologic understanding of phase relations and magma storage conditions.

2.2 Methods

To calibrate a new geothermometer, a data set of clinopyroxene and glass compositions was compiled from recent experimental studies on high-silica magmatic systems (Table A.2). The selected studies were conducted at 675–1025 °C and 75–503 MPa and yielded experimental run products with a bulk silica content of >70 wt% and clinopyroxene with $\leqslant$ 7 wt% Al_2O_3 and Mg# from 2.5–
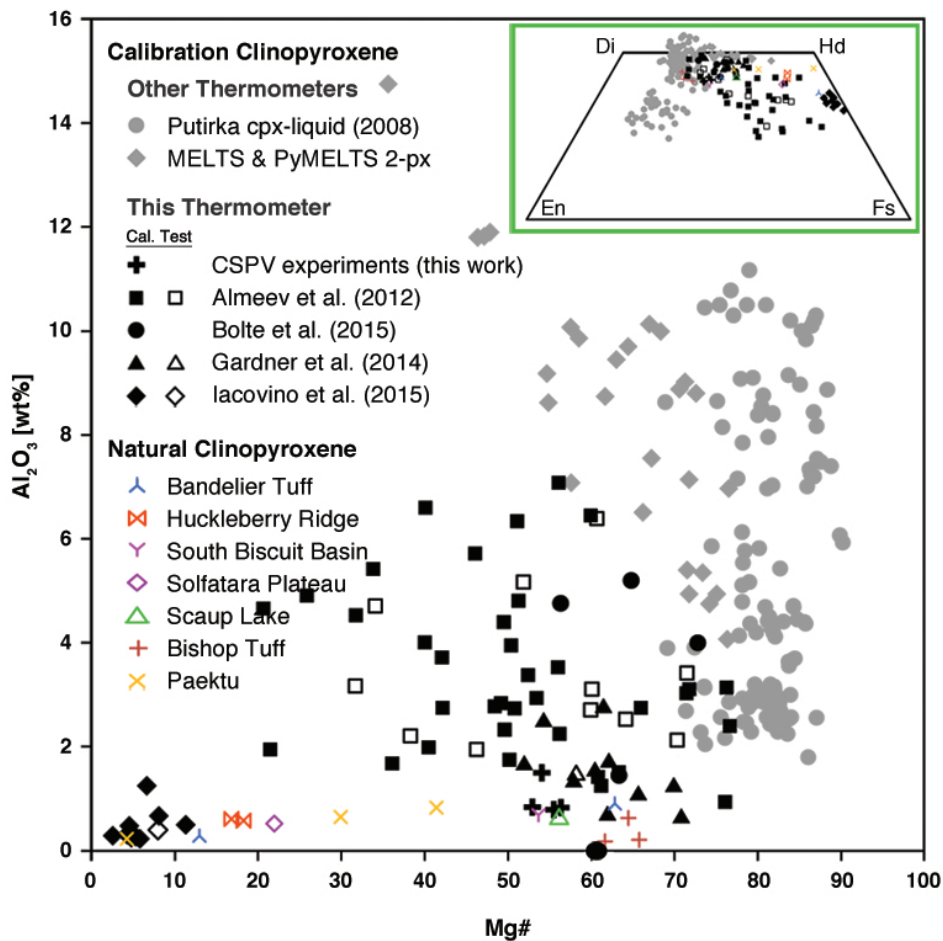
Figure 2.1: Clinopyroxene compositions from experiments and silicic igneous systems. Gray symbols: clinopyroxene used to calibrate existing geothermometers (Sack and Ghiorso 1994; Putirka, personal communication). Black solid and matching black outlined symbols: clinopyroxene used to calibrate and test the new clinopyroxene-liquid geothermometer (Almeev et al. 2012; Gardner et al. 2014; Bolte et al. 2015; Iacovino et al. 2015). Colored symbols: compositions of clinopyroxene from natural high-silica magmatic systems (Hildreth 1977; Warshaw and Smith 1988; Sisson 1991; Girard and Stix 2009; Gardner et al. 2014; Iacovino et al. 2016). Inset: Pyroxene quadrilateral of the same clinopyroxene as the main figure.

77 (Fig. 2.1, Table A.2). These data included relatively few experiments performed between 750–875 °C, therefore new hydrothermal cold-seal pressure vessel (CSPV) experiments (4) were conducted in this temperature range to supplement the experiments from the literature.

Table 2.1: Experiment starting glass

Oxide	wt%	st.dev.
SiO2	74.59	2.73
TiO2	0.23	0.15
Al2O3	13.75	1.96
Cr2O3	0.01	0.01
FeOtot	1.75	0.71
MnO	0.04	0.03
MgO	0.19	0.09
CaO	1.03	0.34
Na2O	2.55	0.37
K2O	5.15	0.19

EPMA data; n = 14.

For the new experiments, the starting material, the Scaup Lake rhyolite from Yellowstone Caldera (sample 12CTYC-01), was twice powdered, homogenized, and glassed at 1400 °C for 30 min in a 1 atm vertical furnace at the Experimental Petrology and Igneous Processes Center (EPIC) at Arizona State University (ASU) (Table 2.1). Single Scaup Lake clinopyroxene crystals with intact, euhedral faces were hand-picked under stereo microscope from a $\leqslant$ 1 mm size fraction of mineral separates to mitigate compositional heterogeneity due to subtle intracrystalline zoning. These clinopyroxene were used as seed crystals in the whole-rock powder. The CSPV experiments were conducted at the Massachusetts Institute of Technology experimental petrology lab in Stellite No. 25 cold-seal hydrothermal pressure vessels with filler rods, and were heated in horizontal, split-tube furnaces. Temperatures were monitored using chromel-alumel thermocouples. Experiments were H_2O-saturated and buffered at NNO using double Au capsules with powdered Ni-NiO buffer in the outer capsule. The pressure for all experiments was 1 kbar, run durations were ~16–24 days (Table 2.2), and experiments were quenched by blowing compressed air over the vessels while at pressure. After quenching, inner and outer capsules were weighed before and after they were pierced and dried in a warming

oven for 10 min. If mass was lost after piercing and drying, often in conjunction with water visible upon piercing, the capsule was presumed to be H_2O-saturated.

Table 2.2: CSPV experimental conditions

Experiment	T ($^{\circ}$C)	P (kbar)	t (hrs)
SCL01-4	750	1	573
SCL01-3	775	1	572
SCL01-5	800	1	385
SCL01-1	825	1	410

The CSPV experimental products (Table A.2) were mounted in epoxy in wells drilled into 1″ aluminum rounds and then measured on the JXA-8530F EPMA at ASU's Eyring Materials Center using an accelerating voltage of 15 kV and beam current of 15 nA. Beam sizes were 1 mm for clinopyroxene and 10 mm for glass. Time-dependent intensity (TDI) correction was applied to glass measurements of Na, K, and Si to mitigate migration of light elements away from the electron beam.

2.3 Results

2.3.1 CSPV Calibration Experiments

Four successful experiments (750–825 $^{\circ}$C, 1 kbar) were glassy with bubbles and included amphibole, indicating the charges remained H_2O-saturated for the run duration. All experiments crystallized clinopyroxene (Fig. 2, Table A.2) and contained equilibrated, unzoned seed crystals, with variable minor amounts of alkali feldspar, plagioclase, Fe-Ti oxides, and quartz.

Accepted clinopyroxene data were sourced from crystals that showed no zoning in backscattered electron (BSE) images. These data were from either newly grown crystals or rims of equilibrated seed crystals (easily distinguished by size: $< 50~\mu$m vs. $\geqslant 100$ mm) that differed from their starting composition (Table A).
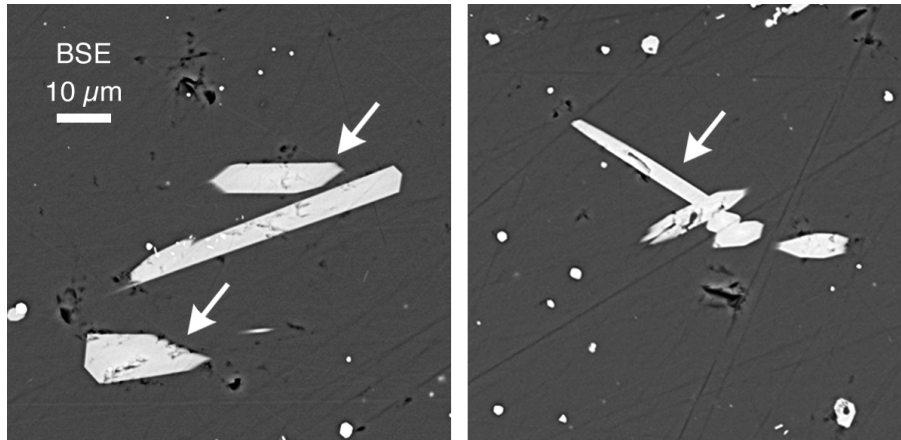
Figure 2.2: Clinopyroxene crystallized during CSPV experiment SCL01-3 (775 °C, 1 kbar, 572 h). Crystals used for calibration indicated with white arrows. Gray background is glass.

2.3.2 Geothermometer Calibration and Performance

The CSPV experiment data were combined with the previously published experimental data. Sixty-four of these data points constitute the geothermometer calibration data set of high-Fe, low-Al clinopyroxene and glass pairs (Table 2.3, Table A.2). Thirteen data points were not included in the calibration data set and instead were set aside as a test data set to check the efficacy of the geothermometer. To preserve temperature variation in the calibration data, a data point was excluded from the calibration data set and reserved for the test data set only if the experiment was conducted at the same temperature as other experiments in that particular study.

Table 2.3: Calibration dataset experimental conditions

Locality	n	T (°C)	P (kbar)
Scaup Lake rhyolite	4	750–825	1
Cougar Point and Indian Batt rhyolites[a]	36	875–1025	2.0–5.03
Blacktail Creek rhyolite tuff[b]	4	790–850	2
Late-erupted Bishop Tuff pumice[c]	10	700–800	1.0–2.0
Paektu Millennium comendite pumice[d]	10	675–750	0.5–1.5

Composition data from [a] Almeev et al. (2012)   [b] Bolte et al. (2015)
[c] Gardner et al. (2014)   [d] Iacovino et al. (2015) are available in Table A.2.

The calibration data set clinopyroxene and glass compositions (60 previously published and 4 from this work) were converted to clinopyroxene components and liquid cation fractions following the procedure used in previous clinopyroxene-liquid geothermometers (Putirka et al. 2003 and references therein) (see Table A.1 for the full procedure). Backward step-wise regression was used to determine which parameters best explained the variation in experimental temperatures. Significant parameters were selected based on statistics of significance from preliminary linear regressions on the calibration data set. These initial linear regressions were performed with T as the dependent variable, and one of two groups of parameters as independent variables. Parameter Group A was comprised of those calculated for use in the Putirka (2008, Eq. 33) geothermometer and Group B encompassed Group A as well as calculations of cations based on 6 O atoms for clinopyroxene (Table A.1). A parameter progressed to the next stage of the process if the 95% confidence interval for its coefficient did not include 0.

These limited sets of parameters were used in new linear regression trials to create new candidate geothermometer equations. These equations were evaluated for efficacy by their ability to return accurate temperatures from the test data set [e.g., R^2 and standard error of estimate (SEE)]. Ultimately, the parameters from both clinopyroxene and liquid that most improved regression statistics were sourced from Group A, resulting in the geothermometer equation:

$$
\begin{aligned}
T(^\circ C) = 300\Big[&-1.89 - 0.601(X_{CaTs}^{cpx}) - 0.186(X_{DiHd_{2003}}^{cpx}) \\
&+ 4.71(X_{SiO_2}^{liq}) + 77.6(X_{TiO_2}^{liq}) + 10.9(X_{FeO}^{liq}) \\
&+ 33.6(X_{MgO}^{liq}) + 15.5(X_{CaO}^{liq}) + 15.6(X_{KO_{0.5}}^{liq})\Big]
\end{aligned}
\tag{2.1}
$$

$X_{DiHd_{2003}}^{cpx}$ represents the Di plus Hd components of clinopyroxene as described in Putirka et al. (2003), and $X_{SiO_2}^{liq}$ represents the cation fraction of SiO_2 in the liquid.

The new geothermometer reproduced the temperatures of the test data set well, with an R^2 value of 0.95 as compared to R^2 = 0.72 for temperatures calculated using the Putirka (2008) clinopyroxene-liquid geothermometer (using Putirka 2008 Eq. 33 in concert with the reported experimental *P*) (Fig.
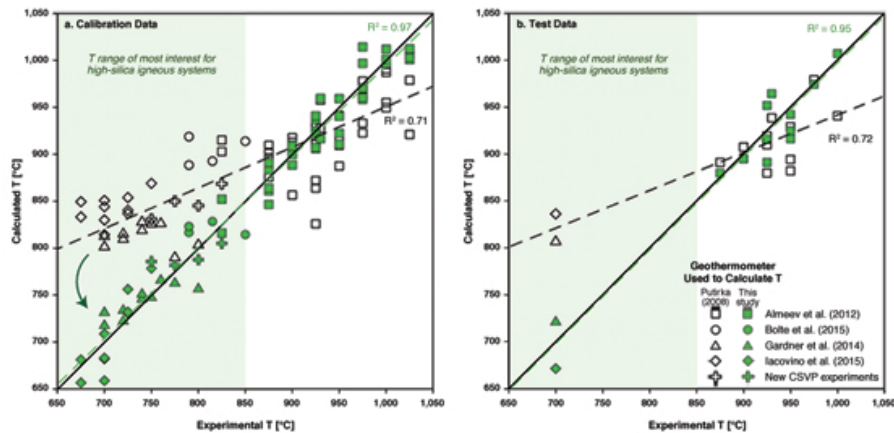
Figure 2.3: Calculated vs. experimental temperature. Temperatures are calculated using both the Putirka (2008, Eq. 33) clinopyroxene-liquid geothermometer (open symbols) and the new geothermometer (solid green symbols), and are plotted against the experimental conditions. Symbols are the same for both panels. The solid line represents unity between the calculated and experimental temperatures. Dashed lines show the best fit through each data set to better illustrate the new geothermometer's efficacy. (a) Calibration data. Arrow emphasizes that in the temperature range of most interest for high-silica magmatic systems, temperatures calculated with the new geothermometer are consistently closer to unity. (b) Test data.

3b). Based on results from the test data set, the new geothermometer has a SEE of ± 20 °C, and when applied to both the calibration and test data sets of high-Fe, low-Al experimental clinopyroxene, recovers these temperatures to within an average of 17 °C. In comparison, the Putirka (2008, Eq. 33) geothermometer, which is calibrated for a broad range of systems, has a reported SEE of ± 45 °C, and can overestimate the same experiments' temperatures by > 170 °C. For experiments performed $\leqslant 850$ °C, the new geothermometer returned temperatures within an average of 20 °C, a fivefold improvement over the Putirka (2008, Eq. 33) clinopyroxene-liquid geothermometer (Fig. 3).

The new geothermometer eliminates any dependence on Jd, and the H_2O and pressure terms in the Putirka (2008, Eq. 33) geothermometer were found to have no significant effect on this empirical calibration. The only clinopyroxene parameters on which the geothermometer relies are the Ca-Tschermak's (CaTs) and $DiHd_{2003}$ components. The new geothermometer has a strong dependence on the TiO_2 and MgO content of the liquid, and greatly increases the dependence on SiO_2 and CaO in the liquid over that of the Putirka (2008, Eq. 33) geothermometer. Because of the new geothermometer's strong dependence on the liquid composition, for input conditions we recommend only using

actual glass compositions measured as close as is prudent to the clinopyroxene of interest. This is in part because the rhyolitic whole rock oxide composition can deviate from that of the glass, particularly in those oxides used in the geothermometer, e.g., MgO, that tend to be higher in crystal cores. Using whole rock instead of glass compositions with the geothermometer increases the SEE of the calculated temperature. For example, a temperature calculated for Bishop Tuff samples using whole rock is $>$ 60 $^\circ$C higher ($>$ 3x the SEE) than a temperature calculated correctly with glass.

Calibration trials were also conducted using the same parameters as the Putirka (2008, Eq. 33) clinopyroxene-liquid geothermometer, including Jd and *P*. Although temperature estimates using these parameters were somewhat improved over the original Putirka (2008, Eq. 33) geothermometer (SEE $\pm$ 30 vs. $\pm$ 60 $^\circ$C for our test data set), this parameterization produced a lower R^2 than our new empirically based regression equation (0.81 vs. 0.95) and the SEE was $\sim$10 $^\circ$C greater (SEE $\pm$ 30 vs. $\pm$ 20 $^\circ$C) for both the entire test data set and the experiments performed $\leqslant$ 850 $^\circ$C. This result is not surprising, because although the Putirka (2008) geothermometer is thermodynamically motivated, it relies on Di, Hd, and Jd equilibria. The Jd content of natural high-silica system clinopyroxene can be zero, and the estimated Jd content of the new geothermometer's calibration data set is as low as 0.002.

Additionally, we explored a universal clinopyroxene-liquid geothermometer calibrated with a data set comprised of both our calibration data set and that used to calibrate Putirka (2008, Eq. 33). Although this geothermometer was able to return a temperature for all test data and improved SEE of experiments conducted $\leqslant$ 850 $^\circ$C vs. the original Putirka (2008, Eq. 33) geothermometer, it was not pursued as it did not improve the SEE for the high-Fe, low-Al test or calibration data sets. And, with R^2 = 0.80, the universal geothermometer had the poorest R^2 value of any of the candidate geothermometer equations. This is also not surprising, as the two calibration data sets—our high-Fe, low-Al clinopyroxene and Putirka (2008)'s generally more mafic clinopyroxene—have little overlap in Al_2O_3 vs. Mg# space or on the pyroxene quadrilateral (Fig. 2.1).

Although the Putirka (2008, Eq. 33) clinopyroxene-liquid geothermometer was calibrated to be broadly applied and is an excellent tool for use with the majority of igneous rock compositions, including more augitic or high-Al clinopyroxene from high-silica systems, high-Fe, low-Al clinopyroxene

appear to be an end-member case that requires special handling. For high-Fe, low-Al clinopyroxene, a universal geothermometer is unable to match the accuracy of a specialized tool.

In some cases, the temperatures calculated with the new geothermometer are within the uncertainty of the Putirka (2008, Eq. 33) geothermometer. However, the Putirka (2008) geothermometer will sometimes fail to return a temperature for high-Fe, low-Al clinopyroxene, particularly if Jd = 0 (i.e., when Al^{IV} = 0), and the new geothermometer eliminates this issue in addition to decreasing uncertainty. Although the new geothermometer calibration data set clinopyroxene has median 2.25 wt% Al_2O_3 (23% of the data set has < 1 wt%) it includes clinopyroxene with up to 7.08 wt% Al_2O_3 (Fig. 2.1). Thus, our new clinopyroxene-liquid geothermometer is recommended for use with natural systems that have bulk $SiO_2 \geqslant$ 70 wt% and bear clinopyroxene with Mg# $\leqslant$ 65 and $Al_2O_3 \leqslant$ 7 wt%. The most up to date version of an Excel spreadsheet and Python notebook for calculating temperature with this new geothermometer may be downloaded from GitHub at http://bit.ly/cpxrhyotherm.

2.3.3   Equilibrium of Natural Samples

An important question when considering using a clinopyroxene-liquid geothermometer is whether clinopyroxene are in equilibrium with coexisting liquid in natural samples. If the mineral did not crystallize in equilibrium with the liquid, results returned by a geothermometer that is based on these two compositions—such as ours—will be suspect. To investigate clinopyroxene-liquid equilibrium and provide a tool for assessing equilibrium in conjunction with our geothermometer, major element partition coefficients were calculated for all experimental compositions in the calibration data set (n = 64), as well as for the larger data set (n = 1290) used to calibrate the Putirka (2008) geothermometer. Using this combined experimental data set, we find SiO_2 clinopyroxene-liquid partition coefficients to be a reliable indicator of equilibrium, with mafic samples having $K_{d\,SiO_2}^{cpx-liquid}$ > 1.0 (average = 1.03), rhyolitic samples having $K_{d\,SiO_2}^{cpx-liquid}$ < 0.75 (average = 0.68), and intermediate silica samples having intermediate $K_{d\,SiO_2}^{cpx-liquid}$ values (average = 0.81). Thus, we advise using clinopyroxene-liquid pairs with our geothermometer only when the $K_{d\,SiO_2}^{cpx-liquid}$ is < 0.75.

The natural samples explored in the discussion section have average $K_{d\ SiO_2}^{cpx-liquid}$ = 0.66, indicating clinopyroxene is in equilibrium with rhyolitic liquids in these systems.

2.4 Application to Natural Systems

Here we use the new geothermometer to calculate temperatures for several natural high-silica systems (Table 2.4, A.4). In all cases the new geothermometer yields temperatures that are lower than those calculated with the Putirka (2008, Eq. 33) geothermometer; for the Bishop Tuff, Bandelier Tuff, and Paektu comendite, this difference is 130 °C on average (Fig. 2.4). For all high-silica systems considered, the new geothermometer calculates temperatures that are more consistent with our understanding of those systems, as well as with experimental phase equilibria and other mineral-derived temperatures.
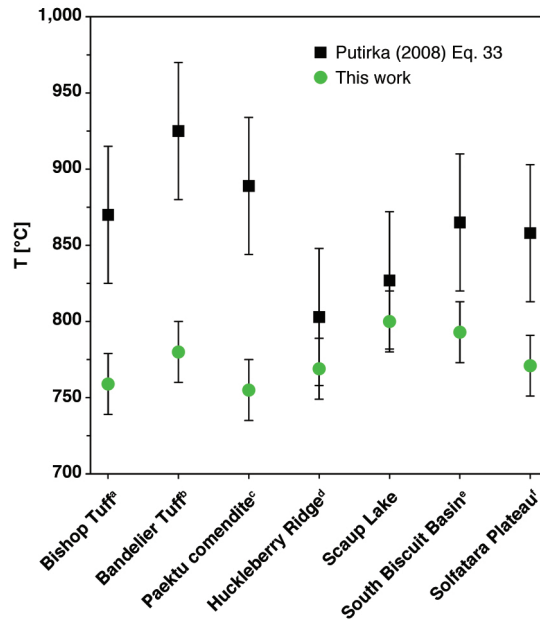
Figure 2.4: Natural clinopyroxene temperatures calculated with clinopyroxene-liquid geothermometers. Average ΔT is 87 °C. Compositional data from [a] Hildreth (1977) and Gardner et al. (2014), [b] Warshaw and Smith (1988) and Wilcock et al. (2013), [c] Iacovino et al. (2016), [d] Sisson (1991), [e] Girard and Stix (2010), and [f] Befus and Gardner (2016) and Girard and Stix (2010) available in Table A.4

2.4.1 Late-erupted Bishop Tuff, Long Valley

The 0.76 Ma late-erupted Bishop Tuff (Ig2) was emplaced at Long Valley Caldera in eastern California near the end of an eruption whose eruptive products covered as much as 2.5×10^6 km^2 of North America (Hildreth and Wilson 2007). The Bishop Tuff has been intensely studied (e.g., Hildreth 1977, 1981; Hervig and Dunbar 1992; Wilson and Hildreth 1997; Anderson et al. 2000; Bindeman and Valley 2002; Reid et al. 2011; Gualda and Ghiorso 2013; Chamberlain et al. 2014; Gualda and Sutton 2016) with particular interest in the possible stratification of the magma body before eruption, a hypothesis based on Fe-Ti oxide geothermometry. Fe-Ti oxide QUILF geothermometry (Anderson et al. 1993) returns a temperature over 800 $^\circ$C for the late-errupted ignimbrite and a temperature of $\sim$720 $^\circ$C for the earlier units (Hildreth and Wilson 2007; Ghiorso and Evans 2008). Similarly, quartz-magnetite oxygen isotope geothermometry returns 815 $^\circ$C for the late-erupted units and 715 $^\circ$C for the early erupted units (Bindeman and Valley 2002). However, Gardner et al. (2014) and Ghiorso and Gualda (2013) suggest that the Fe-Ti oxides did not crystallize in equilibrium with the rest of the Bishop Tuff phase assemblage and that the oxygen isotope geothermometry may not reflect magmatic storage temperatures. Instead, Gardner et al. (2014) suggest a pre-eruptive storage temperature of < 740 $^\circ$C based on phase equilibria experiments on the late-erupted Bishop Tuff composition.

Pyroxene phenocrysts are not present in the early-erupted Bishop Tuff, but clinopyroxene is present in the late-erupted Bishop Tuff (Table 2.4, A.4). Experimental studies of late-erupted Bishop Tuff pumice containing 20% phenocrysts of quartz, sanidine, plagioclase, clinopyroxene, orthopyroxene, biotite, magnetite, and ilmenite indicate that clinopyroxene does not crystallize at temperatures above 800 $^\circ$C at pressures > 1.4 kbar and is unlikely to crystallize above 820 $^\circ$C at pressures $\leqslant 1.2$ kbar (Pamukcu et al. 2012; Gardner et al. 2014). The Putirka (2008, Eq. 33) clinopyroxene-liquid geothermometer calculates 870 $^\circ$C for the late-erupted Bishop Tuff natural clinopyroxene rims, which places the clinopyroxene crystallization interval far above the experimental liquidus of Gardner et al. (2014) (Fig. 2.5). The new geothermometer calculates a late-erupted clinopyroxene temperature of 759 $^\circ$C that is well within the clinopyroxene's stability field in experimental studies and is also consistent with the Gardner et al. (2014) storage temperature and Ti-in-zircon geothermometry (Gualda and Ghiorso

Table 2.4: Average natural clinopyroxene compositions and clinopyroxene–liquid temperatures.

Locality	SiO$_2$	TiO$_2$	Al$_2$O$_3$	Cr$_2$O$_3$	FeO^{tot}	MnO	MgO	CaO	Na$_2$O	K$_2$O	T (°C)
Scaup Lake	51.56	0.17	0.64	0.01	15.42	0.75	11.13	19.97	0.32	0.03	800
	0.26	*0.02*	*0.04*	*0.01*	*0.51*	*0.05*	*0.23*	*0.24*	*0.02*	*0.01*	
South Biscuit Basin[a]	51.81	0.19	0.68	0	16.54	0.84	10.76	18.87	0.29	0.02	793
Solfatara Plateau[b]	49.34	0.22	0.48	0	26.37	0.87	4.12	18.29	0.3	0.01	771
Bishop Tuff[c]	51.98	0.15	0.74	0	12.82	0.57	12.69	20.65	0.38	0	759
Paektu Millennium[d]	48.94	0.22	0.2	0	28.75	0.88	0.86	18.46	1.7	0	755
Lava Creek Tuff A[e]	48.95	0.2	0.64	0	25.11	0.71	5.59	18.48	0.32	0	805
Lava Creek Tuff B[e]	48.57	0.23	0.62	0	26.68	0.73	4.48	18.38	0.31	0	776
Huckleberry Ridge Tuff[f]	48.49	0.2	0.6	0	27.4	0.86	3.28	18.89	0.3	0	769
Bandelier Tuff[g]	52.08	0.14	0.51	0	22.19	1.97	7.1	15.46	0.56	0	780

Oxides given in wt% and normalized. Standard deviation in italics for this work. SEE for temperature calculations is ± 20 °C. Complete data from [a] Girard and Stix (2010) [b] Girard and Stix (2010) and Befus and Gardner (2016) [c] Hildreth (1977) and Gardner et al. (2014) [d] Iacovino et al. (2016) [e] Hildreth, personal communication [f] Sisson (1991) [g] Warshaw and Smith (1988) are available in Table A.4.

2013) (Fig. 2.5). The lower clinopyroxene temperature of 759 °C is also closer to the Fe-Ti oxide and oxygen isotope temperatures for the early erupted units, lending support to the argument that this material may not have been stored at much higher temperatures than the early erupted products, and thus does not support a vertical stratification model for the Bishop Tuff magma body. Workers have suggested the pyroxene-free early erupted material may have been stored laterally to the late-erupted material (Wilson and Hildreth 1997; Cashman and Giordano 2014), and the new geothermometer results for the Bishop Tuff could lend credence to this hypothesis.
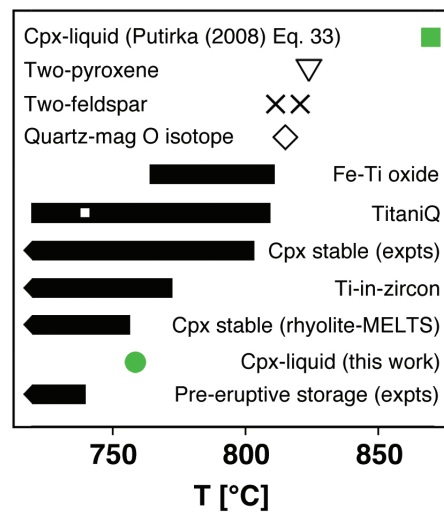
Figure 2.5: Comparison of temperatures and clinopyroxene stability for the late-erupted Bishop Tuff (Ig2). Clinopyroxene-liquid (Putirka 2008, Eq. 33), two-pyroxene (Frost and Lindsley 1992), two-feldspar (Chamberlain et al. 2014), and quartz-magnetite oxygen isotope (Bindeman and Valley 2002) temperatures all are higher than the experimental liquidus/clinopyroxene-in of Gardner et al. (2014). Fe-Ti oxide (Frost and Lindsley 1992) and TitaniQ (Wark et al. 2004, 2007) temperature ranges straddle this liquidus (white square = average TitaniQ temperature). The clinopyroxene-liquid temperature of this work is below the experimental liquidus, experimental liquidus and is more consistent with the rhyolite- MELTS clinopyroxene-in, the Gardner et al. (2014) Bishop Tuff pre-eruptive storage temperature, and the Ti in zircon in zircon temperature (Gualda and Ghiorso 2013) than the Putirka (2008, Eq. 33) clinopyroxene-liquid temperature.

2.4.2 Millennium Eruption Comendite, Paektu

Paektu (also known as Changbaishan) is a high-silica igneous system located on the border of the Democratic People's Republic of Korea and China. Circa 946 AD, the Paektu Millennium Eruption deposited 23 ± 5 km^3 DRE of tephra, most of which is comendite pumice containing alkali feldspar, clinopyroxene (Table 2.4, A.4), fayalite, Fe-Ti oxides, and quartz (Horn and Schmincke 2000). Phase equilibria experiments for this system indicate that clinopyroxene is the liquidus phase, with the liquidus at $\sim$720 °C at 1 kbar and $\sim$770 °C at 500 bar (Iacovino et al. 2015, 2016). Similar to the above results for the Bishop Tuff, the Putirka (2008, Eq. 33) clinopyroxene-liquid geothermometer returns a superliquidus temperature of 889 °C for the Millennium Eruption comendite pumice, whereas the new geothermometer yields a temperature of 755 °C, which approximates the temperature experimentally determined to best reproduce the natural phase assemblage (725 °C at 500 bar; Iacovino et al. 2015, 2016). Paektu is yet to be studied in depth, and it remains unclear whether the Millennium Eruption was the caldera-forming eruption. The new clinopyroxene-liquid geothermometer could help elucidate Paektu's history in future investigations.

2.4.3 Scaup Lake Rhyolite, Yellowstone

High-Fe, low-Al clinopyroxene is the most abundant mafic phase in the Scaup Lake rhyolite, a lava emplaced effusively ca. 257 ka, after the last caldera-forming eruption at Yellowstone (Christiansen et al. 2007; Girard and Stix 2009). Scaup Lake clinopyroxene (Table 2.4, A.4) exhibit exsolution lamellae, are reverse zoned with higher-Fe cores, and have alternating higher-and lower-Fe fine rim zones, all indicators of a complex pre-eruptive history involving both thermal and chemical variation (Till et al. 2015). The Putirka (2008, Eq. 33) clinopyroxene-liquid geothermometer was unable to calculate temperatures for several Scaup Lake clinopyroxene-liquid pairs because the Scaup Lake clinopyroxene have, on average, Jd $<$ 0.008. The new clinopyroxene-liquid geothermometer yields a temperature of 800 °C for the outermost rim of these clinopyroxene, which is slightly lower than that of the Putirka (2008, Eq. 33) geothermometer (827 °C when able to be calculated) and much lower

than the two-pyroxene temperature of ~880 °C obtained via PyMELTS (Sack and Ghiorso 1994) and QUILF. Other post-caldera lavas from Yellowstone, the South Biscuit Basin and Solfatara Plateau rhyolites emplaced ca. 255 and 103 ka, respectively (Christiansen 2001; Bindeman et al. 2008), yield new geothermometer temperatures ~80 °C lower than the temperatures calculated by the Putirka (2008, Eq. 33) clinopyroxene-liquid geothermometer (Fig. 4), underlining the importance of using the new geothermometer for the Yellowstone system.

We judge the new temperature to be the preferred temperature for Scaup Lake clinopyroxene rim growth because, unlike the Putirka (2008, Eq. 33) clinopyroxene-liquid geothermometer, the new geothermometer is able to calculate temperatures for all Scaup Lake clinopyroxene compositions and does not rely on the presence of co-crystallizing orthopyroxene, so it can be used if there is any uncertainty about phase equilibria. This temperature is slightly lower than that recorded by prior Fe-Ti oxide geothermometry (834–880 °C: Hildreth et al. 1984; Vazquez et al. 2009) and two-feldspar geothermometry (819 $\pm$ 20 °C: Till et al. 2015), differences we do not interpret as an error in geothermometry but rather as a reflection of the relative location of phase boundaries and a particular mineral-element pair's ability to diffusively re-equilibrate.

For example, Scaup Lake quartz return temperatures of 849 $\pm$ 13 °C for cores and 862 $\pm$ 10 °C for rims (Vazquez et al. 2009) via TitaniQ (Wark and Watson 2006). The new geothermometer's clinopyroxene rim temperature of 800 °C indicates that clinopyroxene continues to crystallize at or below the temperatures of the quartz-in phase boundary for the Scaup Lake rhyolite. Although there are questions as to the effect of growth rate and a_{TiO_2} on TitaniQ (e.g., Huang and Audétat 2012; Ghiorso and Gualda 2013; Pamukcu et al. 2016), this is the same relative positioning of the quartz-in and clinopyroxene-in phase boundaries observed in experiments on other similar composition systems such as the Blacktail Creek Tuff (Bolte et al. 2015) and Solfatara Plateau rhyolite (Befus and Gardner 2016).

The 800 °C rim crystallization temperature returned by the new geothermometer is also more consistent with our understanding of how exsolution lamellae form parallel to [100] in the cores of clinopyroxene, a feature that is observed in the Scaup Lake clinopyroxene. Experimental studies show that orthopyroxene-in-augite lamellae require temperatures below 825 °C to form (Huebner 1980;

Lindsley 1983). Temperatures calculated for Scaup Lake by other methods are too high to account for the formation of the lamellae, e.g., 862 ± 36 °C (Shaffer and Till 2016) via plagioclase-liquid geothermometry (Putirka 2008) and 876 ± 29 °C via QUILF two-pyroxene geothermometry.

2.4.4 Lava Creek Tuff and Huckleberry Ridge Tuff, Yellowstone

The Lava Creek Tuff is the product of the third, and most recent, caldera-forming eruption at Yellowstone that blanketed much of the continental United States in ash ca. 631 ka (Matthews et al. 2015). The Lava Creek Tuff is dominantly composed of two members, LCT-A and LCT-B, which are indistinguishable in age and separated by a layer of fallout ash (Christiansen 2001). High-Fe, low-Al clinopyroxene (Table 2.4, A.4) were described in both members by Hildreth et al. (1984). The new clinopyroxene-liquid geothermometer calculates temperatures for LCT-A and LCT-B of 805 and 776 °C, respectively. These temperatures correspond within error with geothermometry of other LCT-B phases, sanidine: 814 ± 23 °C via the Putirka (2008) alkali feldspar-liquid geothermometer and quartz: 815 ± 25 °C via TitaniQ (Shamloo and Till 2019), as well as an LCT-B magma storage temperature of 800 ± 50 °C determined using the rhyolite-MELTS geothermometer (Gualda and Ghiorso 2015; Befus et al. 2018). Hildreth (1981) conducted Fe-Ti oxide geothermometry of both members, calculating ∼800 °C for LCT-A and ∼950 °C for LCT-B, implying a thermal gradient in the magma body similar to that proposed for the Bishop Tuff. However, the new clinopyroxene-liquid temperatures are just within the uncertainty of each other and do not support the interpretation of a thermal gradient. The Putirka (2008, Eq. 33) clinopyroxene-liquid geothermometer does not return temperatures for any of these natural samples, reinforcing the utility of the new geothermometer.

The Putirka (2008, Eq. 33) clinopyroxene-liquid geothermometer does return temperatures for clinopyroxene-liquid pairs from the Huckleberry Ridge Tuff, which was erupted during Yellowstone's first caldera-forming eruption ca. 2.1 Ma (Christiansen 2001), and contains compositionally similar clinopyroxene to that of the Lava Creek Tuff. The new clinopyroxene-liquid geothermometer returns a temperature for Huckleberry Ridge of 769 °C, which is more than 30 °C lower than the Putirka (2008, Eq. 33) geothermometer and below the rhyolite-MELTS-calculated liquidus for this system

when modeled at 4.7 wt% H_2O (Gualda et al. 2012; Myers et al. 2016). A clinopyroxene-liquid temperature of 769 $^{\circ}$C is also consistent with two-feldspar geothermometry for the ignimbrite of 768–855 $^{\circ}$C (Elkins and Grove 1990; Swallow et al. 2018). The new clinopyroxene-liquid temperatures for these large siliceous tuffs $\leqslant$ 805 $^{\circ}$C implies that these minerals were last crystallizing at near-solidus conditions and at relatively high crystal/liquid ratios.

2.5 Implications

In general, the new clinopyroxene-liquid geothermometer lowers calculated temperatures for a given sample by an average of almost 90 $^{\circ}$C relative to prior clinopyroxene-liquid geothermometers (Fig. 2.4). In all cases where experiments are available, the temperature returned by the new geothermometer is between the solidus and liquidus for the relevant bulk composition, indicating that the new clinopyroxene-liquid geothermometer is a better approximation of the relevant geologic conditions than the Putirka (2008, Eq. 33) geothermometer, which consistently returns temperatures above the experimental liquidi or the clinopyroxene-in phase boundaries of silicic magmas. Thus, the new geothermometer reconciles many inconsistencies in previous thermometric results.

It is important to note that clinopyroxene chemistry and stability in high-silica systems is not the same as in mafic systems. Dry experiments on mafic bulk compositions reveal that clinopyroxene is stable from $\sim$1180–1470 $^{\circ}$C at 1 atm to 25 kbar and is usually stable in these experiments to at least 25 $^{\circ}$C below its first appearance (e.g., Elthon and Scarfe 1984; Grove and Juster 1989; Juster et al. 1989; Bartels et al. 1991; Grove et al. 1992; Kinzler and Grove 1992; Feig et al. 2010, 2006), however experiments on silicic bulk compositions that constrain clinopyroxene stability are exclusively hydrous and restrict clinopyroxene stability to below 1000 $^{\circ}$C (e.g., Almeev et al. 2012; Gardner et al. 2014; Bolte et al. 2015; Iacovino et al. 2015). In dry mafic systems above 11 kbar, clinopyroxene is rarely a liquidus phase and may become unstable 25–40 $^{\circ}$C after its first appearance (e.g., Elthon and Scarfe 1984; Grove and Juster 1989; Juster et al. 1989; Bartels et al. 1991; Grove et al. 1992; Kinzler and Grove 1992; Feig et al. 2010, 2006). Conversely, in high-silica systems, experiments often place clinopyroxene on the liquidus (Almeev et al. 2012; Gardner et al. 2014; Bolte et al. 2015; Iacovino

et al. 2015). And although clinopyroxene is a mafic phase, experiments and our temperature calculations demonstrate that its stability is not restricted to near-liquidus temperatures. We have calculated clinopyroxene in high-silica natural systems to below 775 °C for the late-erupted Bishop Tuff, Paektu comendite, and Bandelier Tuff (Fig. 4, Table 2.4), and experiments have shown the mineral to crystallize at, or near, the solidus to temperatures as low as 675 °C (e.g., Almeev et al. 2012; Gardner et al. 2014; Bolte et al. 2015; Iacovino et al. 2015; Befus and Gardner 2016). If clinopyroxene stability extends from the liquidus to the solidus in high-silica magma, the presence of clinopyroxene does not necessitate the invocation of xenocrysts, mixing with a hotter magma body, nor imply a low (or high) crystallinity. Instead, clinopyroxene, when present, appears to be a persistent phase throughout the crystallization interval of high-silica systems.

Because of the lack of relevant experiments in its calibration data set, thermodynamic phase equilibria modeling of clinopyroxene-bearing systems using rhyolite-MELTS remains problematic. Although rhyolite-MELTS produces a realistic clinopyroxene crystallization interval—that is, one consistent with the new geothermometer's temperature—for the Bishop Tuff (Fig. 2.5), it should be noted that rhyolite-MELTS was calibrated for this particular locality and the model does not perform as well for other high-silica systems. Rhyolite-MELTS modeling often places clinopyroxene in the middle of, or late in, the high-silica system crystallization sequence, rather than on the liquidus as suggested by experiments (e.g., Almeev et al. 2012; Gardner et al. 2014; Iacovino et al. 2015). Rhyolite-MELTS failed to predict crystallization of clinopyroxene for 70% of the systems examined for this work, all of which contain clinopyroxene in the equilibrium mineral assemblage. For the trials in which clinopyroxene was predicted (not including the Bishop Tuff), on average rhyolite-MELTS predicted the clinopyroxene-in phase boundary over 120 °C below the temperatures returned by the new clinopyroxene-liquid geothermometer and experimental phase equilibria, where available. We join other workers in urging caution when using rhyolite-MELTS to simulate systems in which clinopyroxene is present (e.g., Gardner et al. 2014), as its failure to accurately simulate the mineral's behavior may give the mistaken impression that clinopyroxene has a much narrower crystallization interval than in reality, as well as suggest an inaccurate degree of crystallinity.

Finding low-Al clinopyroxene in a lava may be evaluative in and of itself. In high-silica systems, clinopyroxene contains < 2 wt% Al_2O_3 (Fig. 2.1), while it is possible for mafic clinopyroxene to contain > 10 wt% Al_2O_3, when compositions are queried from the GEOROC database. The low Al content in rhyolitic clinopyroxene is a result of a need for more Si in tetrahedral sites to compensate for the charge imbalance with O_3 oxygen atoms produced by low Ca content in the crystal (CaO can be < 17 wt% in rhyolitic clinopyroxene and up to > 23 wt% in basaltic clinopyroxene; data from GEOROC) (Salviulo et al. 2000). Thus, the presence of low-Al clinopyroxene outside of a rhyolite may indicate that the mineral has been inherited from a higher-silica magma or country rock.

Low-Al, high-Fe clinopyroxene may also hint at the thermal history of the lava. Clinopyroxene high in Al have been linked to fast crystal growth and thus high undercooling; during this process the crystal grows faster than the melt can deliver nutrients to the growth surface, causing a depletion of compatible elements in the surrounding melt as well as an enrichment in incompatible elements. As the crystal grows, it incorporates more incompatible elements into its structure, causing an increase in these elements rim-ward (Lofgren et al. 2006; Zhang 2008; Mollo and Hammer 2017). Conversely, crystal rims low in incompatible and high in compatible elements as described herein counterindicate interface-controlled growth and instead imply diffusion-controlled growth wherein the diffusive velocity of elements in the melt is sufficient to deliver the ideal nutrients to the crystal. Additionally, experimental studies on basaltic compositions have correlated low Al with slow cooling rates (e.g., Mollo et al. 2010). The above suggests a slow growth rate for the low-Al, high-Fe clinopyroxene found in high-silica magmatic systems, relative to high-Al clinopyroxene (Zhang 2008). This, combined with our new geothermometer and clinopyroxene's broad stability in high-silica magmatic systems, makes the mineral an attractive tool for investigating a range of processes in these hazardous geological settings.

References

Almeev, R.R., Bolte, T., Nash, B.P., Holtz, F., Erdmann, M., and Cathey, H.E. (2012) High-temperature, low-H_2O Silicic Magmas of the Yellowstone Hotspot: an Experimental Study of Rhyolite from the Bruneau-Jarbidge Eruptive Center, Central Snake River Plain, USA. *Journal of Petrology*, 53, 1837–1866.

Anderson, A.T., Davis, A.M., and Lu, F. (2000) Evolution of Bishop Tuff Rhyolitic Magma Based on Melt and Magnetite Inclusions and Zoned Phenocrysts. *Journal of Petrology*, 41, 449–473.

Anderson, D.J., Lindsley, D.H., and Davidson, P.M. (1993) QUILF: A pascal program to assess equilibria among Fe, Mg, Mn, Ti oxides, pyroxenes, olivine, and quartz. *Computers & Geosciences*, 19, 1333–1350.

Bartels, K.S., Kinzler, R.J., and Grove, T.L. (1991) High pressure phase relations of primitive high-alumina basalts from Medicine Lake volcano, northern California. *Contributions to Mineralogy and Petrology*, 108, 253–270.

Befus, K.S., and Gardner, J.E. (2016) Magma storage and evolution of the most recent effusive and explosive eruptions from Yellowstone Caldera. *Contributions to Mineralogy and Petrology*, 171.

Befus, K.S., Bruyere, R.H., and Manga, M. (2018) Lava Creek Tuff Love. Presented at the Goldschmidt, Boston, MA, USA. Bindeman, I.N., and Valley, J.W. (2002) Oxygen isotope study of the Long Valley magma system, California: isotope thermometry and convection in large silicic magma bodies. *Contributions to Mineralogy and Petrology*, 144, 185–205.

Bindeman, I.N., Fu, B., Kita, N.T., and Valley, J.W. (2008) Origin and Evolution of Silicic Magmatism at Yellowstone Based on Ion Microprobe Analysis of Isotopically Zoned Zircons. *Journal of Petrology*, 49, 163–193.

Bolte, T., Holtz, F., Almeev, R., and Nash, B. (2015) The Blacktail Creek Tuff: an analytical and experimental study of rhyolites from the Heise volcanic field, Yellowstone hotspot system. *Contributions to Mineralogy and Petrology*, 169.

Cashman, K.V., and Giordano, G. (2014) Calderas and magma reservoirs. *Journal of Volcanology and Geothermal Research*, 288, 28–45.

Chamberlain, K.J., Morgan, D.J., and Wilson, C.J.N. (2014) Timescales of mixing and mobilisation in the Bishop Tuff magma body: perspectives from diffusion chronometry. *Contributions to Mineralogy and Petrology*, 168.

Christiansen, R.L. (2001) *The Quaternary and Pliocene Yellowstone Plateau volcanic field of Wyoming, Idaho, and Montana*, 145 p. U.S. Geological Survey, Reston, VA.

Christiansen, R.L., Lowenstern, J.B., Smith, R.B., Heasler, H., Morgan, L.A., Nathenson, M., Mastin, L.G., Muffler, L.J.P., and Robinson, J.E. (2007) Preliminary Assessment of Volcanic and Hydrothermal Hazards in Yellowstone National Park and Vicinity p. 94. USGS.

Elkins, L.T., and Grove, T.L. (1990) Ternary feldspar experiments and thermodynamic models. *American Mineralogist*, 75, 544–559.

Elthon, D., and Scarfe, C.M. (1984) High-pressure phase equilibria of a high-magnesian basalt and the genesis of primary oceanic basalts. *American Mineralogist*, 69, 1–15.

Feig, S.T., Koepke, J., and Snow, J.E. (2006) Effect of water on tholeiitic basalt phase equilibria: an experimental study under oxidizing conditions. *Contributions to Mineralogy and Petrology*, 152, 611–638.

———(2010) Effect of oxygen fugacity and water on phase equilibria of a hydrous tholeiitic basalt. *Contributions to Mineralogy and Petrology*, 160, 551–568.

Frost, B.R., and Lindsley, D.H. (1992) Equilibria among Fe-Ti oxides, pyroxenes, olivine, and quartz: Part II. Application. *American Mineralogist*, 77, 1004–1020.

Gansecki, C. A. (1998) $^{40}Ar/^{39}Ar$ geochronology and pre-eruptive geochemistry of the Yellowstone Plateau volcanic field rhyolites. Stanford University.

Gardner, J.E., Befus, K.S., Gualda, G.A.R., and Ghiorso, M.S. (2014) Experimental constraints on rhyolite-MELTS and the Late Bishop Tuff magma body. *Contributions to Mineralogy and Petrology*, 168.

Ghiorso, M.S., and Evans, B.W. (2008) Thermodynamics of Rhombohedral Oxide Solid Solutions and a Revision of the FE-TI Two-Oxide Geothermometer and Oxygen-Barometer. *American Journal of Science*, 308, 957–1039.

Ghiorso, M.S., and Gualda, G.A.R. (2013) A method for estimating the activity of titania in magmatic liquids from the compositions of coexisting rhombohedral and cubic iron–titanium oxides. *Contributions to Mineralogy and Petrology*, 165, 73–81.

Girard, G., and Stix, J. (2009) Magma Recharge and Crystal Mush Rejuvenation Associated with Early Post-collapse Upper Basin Member Rhyolites, Yellowstone Caldera, Wyoming. *Journal of Petrology*, 50, 2095–2125.

Girard, G., and Stix, J. (2010) Rapid extraction of discrete magma batches from a large differenti-ating magma chamber: the Central Plateau Member rhyolites, Yellowstone Caldera, Wyoming. *Contributions to Mineralogy and Petrology*, 160, 441–465.

Grove, T.L., and Juster, T.C. (1989) Experimental investigations of low-Ca pyroxene stability and olivine-pyroxene-liquid equilibria at 1-atm in natural basaltic and andesitic liquids. *Contributions to Mineralogy and Petrology*, 103, 287–305.

Grove, T.L., Kinzler, R.J., and Bryan, W.B. (1992) Fractionation of Mid-Ocean Ridge Basalt (MORB). *Geophysical Monograph*, 71, 281–310.

Gualda, G.A.R., and Ghiorso, M.S. (2013) The Bishop Tuff giant magma body: an alternative to the Standard Model. *Contributions to Mineralogy and Petrology*, 166, 755–775.

———(2015) MELTS_Excel: A Microsoft Excel-based MELTS interface for research and teaching of magma properties and evolution. *Geochemistry, Geophysics, Geosystems*, 16, 315–324.

Gualda, G.A.R., and Sutton, S.R. (2016) The Year Leading to a Supereruption. (A.K. Schmitt, Ed.)PLOS ONE, 11, e0159200. Gualda, G.A.R., Ghiorso, M.S., Lemons, R.V., and Carley, T.L. (2012) Rhyolite-MELTS: a Modified Calibration of MELTS Optimized for Silica-rich, Fluid-bearing Magmatic Systems. *Journal of Petrology*, 53, 875–890.

Hervig, R.L., and Dunbar, N.W. (1992) Cause of chemical zoning in the Bishop (California) and Ban-delier (New Mexico) magma chambers. *Earth and Planetary Science Letters*, 111, 97–108.

Hildreth, E.W. (1977) The magma chamber of the Bishop Tuff: Gradients in temperature, pressure, and composition. Ph.D. thesis, University of California, Berkeley.

Hildreth, W. (1981) Gradients in silicic magma chambers: Implications for lithospheric magmatism. *Journal of Geophysical Research: Solid Earth*, 86, 10153–10192.

Hildreth, W., and Wilson, C.J.N. (2007) Compositional Zoning of the Bishop Tuff. *Journal of Petrol-ogy*, 48, 951–999.

Hildreth, W., Christiansen, R.L., and O'Neil, J.R. (1984) Catastrophic isotopic modification of rhy-olitic magma at times of caldera subsidence, Yellowstone Plateau Volcanic Field. *Journal of Geo-physical Research: Solid Earth*, 89, 8339–8369.

Horn, S., and Schmincke, H.-U. (2000) Volatile emission during the eruption of Baitoushan Volcano (China/North Korea) ca. 969 AD. *Bulletin of Volcanology*, 61, 0537–0555.

Huang, R., and Audétat, A. (2012) The titanium-in-quartz (TitaniQ) thermobarometer: A critical ex-amination and re-calibration. *Geochimica et Cosmochimica Acta*, 84, 75–89.

Huebner, J.S. (1980) Pyroxene phase equilibria at low pressure. In C.T. Preweitt, Ed., *Pyroxenes*, Reviews in Mineralogy Vol. 7. Mineralogical Society of America.

Iacovino, K., Kim, J.S., Sisson, T.W., Lowenstern, J.B., Jang, J.N., Song, K.H., Ham, H.H., Ri, K.H., Donovan, A.R., Oppenheimer, C., and others (2015) New Constraints on the Geochemistry of the Millennium Eruption of Mount Paektu (Changbaishan), Democratic People's Republic of Korea/China. In 2015 AGU Fall Meeting. San Francisco, CA, USA.

Iacovino, K., Kim, J.-S., Sisson, T., Lowenstern, J., Ri, K.-H., Jang, J.-N., Song, K.-H., Ham, S.-H., Oppenheimer, C., Hammond, J.O.S., and others (2016) Quantifying gas emissions from the "Millennium Eruption" of Paektu volcano Democratic People's Republic of Korea/China. *Science Advances*, 2, 1–11.

Juster, T.C., Grove, T.L., and Perfit, M.R. (1989) Experimental constraints on the generation of FeTi basalts, andesites, and rhyodacites at the Galapagos Spreading Center, 85°W and 95°W. *Journal of Geophysical Research*, 94, 9251.

Kinzler, R.J., and Grove, T.L. (1992) Primary magmas of mid-ocean ridge basalts 1. Experiments and methods. *Journal of Geophysical Research*, 97, 6885.

Liang, Y., Sun, C., and Yao, L. (2013) A REE-in-two-pyroxene thermometer for mafic and ultramafic rocks. *Geochimica et Cosmochimica Acta*, 102, 246–260.

Lindsley, D.H. (1983) Pyroxene thermometry. *American Mineralogist*, 68, 477–493.

Lindsley, D.H., and Andersen, D.J. (1983) A two-pyroxene thermometer. *Journal of Geophysical Research*, 88, A887.

Lofgren, G.E., Huss, G.R., and Wasserburg, G.J. (2006) An experimental study of trace-element partitioning between Ti-Al-clinopyroxene and melt: Equilibrium and kinetic effects including sector zoning. *American Mineralogist*, 91, 1596–1606.

Masotta, M., Mollo, S., Freda, C., Gaeta, M., and Moore, G. (2013) Clinopyroxene–liquid thermometers and barometers specific to alkaline differentiated magmas. *Contributions to Mineralogy and Petrology*, 166, 1545–1561.

Matthews, N.E., Vazquez, J.A., and Calvert, A.T. (2015) Age of the Lava Creek supereruption and magma chamber assembly from combined 40 Ar/ 39 Ar and U-Pb dating of sanidine and zircon crystals. *Geochemistry, Geophysics, Geosystems*, 16, 2508–2528.

Mollo, S., and Hammer, J.E. (2017) Dynamic crystallization in magmas. In W. Heinrich and R. Abart, Eds., *Mineral reaction kinetics: Microstructures, textures, chemical and isotopic signatures* Vol. 16, pp. 378–418. Mineralogical Society of Great Britain & Ireland.

Mollo, S., Del Gaudio, P., Ventura, G., Iezzi, G., and Scarlato, P. (2010) Dependence of clinopyroxene composition on cooling rate in basaltic magmas: Implications for thermobarometry. *Lithos*, 118, 302–312.

Myers, M.L., Wallace, P.J., Wilson, C.J.N., Morter, B.K., and Swallow, E.J. (2016) Prolonged ascent and episodic venting of discrete magma batches at the onset of the Huckleberry Ridge supereruption, Yellowstone. *Earth and Planetary Science Letters*, 451, 285–297.

Pamukcu, A.S., Gualda, G.A.R., and Anderson, A.T. (2012) Crystallization Stages of the Bishop Tuff Magma Body Recorded in Crystal Textures in Pumice Clasts. *Journal of Petrology*, 53, 589–609.

Pamukcu, A.S., Ghiorso, M.S., and Gualda, G.A.R. (2016) High-Ti, bright-CL rims in volcanic quartz: a result of very rapid growth. *Contributions to Mineralogy and Petrology*, 171.

Putirka, K.D. (2008) Thermometers and Barometers for Volcanic Systems. *Minerals, Inclusions and Volcanic Processes*, Reviews in Mineralogy and Geochemistry, 69, 61–120.

Putirka, K.D., Mikaelian, H., Ryerson, F., and Shaw, H. (2003) New clinopyroxene-liquid thermo-barometers for mafic, evolved, and volatile-bearing lava compositions, with applications to lavas from Tibet and the Snake River Plain, Idaho. *American Mineralogist*, 88, 1542–1554.

Reid, M.R., Vazquez, J.A., and Schmitt, A.K. (2011) Zircon-scale insights into the history of a Supervolcano, Bishop Tuff, Long Valley, California, with implications for the Ti-in-zircon geothermometer. *Contributions to Mineralogy and Petrology*, 161, 293–311.

Sack, R.O., and Ghiorso, M.S. (1994) Thermodynamics of multicomponent pyroxenes: II. Phase relations in the quadrilateral. *Contributions to Mineralogy and Petrology*, 116, 287–300.

Salviulo, G., Secco, L., Marzoli, A., Piccirillo, E.M., and Nyobe, J.B. (2000) Ca-rich pyroxene from basic and silicic volcanic rocks from the Cameroon Volcanic Line (West-Africa): crystal chemistry and petrological relationships. *Mineralogy and Petrology*, 70, 73–88.

Shaffer, J.S., and Till, C.B. (2016) New Temperature and H_2O Estimates for Post Caldera Yellowstone Rhyolite Lavas using Feldspar Geothermometry and Rhyolite-MELTS. In 2016 AGU Fall Meeting. San Francisco, CA, USA.

Shamloo, H.I., and Till, C.B. (2019) Decadal transition from quiescence to supereruption: petrologic investigation of the Lava Creek Tuff, Yellowstone Caldera, WY. *Contributions to Mineralogy and Petrology*, 174.

Sisson, T.W. (1991) Pyroxene-high silica rhyolite trace element partition coefficients measured by ion microprobe. *Geochimica et Cosmochimica Acta*, 55, 1575–1585.

Swallow, E.J., Wilson, C.J.N., Myers, M.L., Wallace, P.J., Collins, K.S., and Smith, E.G.C. (2018) Evacuation of multiple magma bodies and the onset of caldera collapse in a supereruption, captured in glass and mineral compositions. *Contributions to Mineralogy and Petrology*, 173.

Till, C.B., Vazquez, J.A., and Boyce, J.W. (2015) Months between rejuvenation and volcanic eruption at Yellowstone caldera, Wyoming. *Geology*, 43, 695–698.

Vazquez, J.A., Kyriazis, S.F., Reid, M.R., Sehler, R.C., and Ramos, F.C. (2009) Thermochemical evolution of young rhyolites at Yellowstone: Evidence for a cooling but periodically replenished post-caldera magma reservoir. *Journal of Volcanology and Geothermal Research*, 188, 186–196.

Wark, D.A., and Watson, E.B. (2006) TitaniQ: a titanium-in-quartz geothermometer. *Contributions to Mineralogy and Petrology*, 152, 743–754.

Wark, D.A., Hildreth, W., Watson, E.B., and Cherniak, D.J. (2004) Origin of Thermal and Compositional Zoning in the Bishop Magma Reservoir: Insights from Zoned Quartz Phenocrysts p. 3. Presented at the 2004 AGU Fall Meeting, San Francisco, CA, USA.

Wark, D.A., Hildreth, W., Spear, F.S., Cherniak, D.J., and Watson, E.B. (2007) Pre-eruption recharge of the Bishop magma system. *Geology*, 35, 235.

Warshaw, C.M., and Smith, R.L. (1988) Pyroxenes and fayalites in the Bandelier Tuff, New Mexico: temperatures and comparison with other rhyolites. *American Mineralogist*, 73, 1025–1037.

Wilcock, J., Goff, F., Minarik, W.G., and Stix, J. (2013) Magmatic Recharge during the Formation and Resurgence of the Valles Caldera, New Mexico, USA: Evidence from Quartz Compositional Zoning and Geothermometry. *Journal of Petrology*, 54, 635–664.

Wilson, C.J.N., and Hildreth, W. (1997) The Bishop Tuff: New Insights From Eruptive Stratigraphy. *The Journal of Geology*, 105, 407–440.

Zhang, Y. (2008) *Geochemical Kinetics*, 631 p. Princeton University Press, Princeton, New Jersey.

Chapter 3

DIFFUSION CHRONOMETRY USING A PROXY TO THE GROWTH-THEN-DIFFUSION INITIAL
CONDITION: THE SCAUP LAKE RHYOLITE, YELLOWSTONE

Abstract

In order to interpret modern-day unrest at Yellowstone Caldera, timescales leading up to its most
common type of eruption, that of effusively emplaced rhyolite, must be quantified. Eruption of the
Scaup Lake rhyolite ended $\sim$220,000 years of dormancy at this high-silica system. This work takes
advantage of the different rates of elemental diffusion in clinopyroxene to calculate the magmatic
timescales of events preceding emplacement of the Scaup Lake rhyolite. Here, diffusion chronometry
accounting for various sources of error and using multiple elements from NanoSIMS measurements of
Scaup Lake clinopyroxene rims is presented to better understand the relationship between timescales
captured by different minerals from the same volcanic event. Although the rims of different minerals
have previously been considered to record the same events, and sometimes a single mineral has been
used to represent the pre-eruptive history of a given lava flow, we show that the events and timescales
archived by mineral rims from the same lava may not be concomitant. The Scaup Lake rhyolite ap-
pears to have undergone several rejuvenation events over the > 2400 years before its eruption was
triggered, however the last rejuvenation event which occurred < 40 years before eruption was not
recorded by the clinopyroxene.

Multiple methods must be used when determining a timescale for a given process; the degeneracy
inherent in diffusion chronometry modeling means that usually a single true timescale is not identifi-
able via this method. The interpretation of diffusive timescales from mineral rims requires a holistic
petrological approach that includes phase equilibria and crystal growth and dissolution rates.

3.1   Introduction

A persistent challenge in the study of volcanoes and their magmatic systems is determining timescales of magmatic processes, the goal of which is, in part, to construct a timeline of pre-eruptive events that may be used to forecast volcanic eruptions. Geochemical studies have investigated the rate and duration of various magmatic processes, including residence time of a crystal in a magma (e.g., Bindeman and Valley 2001; Costa et al. 2003; Morgan et al. 2004; Cooper and Kent 2014; Stelten et al. 2015; Wotzlaw et al. 2015; Budd et al. 2017; Lynn et al. 2017; Rubin et al. 2017; Morgado et al. 2019), magma chamber assembly (e.g., Druitt et al. 2012; Saunders et al. 2012; Rubin et al. 2016; Reid and Vazquez 2017), magma generation and reheating rates (e.g., Bachmann and Bergantz 2006; Simakin and Bindeman 2012), timescales of intrusion and ascent rates (e.g., Bindeman et al. 2008; Myers et al. 2016; Gordeychik et al. 2018; Mutch et al. 2019), rejuvenation (e.g., Costa and Chakraborty 2004; Morgan et al. 2006; Martin et al. 2008; Allan et al. 2013; Chamberlain et al. 2014; Till et al. 2015; Degruyter et al. 2016; Hartley et al. 2016; Singer et al. 2016, 2016; Pistone et al. 2017), assimilation (e.g., Costa and Dungan 2005), and pre-eruptive "priming" (e.g., Stock et al. 2016).

In recent years, the application of diffusion chronometry to these investigations has flourished. This method calculates timescales from minerals that have intracrystalline chemical zoning resulting from a change in magma chemistry. Diffusion chronometry employs the diffusion rate of elements that migrate through the mineral in order to attain chemical equilibrium (Costa and Morgan 2011). Timescales yielded from this method represent the time that has elapsed between when a chemically distinct mineral zone grew and when the mineral cooled enough to halt chemical diffusion—in igneous petrology, usually this occurs when the mineral cools after volcanic emplacement. This method has been used to study many magmatic systems from mafic to silicic and timescales can be as short as days to weeks (e.g., Pamukcu et al. 2016; Morgado et al. 2019; Mutch et al. 2019; Sundermeyer et al. 2020).

Most studies of intracrystalline diffusion in magmatic systems employ a single element in one mineral; only a fraction utilize diffusion timescales from different elements within a given mineral

(e.g., Costa and Dungan 2005; Morgan and Blake 2006; Druitt et al. 2012; Albert et al. 2015; Till et al. 2015; Bouvet de Maisonneuve et al. 2016; Lynn et al. 2017; Andersen et al. 2018; Gordeychik et al. 2018; Mutch et al. 2019). Fewer still have modeled diffusion in multiple minerals from the same eruption (e.g., Chamberlain et al. 2014; Singer et al. 2016; Cooper et al. 2017; Flaherty et al. 2018; Shamloo and Till 2019). Generally, diffusion timescales calculated from a single element-mineral pair are extrapolated to the entire magmatic system, the assumption being that zonation present in one mineral represents the same events as similarly sequenced zones in another mineral from the same lava. For example, the most rim-ward zones in two types of minerals from the same lava might be expected to represent the same event, a hypothesis that requires validation from the system's phase equilibria relationships.
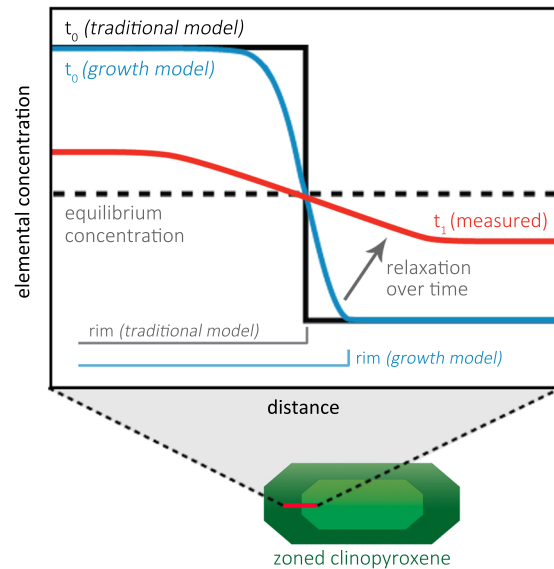
Figure 3.1: Diffusive relaxation of trace element intracrystalline zoning in clinopyroxene.

In this work, we utilize clinopyroxene from Yellowstone Caldera's Scaup Lake rhyolite and compare its diffusive timescales to those of another mineral from the same lava flow that is believed to have an overlapping crystallization interval, sanidine (Brugman and Till 2019). In this study we are interested in whether Scaup Lake clinopyroxene and sanidine record the same magmatic events with

the larger aim of addressing the similarities and differences of the pre-eruptive record of different minerals within the same erupted magma body.

We also examine the difference between chemical zonation that results only from diffusion, and chemical zonation that results from both mineral growth while magma body chemistry is changing *and subsequent* diffusion (hereafter referred to as "growth-then-diffusion"). It is important to model each case appropriately, depending on whether crystal growth or diffusion is thought to occur at a faster rate in the particular mineral of interest over the relevant temperature range, or if they occur at similar competing rates (Zhang 2008).

In cases where diffusion is the dominant (i.e., faster) process, the final analyzed chemical profile is assumed to have relaxed from an initial profile that resembles a step function (Fig. 3.1, solid black line), indicating that the new crystal rim grew instantaneously relative to any changes in melt composition. This is a common assumption made in igneous diffusion chronometry studies and is reasonable for many element-mineral pairs where diffusion is relatively slow relative to the timescales of dynamic changes in melt composition and crystal growth rates, such as olivine growth followed by diffusion in a melt-dominated mafic magmatic system (e.g., Shea et al. 2015).

However, if crystal growth occurs over comparable, or shorter, timescales than magma mixing and melt composition evolution, the initial chemical profile prior to diffusive relaxation cannot be assumed to be a step function. These scenarios require an independent assessment of the initial chemical profile shape and can be modeled utilizing two elements with vastly different diffusivities: a slower-diffusing element may be used to assess the initial profile shape, and a faster-diffusing element may be employed to assess the elapsed time since crystal rim growth (e.g., Costa et al. 2003, 2008; Milman-Barris et al. 2008; Till et al. 2015; Mutch et al. 2019). As suggested by recent studies (e.g., Till et al. 2015; Mutch et al. 2019; Shamloo and Till 2019), this approach is likely necessary for crystal-rich and/or high-silica magmatic systems where magma mixing is likely to be sluggish and in greater competition with crystal growth and diffusion rates. Here we develop a method using multiple elements from the same mineral to calculate diffusion timescales when the effects of both crystal growth and diffusion must be taken into account. Recent studies have made strides to improve error reporting for diffusion chronometry (e.g., Gualda et al. 2012; Allan et al. 2013; Gualda and Sutton

2016; Cooper et al. 2017; Mutch et al. 2019) and here we also aim to further these efforts. We discuss and robustly report error and urge the diffusion chronometry community to reevaluate the common practice of reporting a single diffusion timescale value as a precise chronometer.

3.2 Geologic Setting and Samples

Large high-silica igneous systems like Yellowstone Caldera are of particular interest due to their potential to threaten life and affect commerce. Yellowstone Caldera in NW Wyoming (Fig. 3.2 A) is the youngest expression of the Yellowstone-Snake River Plain hotspot track which trends NE across the northwestern United States from its first apparent eruptive center in SE Oregon (ca. 16 Ma). The current caldera is the result of three major explosive eruptions which formed the Huckleberry Ridge Tuff at 2.09 Ma, the Mesa Falls Tuff at 1.303 Ma, and the Lava Creek Tuff at 0.63 Ma (Rivera et al. 2014, 2016; Matthews et al. 2015). Although these are among the largest explosive eruptions on Earth, Yellowstone more commonly generates effusive rhyolitic eruptions; Yellowstone has produced > 20 of these large-volume flows since the last caldera-forming eruption (Fig. 3.2 B), and future activity is likely to be effusive as well (e.g., Christiansen et al. 2007; Girard and Stix 2012; Watts et al. 2012; Stelten et al. 2015; Till et al. 2019).

The most recent post-caldera effusive eruptions can be divided into three groups: the early Upper Basin Member (UBM) rhyolites that erupted > 480 ka, the late UBM rhyolites that erupted ∼260 ka, and the Central Plateau Member (CPM) rhyolites that erupted ∼170−70 ka (Fig. 3.2 B) (Till et al. 2019 and references therein). Exposed just south of the Mallard Lake resurgent dome, the ca. 262 ka (Christiansen et al. 2007) late UBM Scaup Lake (SCL) rhyolite eruption is significant because it marked the geochemical transition to the most recent CPM volcanic cycle at Yellowstone Caldera (Fig. 3.2 B) (Vazquez et al. 2009; Till et al. 2019). This eruption, which occurred after a ∼220 ky gap in the igneous record, emplaced 2−3 km3 of glassy rhyolitic lava with 12−15 vol% crystals, consisting of sanidine (40%), plagioclase (30%), quartz (20%), pyroxene (7%), and Fe-Ti oxides (3%) (Till et al. 2019) (see Table 3.1 for bulk composition). Zircon crystallization ages for SCL are quite young, with only a
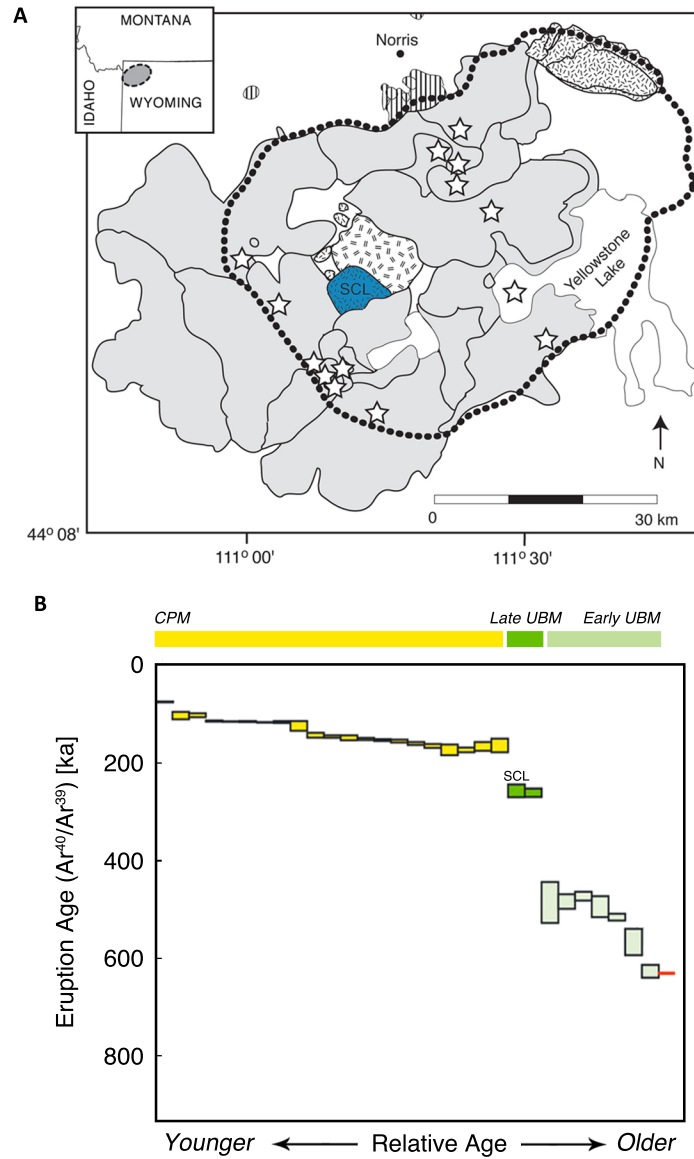
Figure 3.2: A. Location of the Scaup Lake (SCL) rhyolite flow (blue) in Yellowstone caldera (present-day extent marked with dotted line). Subsequent Central Plateau Member (CPM) rhyolites in gray. Stars indicate source vents for CPM flows. After Vazquez et al. (2009) Figure 1, Till et al. (2019) Figure 1, and originally based on the geologic mapping of Christiansen (2001). B. Diagram showing the sequence of eruptions at Yellowstone since the last caldera-forming eruption (red bar). Box height indicates 2 sigma error in $^{40}Ar/^{39}Ar$ eruption age. After Till et al. (2019) Figure 1. Data: Christiansen et al. (2007), Matthews et al. (2015), Stelten et al. (2015, 2018), Till et al. (2019).

few crystal cores dating to earlier than 500 ka (Till et al. 2019), suggesting that magmatic conditions before SCL's eruption were warm enough to dissolve essentially all leftover zircons from early UBM magmas, or that the late UBM eruptions sourced different magma pods that evolved exclusively after the earlier eruptions.

Geochemical analyses indicate progressive compositional and isotopic evolution from Scaup Lake through the subsequent CPM sequence, suggesting a linked petrological history marked by infusions of melted crust (Girard and Stix 2009, 2010; Vazquez et al. 2009; Watts et al. 2012; Loewen and Bindeman 2015; Stelten et al. 2017; Till et al. 2019). Previous diffusion chronometry on Scaup Lake sanidine indicates the timescale between the system's last chemical perturbation and eruption could be as short as a few decades or a few months (Till et al. 2015).

Table 3.1: Scaup Lake rhyolite whole rock

Oxide	wt%
SiO_2	73.26
TiO_2	0.26
Al_2O_3	12.51
FeO^{tot}	1.69
MnO	0.04
MgO	0.23
CaO	0.84
Na_2O	3.30
K_2O	5.18
P_2O_5	0.04

XRF data Girard & Stix (2009)

3.2.1 Scaup Lake Clinopyroxene

Fe-rich clinopyroxene (cpx) is the most abundant mafic phenocryst mineral in Yellowstone Plateau rhyolites (Christiansen 2001). Recent studies have articulated a phenomenon long-known by experimental petrologists who conduct high-silica phase equilibria studies: cpx, while considered to be a high temperature, mafic mineral, is not limited to high temperatures in these systems. Instead,

cpx stability extends from the liquidus perhaps down to the solidus in high-silica magmatic systems. Experiments, as well as a new clinopyroxene-liquid geothermometer, confirm that cpx is stable at or near the solidus to temperatures below 700°C in rhyolitic magmas (Almeev et al. 2012; Gardner et al. 2014; Bolte et al. 2015; Iacovino et al. 2015; Befus and Gardner 2016; Brugman and Till 2019). This makes cpx an appealing choice to compare to preexisting diffusion timescale estimates from sanidine (e.g., that of Till et al., 2015).
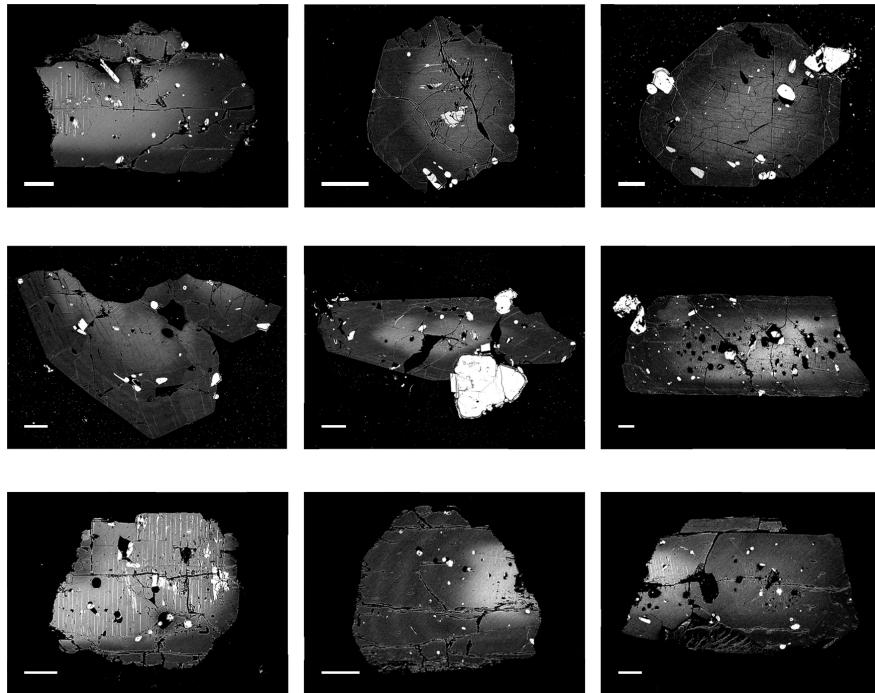
Figure 3.3: Backscattered electron (BSE) images of representative Scaup Lake clinopyroxene. Crystals are reverse-zoned; lighter areas in the clinopyroxene correlate with higher Fe content. Scale bars are 100 microns.

SCL cpx are euhedral, isolated, and commonly ∼0.5 mm, with some phenocrysts > 2 mm. Examination of SCL cpx via backscattered electron imaging (BSE) shows Fe-Mg reverse-zoned crystals with fine outer zones (Fig. 3.3). Some crystals exhibit exsolution lamellae and some cpx are included in quartz and sanidine, indicating that cpx crystallization happens at the same time as, or earlier than that of these felsic minerals. This is consistent with experimental work done on Yellowstone CPM phase relationships, in which cpx was found to crystallize after sanidine and only ∼20°C before

quartz (Befus and Gardner 2016). This overlap in crystallization intervals allows for the possibility of correlating recorded timescales between these minerals.

Like many high-silica magmatic system cpx, SCL cpx have extremely low Al_2O_3 ($\sim$0.6 wt%, Table 3.2, Fig. 3.4) (Brugman and Till 2019). In fact, the younger the post-caldera lava, the more FeO-rich and Al_2O_3-poor the cpx becomes, a trend that does not appear to correlate with cpx crystallization temperature (Fig. 3.4). As low Al content in these cpx is a result of their low Ca content (the resulting charge imbalance with O3 oxygen requires more Si to occupy tetrahedral sites to compensate) (Salviulo et al. 2000) it is likely that low bulk CaO content (< 0.5 wt% for CPM lavas; Girard and Stix 2010) as well as the crystallization of plagioclase (30% of SCL crystals; Till et al. 2019) indirectly caused this depletion of Al in cpx. Low Al in basaltic clinopyroxene has been correlated to slow cooling rates (Mollo et al. 2010), suggesting the Yellowstone post-caldera cpx may grow more slowly than high-Al cpx. Slow, constant growth could allow a crystal to capture a higher resolution record of chemical changes in the melt, however this same information fidelity presents problems when attempting traditional diffusion modeling (see "Diffusion Chronometry Methods").

Table 3.2: Scaup Lake clinopyroxene rim composition

Oxide	wt%
SiO_2	51.71
TiO_2	0.18
Al_2O_3	0.66
Cr_2O_3	0.00
FeO^{tot}	15.36
MnO	0.75
MgO	11.10
CaO	19.92
Na_2O	0.31
K_2O	0.03
P_2O_5	0.04

EPMA data; n = 122
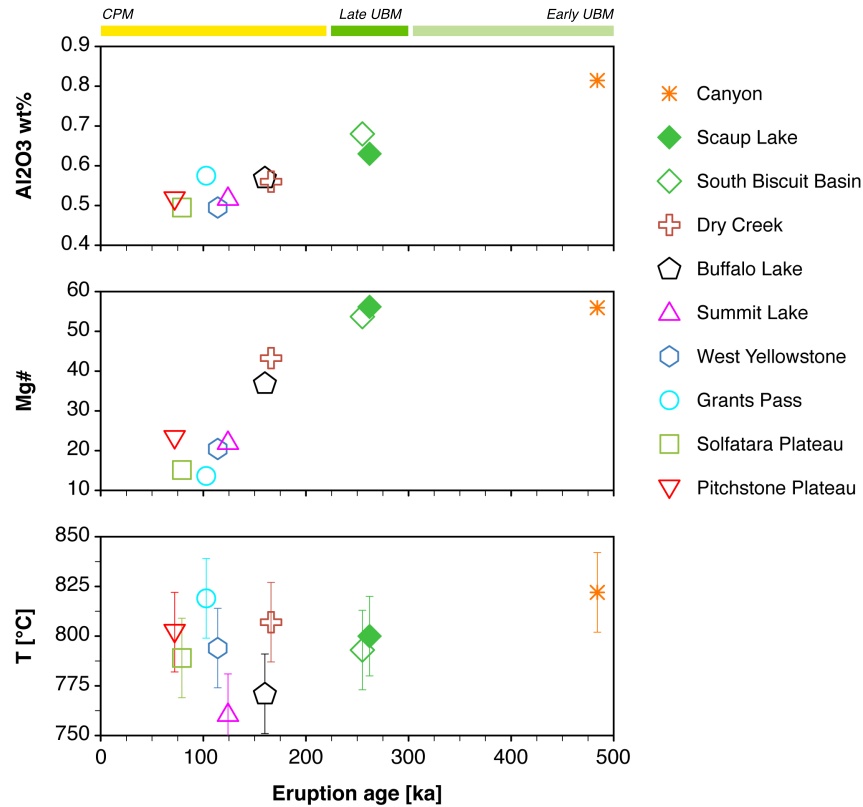
Figure 3.4: Al_2O_3 wt%, Mg#, and clinopyroxene-liquid temperature (Brugman and Till 2019) of Yellowstone clinopyroxene versus $^{40}Ar/^{39}Ar$ eruption date in ka before present. Member names as suggested by Till et al. (2019). Data from Christiansen (2001), Vazquez et al. (2009), Girard and Stix (2010), Pritchard and Larson (2012), Befus and Gardner (2016).

3.3 Analytical Methods

3.3.1 Sample Preparation

In situ EPMA analyses (Table B.1, B.2) were conducted on carbon-coated SCL rhyolite thin sections. For LA-ICP-MS and SIMS analyses, single clinopyroxene crystals with intact faces were hand-picked under stereo microscope from a < 1 mm fraction of separates from Scaup Lake lava samples YCV-08 and 12CTYC-01 collected under National Park Service research permits YELL-2012-SCI-5920 and YELL-2015-SCI-6078. The single crystals were mounted in epoxy with c-axes aligned and paral-

lel to the surface of the mount. Cpx for NanoSIMS analysis were prepared in the same way with the exception that the crystals were mounted in epoxy wells drilled into 1″ aluminum rounds to reduce outgassing under high vacuum. Crystal separate mounts were polished to expose central cross-sections of the cpx using an auto-polisher and diamond suspension pastes to 0.25 microns, then were gold-coated.

3.3.2   LA-ICP-MS and EPMA

Cpx elemental abundances were measured at the Group 18 laboratory at Arizona State University (ASU) using a Thermo Scientific iCAP Qc quadrupole ICP-MS with a Photon Machines Analyte G2 ArF Excimer 193nm UV laser with HelEx ablation cell.

Measurements of cpx and glass (Table B.1, B.2) were performed on the JXA-8530F EPMA at ASU's Eyring Materials Center using an accelerating voltage of 15 kV and beam current of 15 nA. Spot sizes were 1 micron for crystals and 10 microns for glass. The EPMA was also used to identify intracrystalline zone boundaries of interest via backscattered electron BSE images.

3.3.3   SIMS and NanoSIMS

Intracrystalline zone boundary profiles of the elements of interest were measured with the Cameca IMS 6f SIMS at ASU's National Science Foundation (NSF) Multi-User Facility. SIMS profiles were measured with a primary beam intensity of 10 nA of O– gated to 4 microns, with $\leqslant$ 8-micron step size between analysis points.

ASU's NSF Multi-User Facility Cameca 50L NanoSIMS was used to complete linescans across SCL cpx intracrystalline boundaries. Single rim profiles as well as consecutive rim profiles were measured to provide an extra check in order to confirm modeling results. Duplicate profiles were measured of some zone boundaries as an additional check. 60 linescans, each including measurements of Mg, Si, Fe, Ce, and Dy, were measured from 16 cpx grains. These represent some of the first cpx trace element analyses conducted via NanoSIMS, and so a variety of settings were explored. Linescans were 37–77

microns long with 0.2–1 micron spacing between analysis points taken with a beam size of 500–750 nm. Instrument settings included apertures D1-1, D1-2, or D1-3 with at a primary beam intensity of 50 pA of O−. EPMA secondary-electron images (SEI) of analyzed areas were used to confirm the location of the NanoSIMS linescans.

3.3.4 Geothermometry

Temperature was calculated using a clinopyroxene-liquid geothermometer specifically calibrated for the high-Fe, low-Al clinopyroxene found in high-silica igneous systems (Brugman and Till 2019). Scaup Lake clinopyroxene rims yielded a temperature of 800 $\pm$ 20°C.

3.4 Diffusion Chronometry Methods

Diffusion modelling is based on Fick's 2nd Law:

$$\frac{\partial C}{\partial t} = D \left(\frac{\partial^2 C}{\partial x^2} \right) \tag{3.1}$$

where $\frac{\partial C}{\partial t}$ is the position-independent change in elemental concentration over time, D is the diffusion coefficient (Eq. 3.2), and D is independent of C (concentration) or x (position). An element's diffusion coefficient, D, is calculated:

$$D = D_0 e^{\text{-E/RT}} \tag{3.2}$$

where D_0 is a preexponential factor, E is the activation energy, R is the gas constant, and T is the temperature at which diffusion is occurring. D also depends on the magma body temperature, pressure, $f\mathrm{O}_2$, and the mineral type, element, and crystallographic direction of diffusion. Because these cpx are from the same lava and due to the care taken to prepare samples for analysis, we assume uniform pressure, $f\mathrm{O}_2$, and crystallographic direction of diffusion and therefore use Equation 2 to calculate D for all models.

We modeled 1-dimensional position- and concentration-independent diffusion in SCL cpx using both the diffusion only and growth-then-diffusion initial conditions. In all cases, the chemical profiles are first fit using the analytical solution to the diffusion equation:

$$C = C_1 + \left(\frac{C_0 - C_1}{2} \right) * Erfc \left(\frac{x}{2\sqrt{Dt}} \right) \qquad (3.3)$$

Where C_0 and C_1 represent the elemental concentrations of a given element at the left- and right-hand plateaus, respectively, D is the diffusion coefficient, t is elapsed time, and Erfc is the complimentary error function. This approach was employed in a Monte Carlo model to calculate timescales from a single element-mineral pair from a step-function initial condition. For the growth-then-diffusion case, where we do not assume a step function initial condition, we utilized a Monte Carlo forward-model. A combination of a stepping method and an initial value problem (IVP) finite differences method was employed to diffusively relax the concentration profiles through time; the measured post-diffusion profile of a faster diffusing element was forward-modelled from the measured profile of a slowly diffusing element (a proxy to the initial condition of the faster diffusion element at t = 0) (Fig. 3.5 B). In order to be directly comparable, these profiles must be scaled so their plateaus match.

Errors were calculated for both diffusion modeling approaches. For both methods, the best-fit time interval reported for each profile represents the time interval in our model search that produced the lowest RMS misfit between the measured and modeled profiles. Confidence intervals for these timescales were calculated by converting the misfit probability distribution (PDF) curves into cumulative probability (CDF) curves and locating the times at the 2.5% and 97.5% limits (Sambridge 1999; Beghein 2010), then clipping the upper error boundary to the maximum timescale calculated for the profile using a step function initial condition (see below). The misfit relationships we obtain are bounded by time = zero and are limited by the shape of the elemental profile itself, and so uncertainty bounds are reported as asymmetric confidence intervals (see further discussion in "Error").

A difficulty in modeling diffusion is the need to use an appropriate diffusion coefficient for the element-mineral pair of interest. Diffusion studies of cpx in rhyolitic systems are hampered by a lack of experimental diffusion data for the low-Al, high-Fe cpx common to high-silica systems (Brugman

and Till 2019). Higher Al contents must be charge balanced by Fe^{3+} and a vacancy ($Fe^{2+} = Al^{3+} + Fe^{3+}$ + [ ]), resulting in more point defects in the crystal lattice. This allows for faster diffusion to occur in a high-Al cpx than in a low-Al cpx with an otherwise comparable composition. Whether this relationship is borne out to low-Al, high-Fe cpx i.e., whether Fe-Mg diffusion occurs at a slower rate for the low-Al, high-Fe cpx crystallized in high-silica systems, is as yet untested. Although experimental Fe and Fe-Mg diffusion studies have been conducted to determine E, D0, and therefore D for cpx at temperatures of 800–1200°C (Azough and Freer 2000; Dimanov and Wiedenbeck 2006; Müller et al. 2013), Fe-rich augite that is low in Al has not been experimented on in this manner. An experimental study found that Fe diffuses one order of magnitude slower in synthetic Fe-free diopside than in natural low-Fe diopside at 1050°C (Azough and Freer 2000). However, we are not comfortable extrapolating this result to Fe-Mg interdiffusion in SCL natural high-Fe cpx (average Mg# = 56.3), and so modeled diffusion using D(Fe,Mn)-Mg calculated with the activation energy and preexponential factors from Dimanov and Wiedenbeck (2006) and DCe calculated with the activation energy and preexponential factors from Van Orman et al. (2001).

3.5   Results

3.5.1   Crystal-Melt Equilibria

SCL geothermometry and experimental studies on similar composition systems indicate that cpx crystallizes at or below the onset of quartz stability (Bolte et al. 2015; Befus and Gardner 2016; Brugman and Till 2019), and so the co-crystallization of cpx with quartz and sanidine is not surprising. SCL cpx have core exsolution lamellae that suggest a past period of disequilibrium, however crystals are euhedral, indicating that they were in equilibrium with the melt in the final stages of their magmatic residence time. Previous experimental studies indicate a $K_{d\,SiO_2}^{cpx-liquid}$ < 0.75 for cpx in equilibrium with rhyolitic magma (Brugman and Till 2019) and SCL analyses yield $K_{d\,SiO_2}^{cpx-liquid}$ = 0.66, suggesting equilibrium. If SCL cpx were not in equilibrium with the melt, experimental dissolution rates
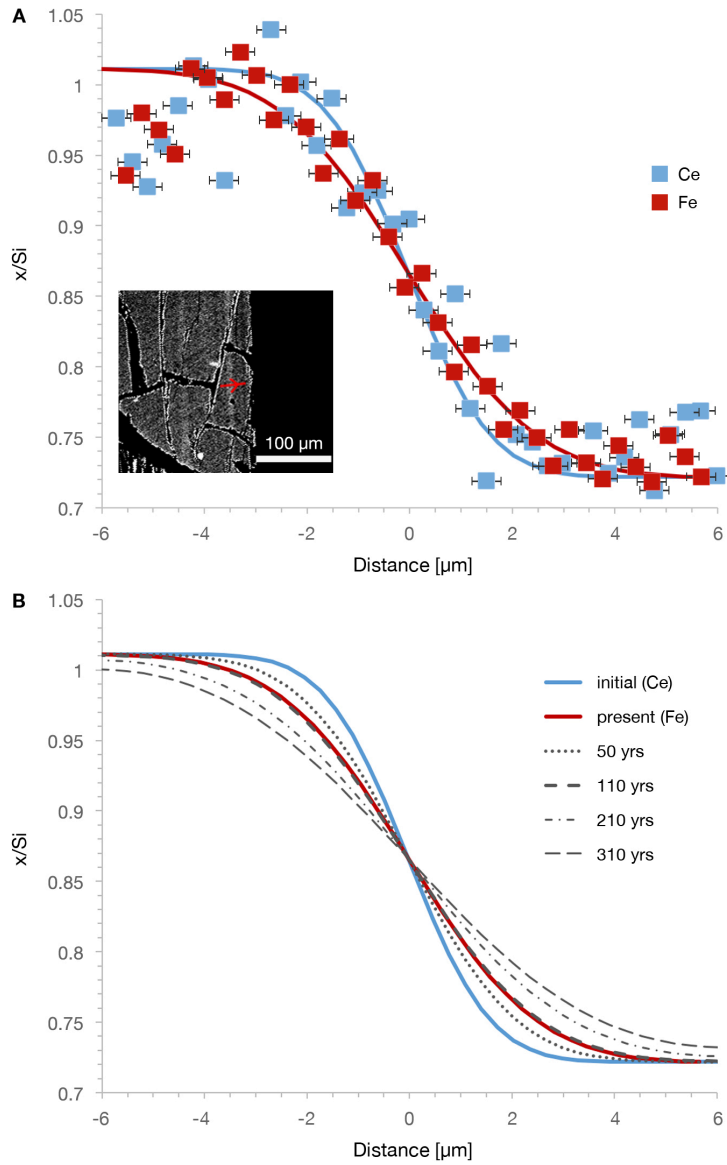
Figure 3.5: A. NanoSIMS profiles and their best-fit modeled profiles for Ce (blue) and Fe (red). Vertical errors are smaller than the symbols. Distance is measured from the profile midpoint. Inset: BSE image of a clinopyroxene grain shows location and direction (core to rim) of the NanoSIMS profile from which this profile segment was taken. B. Plot of diffusion chronometry results. Solid lines indicate the growth-then-diffusion initial condition proxy profile (blue) and present-day Fe profile (red), same as panel A. Dashed lines indicate shape of modeled profiles after the corresponding number of years. Here, 110 years (thick dashes) was the best fit.

of cpx in basaltic systems (1.05×10^{-8} m/s at 1250°C and 0.5 GPa) suggest that the cpx would have disappeared from SCL's magma body within a few years (Chen and Zhang 2009).

3.5.2 Elements Chosen for Diffusion Chronometry

We investigated a variety of possible elements in cpx with diffusivities slower than Fe-Mg, in particular cations with unfavorable charges or large radii. LA-ICP-MS analysis of SCL cpx revealed that they contained $\sim$175 ppm of Ce, such that it should be present in sufficient quantities to yield a measurable concentration profile. In order for a Ce elemental concentration profile to be used as a proxy to the Fe-Mg initial condition, it must partition into cpx in a similar manner to that of Fe and Mg, the coupled substitution of which are usually used for diffusion chronometry modeling in cpx. Fe and Mg are highly compatible elements with a partition coefficient (K_d) up to 13.1 for Fe and up to 20.4 for Mg in cpx found in rhyolite (Sisson 1991). Therefore Ce must also have $K_d > 1$ in cpx and indeed, Ce has been shown to partition compatibly into high-Fe cpx with K_d ranging from 2.5–20.9 (Mahood and Hildreth 1983; Sisson 1991). And most importantly, published diffusion coefficients for REE revealed that Ce can diffuse > 700 times slower in cpx than Fe and Mg (Van Orman et al. 2001; Costa and Morgan 2011). That diffusion study (Van Orman et al. 2001) was conducted on diopside that presumably contained trivalent Ce. We deem the application of this diffusion coefficient to SCL Fe-rich cpx appropriate given that a change in Ce oxidation state would require a compensating M1 site vacancy (an increase in which facilities diffusion) or a substitution of Al^{3+}. As SCL cpx has a very low Al_2O_3 content and relatively high CaO content ($\sim$0.6 wt% and $\sim$20 wt% respectively, Table SCL cpx) it seems unlikely that quadrivalent Ce is present in sufficient quantities to affect its diffusivity such that the element could not be used in this study.

3.6 Diffusion Modeling Results

Preliminary analyses via SIMS revealed Fe-Mg and Ce elemental profiles with quantifiable variation across intracrystalline zone boundaries, but of inadequate spatial resolution for diffusion

chronometry. The zone boundaries in the cpx were quite narrow (only a few 10s of microns wide) compared to the SIMS' spatial resolution. To mitigate convolution, at least three analysis points must be measured across the profile "ramp", the area of the elemental concentration profile showing transition from one concentration to another. Therefore, analyses with higher spatial resolution were required to sufficiently quantify concentration gradients for diffusion modeling. NanoSIMS analyses were determined to be the best tool to collect profiles for modeling diffusion in SCL cpx. Out of 60 linescans, the seven segments selected for diffusion chronometry modeling exhibited the clearest element concentration profile plateaus and ramps in locations corresponding to BSE zoning.

Preliminary calculations using our NanoSIMS data and a traditional diffusion modeling approach utilizing an analytical solution to the diffusion equation reinforced the hypothesis that the initial condition in SCL cpx cannot be approximated by a step function. Here, concentration profiles of different elements collected simultaneously in multi-collection mode on the NanoSIMS appear to be approximately the same length (Fig. 3.5 A), which is not possible for elements that differ in diffusive rate by > 700x Mg (Van Orman et al. 2001; Costa and Morgan 2011). After the same amount of time, faster-diffusing elements should have longer ramps than those of slower-diffusing elements. Additionally, if all elements began diffusing from a step function, different elements' concentration profiles across the same zone boundary should give the same diffusive timescale. However, the measured profiles from different elements yielded timescales that deviated by at least one, and often multiple, orders of magnitude. Together, the indistinguishable length of the profiles and the large variance in traditional diffusion chronometry timescales strongly indicate that SCL elemental concentration profiles across intracrystalline zone boundaries recorded growth-then-diffusion.

Thus, we employed Ce to determine the initial condition in our finite element diffusion approach to model diffusion timescales from Fe. Because we assume the two elements' initial profile shapes are the same, we therefore assume that although the surrounding melt's composition changed during crystal growth, there was no relative change in the concentration of these two elements to each other. This assumption also implies that no boundary layer formed around the crystal, which is generally a result of crystal growth that outpaces the ability of the surrounding melt to diffuse elements to the
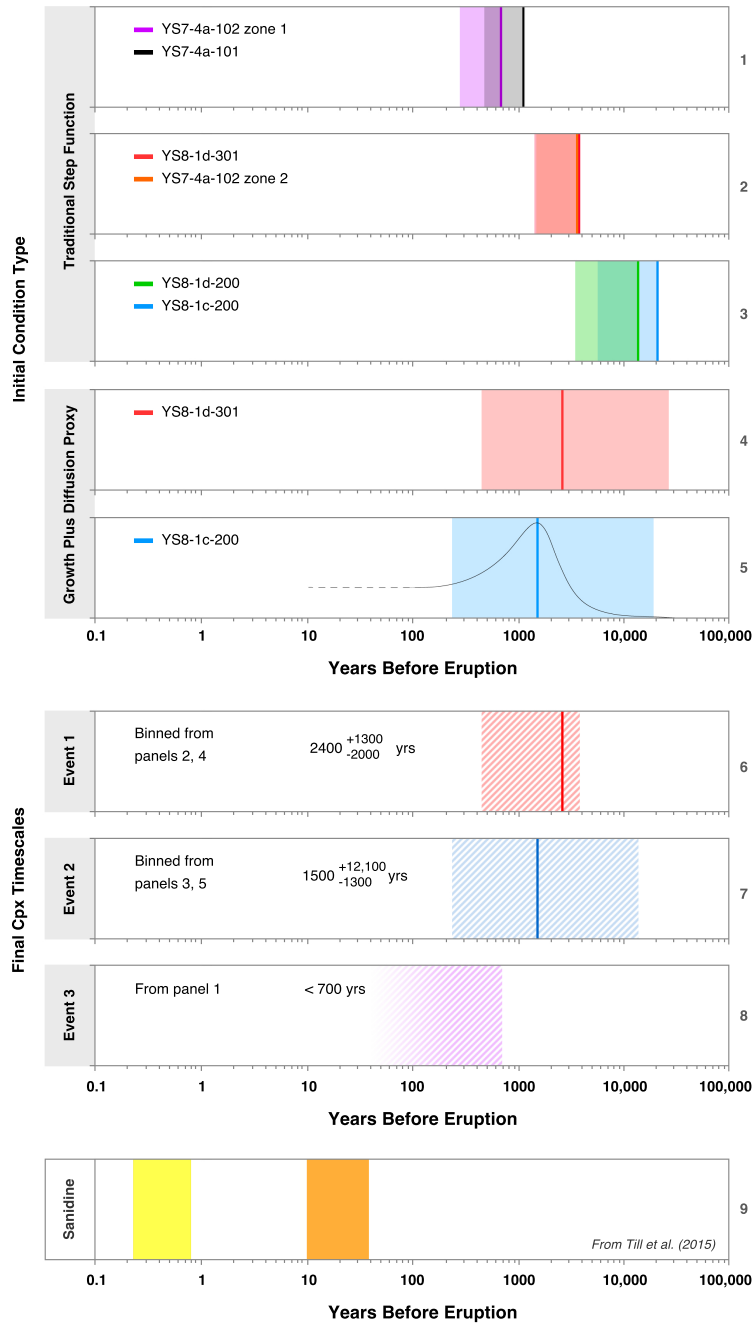
Figure 3.6: Diffusion chronometry modeling results for Scaup Lake cpx rims using a traditional step function (panels 1–3) or growth plus diffusion (panels 4–5) initial condition. Solid lines indicate best fit times (maximum possible times for panels 1–3, actual times for panels 4–5) and shaded areas show 95% confidence intervals. The red profiles in panels 2 and 4 and the blue profiles in panels 3 and 5 are the same NanoSIMS profiles, respectively, modeled using each of the two types of initial conditions. Warm colored profiles (panels 2, 4) and cool colored profiles (panels 3, 5) were binned together to calculate the final timescales in panels 6 and 7. Panel 8 shows maximum timescale for the event recorded by the profiles in panel 1. Panel 4 shows probability distribution function curve from which the times and error were derived. Panel 9 shows timescales from sanidine rims as reported by Till et al. (2015).

49

growing crystal edge. We deem these to be acceptable assumptions due to the low Al content of SCL cpx (average 0.63 wt% Al and 0.0527 CaTs), a characteristic that has been linked to low degrees of undercooling in basalt and should therefore result in crystal growth as slow, or slower, in rhyolitic systems (Mollo et al. 2010).

Our growth-then-diffusion initial condition proxy method differs from the binary-element diffusion modeling (BEDM) method of Morgan and Blake (2006). That study cleverly avoids the problem of determining the initial condition by using forward modeling of a slower diffusing trace element to match the absolute amount of diffusion of a faster diffusing trace element in order to determine magmatic residence times (Morgan and Blake 2006). Here however, we use the shape of the slower diffusing, similarly partitioning element as a proxy to the faster diffusing element's initial condition. Suitable profiles for our method were selected according to the following criteria: adequate plateaus and inclusion of at least three data points on the ramp, which is required to mitigate convolution and fit a curve on a short enough timescale (Morgan and Blake 2006) to be reasonable for SCL (e.g., less than the difference in time between the last caldera-forming eruption and the eruption of SCL). Only two profiles were modeled using our growth-then-diffusion initial condition proxy method because even with the high spatial resolution of the NanoSIMS, most SCL cpx intracrystalline zone boundary profiles were too narrow to yield enough data points to satisfy these conditions. We look forward to further refinement of NanoSIMS settings and techniques as well as future analytical instruments that will be able to further resolve these nano-scale features.

Profiles modeled using the growth-then-diffusion initial condition proxy method gave timescales of $1500^{+17,200}_{-1300}$ and $2400^{+25,800}_{-2000}$ (95% confidence, Fig. 3.6 panels 4–5). The same profiles modeled using the traditional step function initial condition gave maximum timescales of $20,700^{+71,400}_{-14,900}$ and $3700^{+91,200}_{-2400}$, respectively (95% confidence, Fig. 3.6 panels 2–3). Profiles that could not be modeled using the growth plus diffusion initial condition proxy were modeled using the traditional step function initial condition and yielded maximum timescales that were consistent with already-modeled profiles (Fig. 3.6 panels 1–3).

3.7   Discussion

As expected, consecutive rim profiles from the same crystal give older best fit or maximum times proceeding from rim to core e.g., rim-ward profile YS7-4a-102 zone 1 (Fig. 3.6 panel 1, purple) versus older core-ward profile YS7-4a-102 zone 2 (Fig. 3.6 panel 2, orange) and rim-ward profile YS8-1d-301 (Fig. 3.6 panels 2 & 4, red) versus older core-ward profile YS8-1d-200 (Fig. 3.6 panel 3, green). We also see correlations between outer zone boundaries measured in two different locations on the same crystal such as profiles YS7-4a-102 zone 1 and YS7-4a-101 (Fig. 3.6 panel 1, purple and black respectively), as well as correlations between outer zone boundaries from different crystals e.g., YS8-1d-301 and YS7-4a-102 zone 2 (Fig. 3.6 panel 2, red and orange respectively) and YS8-1d-200 and YS8-1c-200 (Fig. 3.6 panel 3, green and blue respectively). These results not only provide a check to make sure our diffusion timescales make sense but also illustrate that the outermost measurable intracrystalline zone boundaries for a given mineral are not necessarily the last chemical perturbations experienced by the magmatic system. Indeed, the outermost measurable intracrystalline zone boundaries for a given mineral crystal are not necessarily the last chemical perturbations experienced by that type of mineral in a given magmatic system.

Diffusion modeling for SCL cpx yielded three rim zone age populations representing three separate events at 2400^{+1300}_{-2000} years, $1500^{+12,100}_{-1300}$ years, and a maximum of 700 years ago (Fig. 3.6 panels 6−8). It is not possible to change these populations by combining timescales from, for example, panels 1 and 2; there are unavoidably three separate chemical perturbation events because each bin contains a timescale from a crystal with two consecutive zones, the other of which yielded a timescale in another event bin (see above).

Figure 3.6 also illustrates the difference between the best time calculated using the growth-then-diffusion initial condition proxy (panels 4−5) versus the maximum possible time calculated using a step function initial condition for the same profiles (Panels 2−3, YS8-1c-200 in blue and YS8-1d-301 in red). Note that for profile YS8-1c-200 the maximum timescale aligns nicely with the upper end of the 95% confidence interval for the growth-then-diffusion best time (Fig. 3.6 panels 3 & 5, blue). However, the maximum timescale should not be considered a shorthand for determining the error

envelope for profiles that result from growth-then-diffusion, as there is no correlation between the maximum time and the upper end of the best time error envelope for profile YS8-1d-301 (Fig. 3.6 panels 2 & 4, red). Moreover, if these maximum times were not presented as such and instead were suggested to be best times, the proposed timeline of events for SCL would be erroneously shifted to far longer times than actuality. For example, if we reported the timescale for Event 2 based on the step function initial condition modeling whose results are shown in Figure 3.6 panel 3, we might average these two timescales, giving a time for Event 2 of $17,100^{+76,500}_{-12,600}$ years. The low end of this timescale's 95% confidence interval overshoots our best time from the growth-then-diffusion initial condition proxy method for Event 2 of 1500 years by over an order of magnitude.

Because we are interested in comparing timescales from SCL cpx rims to timescales from other mineral rims, our reported best timescales were modeled by propagating all D error contributors (E, D0, and T) as discussed below.
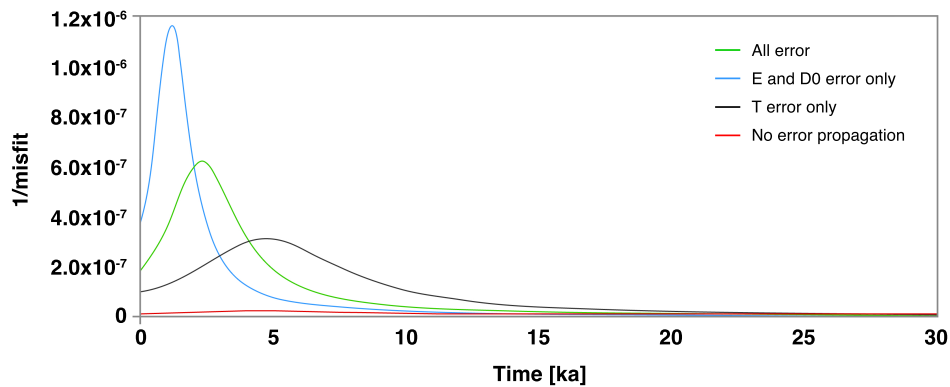
Figure 3.7: Plot of 1/misfit versus modeled time comparing the results from various levels of error propagation.

3.8 Error

3.8.1 Sources of Error

Here we have used Monte Carlo simulations to account for and compare sources of error. The first source of error is the selection of the physical geometry of the profile when using the analytical solution to the diffusion equation (Eq. 3.3). C_0 and C_1 for each measured profile can be estimated by either, 1) visually selecting a range of concentration values for which a horizonal line would make sense for a plateau; or 2) averaging the points along the purported plateau segment of the profile and then using the analytical error of the data collection method to create a $\pm$ 1 sigma range of concentration values. Our calculations show no significant difference in misfit between the two methods if the former is reasonably constrained (average difference of misfit = 2.3 x 10^{-6}). Therefore, our Monte Carlo error estimation used a synthetic normal distribution of possible C_0 and C_1 values in a given range to fit profiles in the analytical solution model.

The second source of error is the variables used to calculate the diffusion coefficient (Eq. 3.2), which include temperature (T), activation energy (E), and the preexponential factor (D0). T is calculated with a geothermometer—these have published error values and most are at least partially based on empirical data. E and D0 are determined through experiments, and so also have associated error. To determine the effect of these individual sources of error on resulting timescales, we compare propagating 1) E, D0, and T; 2) E and D0; or 3) T only. We can also examine the error inherent in our method by choosing to propagate none of these. The effect of these is illustrated in Figure 3.7, where 1/misfit is plotted so the best fit is intuitively at the peak of the plotted curve. The broad and subdued peak of "T error only" (Fig. 3.7, black) indicates the large degree of uncertainty that this variable introduces to the resulting timescale calculation (range of 95% confidence interval $\sim$24 ka), whereas the sharp, narrow peak of "E and D0 error only" (Fig. 3.7, blue) suggests a minor contribution to uncertainty (range of 95% confidence interval $\sim$18 ka). "All error" (Fig. 3.7, green) shows the effect of propagating E, D0, and T and is appropriately intermediate to the "T error only" and "E and D0 error
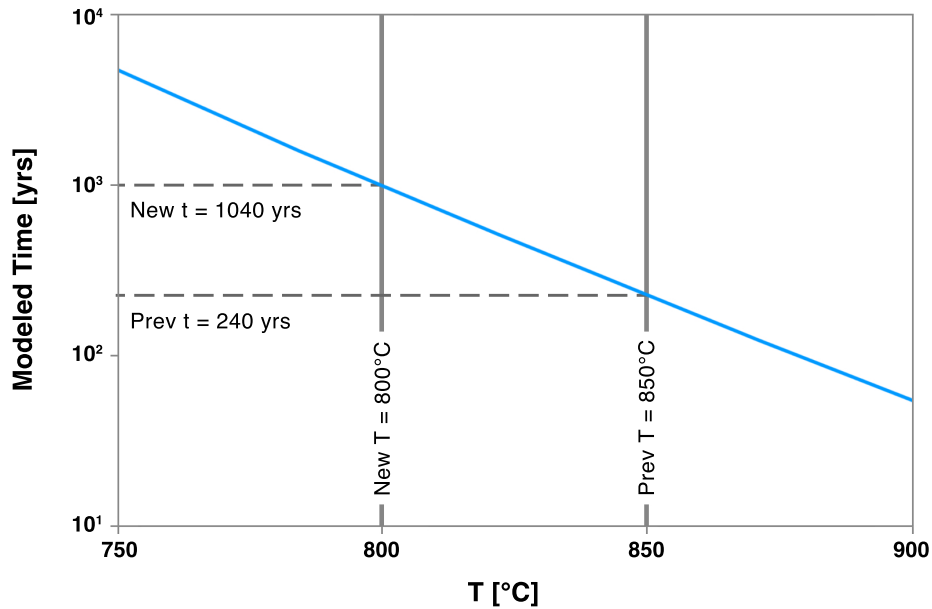
Figure 3.8: The change in modeled diffusion timescale as a function of model temperature for a Scaup Lake cpx NanoSIMS element concentration profile. A traditional step function initial condition was used for this example. Vertical and horizontal gray lines call attention to the difference in timescale (dashed) that results from a small change in modeling temperature (solid).

only" PDFs. Without error propagation (Fig. 3.7, red), only one D is modeled for the given range of times. Because of this, only one T is explored, and thus the overall match in fit between the best-fit modeled profile and the measured profile is relatively poor, as indicated by the broad, flat PDF.

Unsurprisingly, the greatest source of error in diffusion chronometry is the error associated with the temperature at which modeling will be performed, or more precisely, the error associated with the mineral geothermometer used to calculate this temperature. The large influence of temperature on diffusive timescales is due to the Arrhenius relationship of T to D (Eq. 3.2) and reflects an exponential increase in diffusion rate as point defects in the crystal lattice increase with temperature; a ΔT of just 50°C can result in a Δt of approximately one order of magnitude (Fig. 3.8). In Figure 3.9 we examine the effect of temperature on resulting timescales by modeling via our finite difference method and propagating only T error. Note that while there is generally one lowest value for the misfit between the modeled and measured profile, multiple temperature-time pairs may produce model profiles that yield the same misfit value (Fig. 3.9, black region).

This result highlights a fundamental principle underlying diffusion modeling: there is no single "best time" for a given elemental diffusion profile. There is a single best fit profile (a shape that produces the lowest misfit), but that profile can be arrived at via any of a number of degenerate combinations of time and D, of which T is a variable. Although a single time for a profile cannot be determined, it is possible to identify a region of qualifying solutions (Fig. 3.9, black region) and then constrain the timescales represented therein using known ages of temporally adjacent eruptions, as well as logic based on observed petrographic relationships and geothermometry.
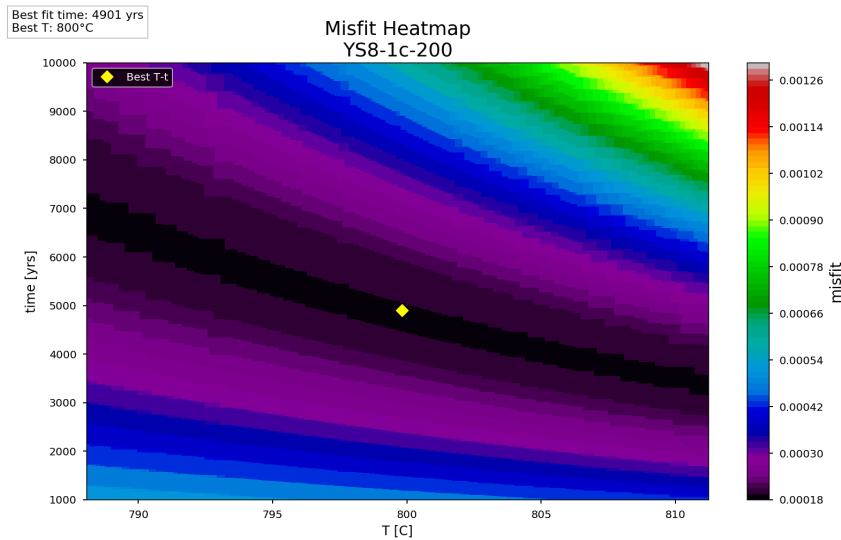
Figure 3.9: Time vs. temperature (T) heatmap showing lowest misfit as darker colors. Plot produced by modeling only the propagation of T error, which was determined by the geothermometer's error. Note that although there is a best time for the calculated T of 800°C, there are other times that represent equally good fits within the range of Ts given by the geothermometer's error.

3.8.2 Recommendations for Error Reporting

As illustrated in Figure 3.7, modeling, at minimum, multiple Ds based on propagating the T error reported by the geothermometer gives the maximum possible error envelope that is reasonably constrained and may be used to compare timescales from different minerals, lavas, or magmatic systems that are modeled using different methods. Propagating all D error contributors (E, D0, and T) allows

for comparison of timescales modeled using the same method. This tiered approach is modeled after that used by the geochronology community (Horstwood et al. 2016). Modeling diffusion from a step-function initial condition is recommended to find an absolute upper limit on error, as this method will produce the maximum timescale possible for the measured profile—although the true relevance of this value depends on whether the profile is partially the result of crystal growth. We recommend reporting timescale uncertainty in the form of asymmetric 95% confidence intervals clipped to this maximum as described in "Diffusion Modeling Procedure" and as reported in "Results."

3.8.3   Shape of PDF and Asymmetric Confidence Intervals

Expressing uncertainty as asymmetric confidence intervals are necessitated by the nature of the curve being fit and the diffusive relaxation process being modeled. Here PDFs do not always look like bell curves; they tend to have small amplitudes and have higher tails to the left than to the right (Fig. 3.7). The small amplitude is a result of the profile's plateaus. The modeled curve will necessarily match the points along much of the plateau, and so the misfit for these points will always be low, and similar from run to run. Since these points will always be fit by the modeled curve, the misfit for a reasonably-constrained model run (in terms of time and D) will never equal zero. The "goodness" of fit therefore is overwhelmingly controlled by the fit of the points along the ramp, although at least one point along the ramp (at the ramp midpoint) will be similar from run to run. Thus, the best fit modeled profile (the modeled profile with the lowest misfit) will not have a drastically lower overall misfit score than that of a moderate fit.

PDFs tend to have higher tails towards time = 0 for a similar reason as their small amplitude. When checking for misfit against the measured elemental diffusion profile, the probability to the left of the peak will not reach zero because the plateaus should always be well-fit, and so as discussed above, there is a threshold misfit value for well-fit plateaus but a poorly fit ramp. Conceptually, this means that in the left-of-peak space of shorter times, it is within the realm of possibility that a post-diffusion profile began as its measured shape and no analytically resolvable diffusion took place during that time.

Probability to the right of the peak (towards higher times) can reach a higher misfit (lower 1/misfit) value than to the left because as longer times are modeled, the modeled ramp width increases to wider than the ramp of the measured profile. This results in severe misfit between points that are on plateaus in the measured profile but are being compared to points on the ramp in the modeled profile. Often right-of-peak probability will approach but not reach zero because for a model run in a well-constrained time range, the plateau extrema (points at the beginning and end of the profile) should still be matched.

3.9 Implications for the Scaup Lake Rhyolite

The most recent magmatic events recorded by minerals in the Scaup Lake rhyolite are of interest because it is possible these events led to its eruption 220 ky after the early UBM sequence (Fig. 3.2). During long periods of quiescence, cooled magma bodies may exist as a near-solidus mush containing > 50% crystals (e.g., Hildreth 2004; Cooper and Kent 2014; Rubin et al. 2017). In order to become eruptible, the magma body must be rejuvenated e.g., remelted by adding heat or volatiles. Rejuvenation can be identified via disequilibrium textures, such as the aforementioned intracrystalline compositional zonation. At SCL, we see abundant evidence of late-stage disequilibrium as represented by reverse-zoning in the cpx (Fig. 3.3), sanidine (Till et al. 2015), and zircon (Bindeman and Valley 2001; Bindeman et al. 2008) as well as oscillatory zoning, resorbed cores, and truncation of zones that indicate previous dissolution.

3.9.1 Comparison of SCL Clinopyroxene and Sanidine

To investigate the timing of the last events recorded by minerals before eruption, here we compare diffusion timescales from the rims of SCL cpx to those from the rims of SCL sanidine. Prior work by Till et al. (2015) on sanidine from SCL was the first published study to use NanoSIMS to capture intracrystalline zone boundary profiles for diffusion dating. That work noted similar widths of profiles from elements with different diffusivities, which suggested the profiles were a result of

growth-then-diffusion. Using both feldspar growth rates and traditional step function initial condition diffusion modeling, that work reported two populations of sanidine rejuvenation-eruption times: 1.5–10 months and 10–40 years, which are short but consistent with models of eruptive timescales initiated by near-liquidus intrusions (Simakin and Bindeman 2012).

We sought to determine whether the SCL cpx show rejuvenation-eruption timescales consistent with the history recorded by SCL sanidine. Petrography and experiments on similar systems indicate that these minerals should have overlapping stability fields. Indeed, cpx-liquid geothermometry produces cpx rim temperatures of $800 \pm 20°$C and 2-feldspar thermometry gives sanidine rim temperatures of $819 \pm 20°$C (Elkins and Grove 1990; Wen and Nekvasil 1994; Brugman and Till 2019), indicating that these two minerals likely co-crystallized, and therefore potentially recorded the same changes in magma body conditions.

Our results show that the SCL magma source experienced multiple late rejuvenation events (Fig. 3.6). This is not immediately apparent when examining SCL sanidine, as the outermost zone of these is broad ($\sim$500 microns) and appears to be homogenous. However, upon closer examination, this outer zone is composed of several fine, lower-contrast, oscillatory zones (Till et al. 2015), implying the sanidine were exposed to varying magma conditions more recently than 1.5–10 months and/or 10–40 years before eruption.

The outermost zones of SCL cpx and sanidine did not yield the same timescales. As shown in Figure 3.6, SCL sanidine do not record timescales > 100 years in their outermost rims (panel 9) and the youngest SCL cpx rim timescale is a maximum of 700 years (panel 8). While it is possible that this cpx timescale, denoted "Event 3" (Fig. 3.6 panel 8), could encompass the oldest reported SCL sanidine timescale of 10–40 years, it is more likely that these are separate events. Additionally, feldspar geothermometry indicates a 20–50°C heating trend from core to rim (Till 2017) that is not replicated in the cpx rims. This late sanidine growth and apparent change in recorded temperature is likely the result of degassing-driven crystallization, likely associated with ascent (Humphreys et al. 2016; Till 2017). The region of fine (< 50 micron) oscillatory zoning in SCL sanidine rim-ward of the 1.5–10 months and 10–40 years zone boundary is quite broad ($\sim$500 microns), implying that very fast growth occurred here. Sanidine growth in rhyolitic systems occurs at 10^{-8}–10^{-12} m/s (Swanson 1977),

and so the thick rim observed in these minerals could have grown on the order of days (Till 2017). If the crystal grows faster than the melt can deliver elements to the growth surface, this results in a depletion of compatible elements in the surrounding melt (Zhang 2008). As the diffusion rate of SiO_2 through dry rhyolitic melt is $\sim 10^{-13}$ m^2/s (Zhang 2008), these fine, oscillatory zones could be the result of the formation of boundary layers around the sanidine crystal as it grew. The crystal was moved to a less-depleted melt region during ascent where it was free to quickly grow until a boundary layer formed again, and so on. SCL cpx, on the other hand, exhibit relatively short distances between the modeled rim zone boundary and crystal edge ($\sim 20-70$ microns) that may be due to slow crystal growth of the mineral at these conditions. Cpx growth in basaltic systems is $\sim 10^{-9}$ m/s but is expected to be slower in lower-temperature systems as kinetic processes slow and the system approaches the solidus (Orlando et al. 2008). Experiments and geothermometry confirm cpx was stable at 800°C (Almeev et al. 2012; Gardner et al. 2014; Bolte et al. 2015; Iacovino et al. 2015; Befus and Gardner 2016; Brugman and Till 2019), but whether cpx is able to grow fast enough at the lower end of its stability field to record variable chemistry at the spatial resolution of existing analytical techniques is unknown. Therefore, the simplest explanation is that by 10$-$40 years before SCL erupted, cpx was growing slowly enough that the resulting increase in crystal size is undetectable given the spatial resolution of our current analytical methods.

Given the robustness of the diffusion modeling approaches and error propagation described herein, this is an intriguing result, as it suggests that the last event recorded by a mineral is not necessarily the last event experienced by the magmatic system. In fact, we suggest it is more accurate to say that the last event *we are able to measure in each mineral* is not necessarily the last event experienced by the magmatic system.

3.9.2 Scaup Lake Rhyolite History

The cpx and sanidine of the Scaup Lake rhyolite display a complex magmatic history of periodic disequilibria and heating events. These minerals have several, if not dozens, of intracrystalline zones that have survived conditions that dissolved part of the mineral, suggesting a magma body that was

in constant flux. Although it is possible that these mineral crystals could have been moving within the magma body to regions of different chemistry in the > decades before eruption, this seems unlikely given the viscosity of rhyolitic magma ($\sim 10^{10}$ Pa·s; Hess et al. 2008). It is more likely that the chemical changes recorded in SCL cpx and sanidine (excluding the fine, oscillatory sanidine rim zones) are the result of multiple, slow changes to the local magma body conditions such that crystals were able to record these changes in their new growth as they experienced them.

Zircon ages and compositions indicate that SCL is estranged from the early UBM lavas, possibly due to a period of heating and dissolution (Till et al. 2019). SCL cpx and sanidine record two different instances of massive rejuvenation by more primitive material, as indicated by broad regions of reverse zoning as well as evidence of crystal dissolution in the sanidine. For sanidine, this is the rim zone boundary that gives timescales of 1.5–10 months and 10–40 years (Till et al. 2015). For cpx, this is the bright-core-dark-rim boundary that was not explored in this work (Fig. 3.3), but is certainly older than the oldest cpx rim timescale we found, which was 2400^{+1300}_{-2000} years.

If the broad and intermediate zones do represent rejuvenation of the SCL magma body by juvenile rhyolite derived from basaltic underplating as suggested by previous workers (e.g., Stelten et al. 2017), the implication is that several instances of juvenile rhyolite extraction occurred, and thus perhaps there were several instances of primitive magma intruding into the crust. As the SCL rhyolite was erupted $\sim$220 ka after the previous UBM eruption, it is notable that it seems to have taken many such events for an eruption to be triggered. This indicates that each incremental rejuvenation event added a relatively small amount of material/heat until the SCL magma body became eruptible (< $\sim$40% crystals; Gelman et al. 2013), critical overpressure was reached, and the magma began to degas and ascend, triggering degassing-driven fast crystallization in the sanidine (Till 2017) but not in the cpx. The SCL rhyolite was erupted 262 ka (Christiansen et al. 2007) but its reservoir was not emptied; SCL is compositionally linked to the CPM lavas, which erupted only $\sim$90 ka later. The bulk rock and isotopic compositions of SCL and CPM lavas and the reverse oxygen isotopic zoning of zircons (i.e., low-δ^{18}O crystal cores and high-δ^{18}O rims) point to a common hydrothermally-altered protolith for these lavas that experienced multiple episodes of recharge by juvenile rhyolites that were themselves

generated by mantle-derived material (Bindeman et al. 2008; Girard and Stix 2009; Stelten et al. 2017).

3.10 Conclusions

Because each mineral's crystallization interval and growth rate constrains its ability to record magmatic events, an understanding of the phase equilibria and temperature history of the system is essential to interpreting diffusion chronometry results. It is important to recognize that SCL cpx are not lacking quantifiable evidence of the most recent magmatic events simply because they are mafic minerals and therefore are only stable at higher temperatures—based on the crystal stability inferred for cpx via geothermometry, petrography, and experiments on cpx in similar high-silica systems, cpx is demonstrably stable at low temperatures (see "Crystal-Melt Equilibria"). Timescales < 700 years are not represented in SCL cpx possibly because crystal growth was so slow at $\leqslant 800^\circ$C that it had essentially halted, or the new zone(s) is too fine to be resolved at the spatial resolution of BSE or NanoSIMS. Experimental data to constrain the crystal growth rates of cpx in rhyolitic systems would greatly enrich this conversation.

The method presented in this work is a powerful new tool for diffusion studies on systems where crystals have experienced growth-then-diffusion, a process that is likely to occur in lower-temperature, more viscous, rhyolitic systems. Timescales of rejuvenation are important, particularly for high-silica systems that may erupt explosively, because the amount of time it takes for a quiescent magma body to become eruptible informs our models of magma body dynamics and storage conditions and has implications for volcano monitoring and hazard management. Our comparison of maximum and best timescales for the same profiles (Fig. 3.6 panels 2–5) suggests that if most growth-then-diffusion profiles have been modeled using a traditional step function initial condition, the maximum times yielded by that method do not have a predictable relationship to the actual range of best times for the event, and could be used to mistakenly assign ages to events that are an order of magnitude too old. We also find that for Scaup Lake, multiple rejuvenation events occurred over the > 2400 years before its eruption was triggered, the last rejuvenation event being < 40 years before eruption.

If rejuvenation timescales are on the scale of a human lifetime as is increasingly becoming apparent (e.g., Till et al. 2015; Morgado et al. 2019; Shamloo and Till 2019), it is imperative that we compile timescale data from many individual eruptions in order to aid future forecasting efforts. Furthermore, to increase the robustness of this data, it is crucial to fully report error on these timescales to allow cross-comparison between different minerals from the same eruptions, and to compare timescales originating from different systems. Because of the degeneracy of diffusion timescales, we stress that diffusion chronometry alone cannot determine a timescale for a given process. The assumptions and simplifications common in igneous diffusion chronometry thus far may have helped the field to flourish, but they are no longer adequate for the statistics-based forecasting we wish to undertake in the future.

References

Albert, H., Costa, F., and Martí, J. (2015) Timing of Magmatic Processes and Unrest Associated with Mafic Historical Monogenetic Eruptions in Tenerife Island. Journal of Petrology, egv058.

Allan, A.S.R., Morgan, D.J., Wilson, C.J.N., and Millet, M.-A. (2013) From mush to eruption in centuries: assembly of the super-sized Oruanui magma body. Contributions to Mineralogy and Petrology, 166, 143–164.

Almeev, R.R., Bolte, T., Nash, B.P., Holtz, F., Erdmann, M., and Cathey, H.E. (2012) High-temperature, low-H_2O Silicic Magmas of the Yellowstone Hotspot: an Experimental Study of Rhyolite from the Bruneau-Jarbidge Eruptive Center, Central Snake River Plain, USA. Journal of Petrology, 53, 1837–1866.

Andersen, N.L., Singer, B.S., Costa, F., Fournelle, J., Herrin, J.S., and Fabbro, G.N. (2018) Petrochronologic perspective on rhyolite volcano unrest at Laguna del Maule, Chile. Earth and Planetary Science Letters, 493, 57–70.

Azough, F., and Freer, R. (2000) Iron diffusion in single-crystal diopside. Phys Chem Minerals, 27, 732–740.

Bachmann, O., and Bergantz, G.W. (2006) Gas percolation in upper-crustal silicic crystal mushes as a mechanism for upward heat advection and rejuvenation of near-solidus magma bodies. Journal of Volcanology and Geothermal Research, 149, 85–102.

Befus, K.S., and Gardner, J.E. (2016) Magma storage and evolution of the most recent effusive and explosive eruptions from Yellowstone Caldera. Contributions to Mineralogy and Petrology, 171.

Beghein, C. (2010) Radial anisotropy and prior petrological constraints: A comparative study. Journal of Geophysical Research, 115.

Bindeman, I.N., and Valley, J.W. (2001) Low-δ^{18}O Rhyolites from Yellowstone: Magmatic Evolution Based on Analyses of Zircons and Individual Phenocrysts. Journal of Petrology, 42, 1491–1517.

Bindeman, I.N., Fu, B., Kita, N.T., and Valley, J.W. (2008) Origin and Evolution of Silicic Magmatism at Yellowstone Based on Ion Microprobe Analysis of Isotopically Zoned Zircons. Journal of Petrology, 49, 163–193.

Bolte, T., Holtz, F., Almeev, R., and Nash, B. (2015) The Blacktail Creek Tuff: an analytical and experimental study of rhyolites from the Heise volcanic field, Yellowstone hotspot system. Contributions to Mineralogy and Petrology, 169.

Bouvet de Maisonneuve, C., Costa, F., Huber, C., Vonlanthen, P., Bachmann, O., and Dungan, M.A. (2016) How do olivines record magmatic events? Insights from major and trace element zoning. Contributions to Mineralogy and Petrology, 171.

Brugman, K.K., and Till, C.B. (2019) A low-aluminum clinopyroxene-liquid geothermometer for high-silica magmatic systems. American Mineralogist, 104, 996–1004.

Budd, D.A., Troll, V.R., Deegan, F.M., Jolis, E.M., Smith, V.C., Whitehouse, M.J., Harris, C., Freda, C., Hilton, D.R., Halldórsson, S.A., and others (2017) Magma reservoir dynamics at Toba caldera, Indonesia, recorded by oxygen isotope zoning in quartz. Scientific Reports, 7, 40624.

Chamberlain, K.J., Morgan, D.J., and Wilson, C.J.N. (2014) Timescales of mixing and mobilisation in the Bishop Tuff magma body: perspectives from diffusion chronometry. Contributions to Mineralogy and Petrology, 168.

Chen, Y., and Zhang, Y. (2009) Clinopyroxene dissolution in basaltic melt. Geochimica et Cosmochimica Acta, 73, 5730–5747.

Christiansen, R.L. (2001) The Quaternary and Pliocene Yellowstone Plateau volcanic field of Wyoming, Idaho, and Montana, 145 p. U.S. Geological Survey, Reston, Va.

Christiansen, R.L., Lowenstern, J.B., Smith, R.B., Heasler, H., Morgan, L.A., Nathenson, M., Mastin, L.G., Muffler, L.J.P., and Robinson, J.E. (2007) Preliminary Assessment of Volcanic and Hydrothermal Hazards in Yellowstone National Park and Vicinity p. 94. USGS.

Cooper, G.F., Morgan, D.J., and Wilson, C.J.N. (2017) Rapid assembly and rejuvenation of a large silicic magmatic system: Insights from mineral diffusive profiles in the Kidnappers and Rocky Hill deposits, New Zealand. Earth and Planetary Science Letters, 473, 1–13.

Cooper, K.M., and Kent, A.J.R. (2014) Rapid remobilization of magmatic crystals kept in cold storage. Nature, 506, 480–483.

Costa, F., and Chakraborty, S. (2004) Decadal time gaps between mafic intrusion and silicic eruption obtained from chemical zoning patterns in olivine. Earth and Planetary Science Letters, 227, 517–530.

Costa, F., and Dungan, M. (2005) Short time scales of magmatic assimilation from diffusion modeling of multiple elements in olivine. Geology, 33, 837–840.

Costa, F., and Morgan, D. (2011) Time Constraints from Chemical Equilibration in Magmatic Crystals. In Timescales of Magmatic Processes: From Core to Atmosphere pp. 123–159. Blackell Publishing, Ltd.

Costa, F., Chakraborty, S., and Dohmen, R. (2003) Diffusion coupling between trace and major elements and a model for calculation of magma residence times using plagioclase. Geochimica et Cosmochimica Acta, 67, 2189–2200.

Costa, F., Dohmen, R., and Chakraborty, S. (2008) Time Scales of Magmatic Processes from Modeling the Zoning Patterns of Crystals. Reviews in Mineralogy and Geochemistry, 69, 545–594.

Degruyter, W., Huber, C., Bachmann, O., Cooper, K.M., and Kent, A.J.R. (2016) Magma reservoir response to transient recharge events: The case of Santorini volcano (Greece). Geology, 44, 23–26.

Dimanov, A., and Wiedenbeck, M. (2006) (Fe,Mn)-Mg interdiffusion in natural diopside: effect of pO_2. European Journal of Mineralogy, 18, 705–718.

Druitt, T.H., Costa, F., Deloule, E., Dungan, M., and Scaillet, B. (2012) Decadal to monthly timescales of magma transfer and reservoir growth at a caldera volcano. Nature, 482, 77–80.

Elkins, L.T., and Grove, T.L. (1990) Ternary feldspar experiments and thermodynamic models. American Mineralogist, 75, 544–559.

Flaherty, T., Druitt, T.H., Tuffen, H., Higgins, M.D., Costa, F., and Cadoux, A. (2018) Multiple timescale constraints for high-flux magma chamber assembly prior to the Late Bronze Age eruption of Santorini (Greece). Contributions to Mineralogy and Petrology, 173.

Gardner, J.E., Befus, K.S., Gualda, G.A.R., and Ghiorso, M.S. (2014) Experimental constraints on rhyolite-MELTS and the Late Bishop Tuff magma body. Contributions to Mineralogy and Petrology, 168.

Gelman, S.E., Gutiérrez, F.J., and Bachmann, O. (2013) On the longevity of large upper crustal silicic magma reservoirs. Geology, 41, 759–762.

Girard, G., and Stix, J. (2010) Rapid extraction of discrete magma batches from a large differentiating magma chamber: the Central Plateau Member rhyolites, Yellowstone Caldera, Wyoming. Contributions to Mineralogy and Petrology, 160, 441–465.

——— (2012) Future volcanism at Yellowstone caldera: Insights from geochemistry of young volcanic units and monitoring of volcanic unrest. GSA Today, 4–10.

——— (2009) Magma Recharge and Crystal Mush Rejuvenation Associated with Early Post-collapse Upper Basin Member Rhyolites, Yellowstone Caldera, Wyoming. Journal of Petrology, 50, 2095–2125.

Gordeychik, B., Churikova, T., Kronz, A., Sundermeyer, C., Simakin, A., and Wörner, G. (2018) Growth of, and diffusion in, olivine in ultra-fast ascending basalt magmas from Shiveluch volcano. Scientific Reports, 8.

Gualda, G.A.R., and Sutton, S.R. (2016) The Year Leading to a Supereruption. (A.K. Schmitt, Ed.)PLOS ONE, 11, e0159200.

Gualda, G.A.R., Pamukcu, A.S., Ghiorso, M.S., Anderson, A.T., Sutton, S.R., and Rivers, M.L. (2012) Timescales of Quartz Crystallization and the Longevity of the Bishop Giant Magma Body. (N. Houlie, Ed.)PLoS ONE, 7, e37492.

Hartley, M.E., Morgan, D.J., Maclennan, J., Edmonds, M., and Thordarson, T. (2016) Tracking timescales of short-term precursors to large basaltic fissure eruptions through Fe–Mg diffusion in olivine. Earth and Planetary Science Letters, 439, 58–70.

Hess, K.-U., Cordonnier, B., Lavallée, Y., and Dingwell, D.B. (2008) Viscous heating in rhyolite: An in situ experimental determination. Earth and Planetary Science Letters, 275, 121–126.

Hildreth, W. (2004) Volcanological perspectives on Long Valley, Mammoth Mountain, and Mono Craters: several contiguous but discrete systems. Journal of Volcanology and Geothermal Research, 136, 169–198.

Horstwood, M.S.A., Košler, J., Gehrels, G., Jackson, S.E., McLean, N.M., Paton, C., Pearson, N.J., Sircombe, K., Sylvester, P., Vermeesch, P., and others (2016) Community-Derived Standards for LA-ICP-MS U-(Th-)Pb Geochronology - Uncertainty Propagation, Age Interpretation and Data Reporting. Geostandards and Geoanalytical Research, 40, 311–332.

Humphreys, M.C.S., Edmonds, M., and Klöcking, M.S. (2016) The validity of plagioclase-melt geothermometry for degassing-driven magma crystallization. American Mineralogist, 101, 769–779.

Iacovino, K., Kim, J.S., Sisson, T.W., Lowenstern, J.B., Jang, J.N., Song, K.H., Ham, H.H., Ri, K.H., Donovan, A.R., Oppenheimer, C., and others (2015) New Constraints on the Geochemistry of the Millennium Eruption of Mount Paektu (Changbaishan), Democratic People's Republic of Korea/China. In 2015 AGU Fall Meeting. San Francisco, CA, USA.

Loewen, M.W., and Bindeman, I.N. (2015) Oxygen isotope and trace element evidence for three-stage petrogenesis of the youngest episode (260–79 ka) of Yellowstone rhyolitic volcanism. Contributions to Mineralogy and Petrology, 170.

Lynn, K.J., Garcia, M.O., Shea, T., Costa, F., and Swanson, D.A. (2017) Timescales of mixing and storage for Keanakāko'i Tephra magmas (1500–1820 C.E.), Kīlauea Volcano, Hawai'i. Contributions to Mineralogy and Petrology, 172.

Mahood, G., and Hildreth, W. (1983) Large partition coefficients for trace elements in high-silica rhyolites. Geochimica et Cosmochimica Acta, 47, 11–30.

Martin, V.M., Morgan, D.J., Jerram, D.A., Caddick, M.J., Prior, D.J., and Davidson, J.P. (2008) Bang! Month-Scale Eruption Triggering at Santorini Volcano. Science, 321, 1178–1178.

Matthews, N.E., Vazquez, J.A., and Calvert, A.T. (2015) Age of the Lava Creek supereruption and magma chamber assembly from combined $^{40}Ar/^{39}Ar$ and U-Pb dating of sanidine and zircon crystals. Geochemistry, Geophysics, Geosystems, 16, 2508–2528.

Milman-Barris, M.S., Beckett, J.R., Baker, M.B., Hofmann, A.E., Morgan, Z., Crowley, M.R., Vielzeuf, D., and Stolper, E. (2008) Zoning of phosphorus in igneous olivine. Contributions to Mineralogy and Petrology, 155, 739–765.

Mollo, S., Del Gaudio, P., Ventura, G., Iezzi, G., and Scarlato, P. (2010) Dependence of clinopyroxene composition on cooling rate in basaltic magmas: Implications for thermobarometry. Lithos, 118, 302–312.

Morgado, E., Morgan, D.J., Castruccio, A., Ebmeier, S.K., Parada, M.-Á., Brahm, R., Harvey, J., Gutiérrez, F., and Walshaw, R. (2019) Old magma and a new, intrusive trigger: using diffusion chronometry to understand the rapid-onset Calbuco eruption, April 2015 (Southern Chile). Contributions to Mineralogy and Petrology, 174.

Morgan, D.J., and Blake, S. (2006) Magmatic residence times of zoned phenocrysts: introduction and application of the binary element diffusion modelling (BEDM) technique. Contributions to Mineralogy and Petrology, 151, 58–70.

Morgan, D.J., Blake, S., Rogers, N.W., DeVivo, B., Rolandi, G., Macdonald, R., and Hawkesworth, C.J. (2004) Time scales of crystal residence and magma chamber volume from modelling of diffusion profiles in phenocrysts: Vesuvius 1944. Earth and Planetary Science Letters, 222, 933–946.

Morgan, D.J., Blake, S., Rogers, N.W., De Vivo, B., Rolandi, G., and Davidson, J.P. (2006) Magma chamber recharge at Vesuvius in the century prior to the eruption of AD 79. Geology, 34, 845–848.

Müller, T., Dohmen, R., Becker, H.W., ter Heege, J.H., and Chakraborty, S. (2013) Fe–Mg interdiffusion rates in clinopyroxene: experimental data and implications for Fe–Mg exchange geothermometers. Contributions to Mineralogy and Petrology, 166, 1563–1576.

Mutch, E.J.F., Maclennan, J., Shorttle, O., Edmonds, M., and Rudge, J.F. (2019) Rapid transcrustal magma movement under Iceland. Nature Geoscience.

Myers, M.L., Wallace, P.J., Wilson, C.J.N., Morter, B.K., and Swallow, E.J. (2016) Prolonged ascent and episodic venting of discrete magma batches at the onset of the Huckleberry Ridge supereruption, Yellowstone. Earth and Planetary Science Letters, 451, 285–297.

Orlando, A., D'Orazio, M., Armienti, P., and Borrini, D. (2008) Experimental determination of plagioclase and clinopyroxene crystal growth rates in an anhydrous trachybasalt from Mt Etna (Italy). European Journal of Mineralogy, 20, 653–664.

Pamukcu, A.S., Ghiorso, M.S., and Gualda, G.A.R. (2016) High-Ti, bright-CL rims in volcanic quartz: a result of very rapid growth. Contributions to Mineralogy and Petrology, 171.

Pistone, M., Blundy, J., and Brooker, R.A. (2017) Water transfer during magma mixing events: Insights into crystal mush rejuvenation and melt extraction processes. American Mineralogist, 102, 766–776.

Pritchard, C.J., and Larson, P.B. (2012) Genesis of the post-caldera eastern Upper Basin Member rhyolites, Yellowstone, WY: from volcanic stratigraphy, geochemistry, and radiogenic isotope modeling. Contributions to Mineralogy and Petrology, 164, 205–228.

Reid, M.R., and Vazquez, J.A. (2017) Fitful and protracted magma assembly leading to a giant eruption, Youngest Toba Tuff, Indonesia. Geochemistry, Geophysics, Geosystems, 18, 156–177.

Rivera, T.A., Schmitz, M.D., Crowley, J.L., and Storey, M. (2014) Rapid magma evolution constrained by zircon petrochronology and $^{40}Ar/^{39}Ar$ sanidine ages for the Huckleberry Ridge Tuff, Yellowstone, USA. Geology, 42, 643–646.

Rivera, T.A., Schmitz, M.D., Jicha, B.R., and Crowley, J.L. (2016) Zircon Petrochronology and $^{40}Ar/^{39}Ar$ Sanidine Dates for the Mesa Falls Tuff: Crystal-scale Records of Magmatic Evolution and the Short Lifespan of a Large Yellowstone Magma Chamber. Journal of Petrology, 57, 1677–1704.

Rubin, A., Cooper, K.M., Leever, M., Wimpenny, J., Deering, C., Rooney, T., Gravley, D., and Yin, Q. (2016) Changes in magma storage conditions following caldera collapse at Okataina Volcanic Center, New Zealand. Contributions to Mineralogy and Petrology, 171.

Rubin, A., Cooper, K.M., Till, C.B., Kent, A.J.R., Costa, F., Gravley, D., Deering, C., and Cole, J. (2017) Rapid cooling and cold storage in a silicic magma reservoir recorded in individual crystals. Science, 356.

Salviulo, G., Secco, L., Marzoli, A., Piccirillo, E.M., and Nyobe, J.B. (2000) Ca-rich pyroxene from basic and silicic volcanic rocks from the Cameroon Volcanic Line (West-Africa): crystal chemistry and petrological relationships. Mineralogy and Petrology, 70, 73–88.

Sambridge, M. (1999) Geophysical inversion with a neighbourhood algorithm - II. Appraising the ensemble. Geophysical Journal International, 138, 727–746.

Saunders, K., Blundy, J., Dohmen, R., and Cashman, K. (2012) Linking Petrology and Seismology at an Active Volcano. Science, 336, 1023–1027.

Shamloo, H.I., and Till, C.B. (2019) Decadal transition from quiescence to supereruption: petrologic investigation of the Lava Creek Tuff, Yellowstone Caldera, WY. Contributions to Mineralogy and Petrology, 174.

Shea, T., Lynn, K.J., and Garcia, M.O. (2015) Cracking the olivine zoning code: Distinguishing between crystal growth and diffusion. Geology, 43, 935–938.

Simakin, A.G., and Bindeman, I.N. (2012) Remelting in caldera and rift environments and the genesis of hot, "recycled" rhyolites. Earth and Planetary Science Letters, 337–338, 224–235.

Singer, B.S., Costa, F., Herrin, J.S., Hildreth, W., and Fierstein, J. (2016) The timing of compositionally-zoned magma reservoirs and mafic 'priming' weeks before the 1912 Novarupta-Katmai rhyolite eruption. Earth and Planetary Science Letters, 451, 125–137.

Sisson, T.W. (1991) Pyroxene-high silica rhyolite trace element partition coefficients measured by ion microprobe. Geochimica et Cosmochimica Acta, 55, 1575–1585.

Stelten, M.E., Cooper, K.M., Vazquez, J.A., Calvert, A.T., and Glessner, J.J.G. (2015) Mechanisms and Timescales of Generating Eruptible Rhyolitic Magmas at Yellowstone Caldera from Zircon and Sanidine Geochronology and Geochemistry. Journal of Petrology, 56, 1607–1642.

Stelten, M.E., Cooper, K.M., Wimpenny, J.B., Vazquez, J.A., and Yin, Q.-Z. (2017) The role of mantle-derived magmas in the isotopic evolution of Yellowstone's magmatic system. Geochemistry, Geophysics, Geosystems, 18, 1350–1365.

Stelten, M.E., Champion, D.E., and Kuntz, M.A. (2018) The timing and origin of pre- and post-caldera volcanism associated with the Mesa Falls Tuff, Yellowstone Plateau volcanic field. Journal of Volcanology and Geothermal Research, 350, 47–60.

Stock, M.J., Humphreys, M.C.S., Smith, V.C., Isaia, R., and Pyle, D.M. (2016) Late-stage volatile saturation as a potential trigger for explosive volcanic eruptions. Nature Geoscience, 9, 249–254.

Sundermeyer, C., Di Muro, A., Gordeychik, B., and Wörner, G. (2020) Timescales of magmatic processes during the eruptive cycle 2014–2015 at Piton de la Fournaise, La Réunion, obtained from Mg–Fe diffusion modelling in olivine. Contributions to Mineralogy and Petrology, 175.

Swanson, S.E. (1977) Relation of nucleation and crystal-growth rate to the development of granitic textures. American Mineralogist, 62, 966–978.

Till, C.B. (2017) An Integrated Approach for Identifying P-T-X-t Histories and Eruption Triggers for Silicic Magmas; An Example Examining the Scaup Lake Rhyolite Yellowstone Caldera, WY. In 2017 Scientific Assembly. Presented at the IAVCEI, Portland, OR.

Till, C.B., Vazquez, J.A., and Boyce, J.W. (2015) Months between rejuvenation and volcanic eruption at Yellowstone caldera, Wyoming. Geology, 43, 695–698.

Till, C.B., Vazquez, J.A., Stelten, M.E., Shamloo, H.I., and Shaffer, J.S. (2019) Coexisting Discrete Bodies of Rhyolite and Punctuated Volcanism Characterize Yellowstone's Post☐Lava Creek Tuff Caldera Evolution. Geochemistry, Geophysics, Geosystems, 20, 3861–3881.

Van Orman, J.A., Grove, T.L., and Shimizu, N. (2001) Rare earth element diffusion in diopside: influence of temperature, pressure, and ionic radius, and an elastic model for diffusion in silicates. Contributions to Mineralogy and Petrology, 141, 687–703.

Vazquez, J.A., Kyriazis, S.F., Reid, M.R., Sehler, R.C., and Ramos, F.C. (2009) Thermochemical evolution of young rhyolites at Yellowstone: Evidence for a cooling but periodically replenished post-caldera magma reservoir. Journal of Volcanology and Geothermal Research, 188, 186–196.

Watts, K.E., Bindeman, I.N., and Schmitt, A.K. (2012) Crystal scale anatomy of a dying supervolcano: an isotope and geochronology study of individual phenocrysts from voluminous rhyolites of the Yellowstone caldera. Contributions to Mineralogy and Petrology, 164, 45–67.

Wen, S., and Nekvasil, H. (1994) SOLVALC: An interactive graphics program package for calculating the ternary feldspar solvus and for two-feldspar geothermometry. Computers & Geosciences, 20, 1025–1040.

Wotzlaw, J.-F., Bindeman, I.N., Stern, R.A., D'Abzac, F.-X., and Schaltegger, U. (2015) Rapid heterogeneous assembly of multiple magma reservoirs prior to Yellowstone supereruptions. Scientific Reports, 5, 14026.

Zhang, Y. (2008) Geochemical Kinetics, 631 p. Princeton University Press, Princeton, New Jersey.

Chapter 4

EXPERIMENTAL DETERMINATION OF ROCKY EXOPLANET MANTLE SOLIDI AND MELT COMPOSITIONS

Abstract

Interest in exoplanet studies has intensified over the last two decades with the discovery of ~ 4000 exoplanets. Investigation of these planets from outside our solar system primarily utilizes tools from the fields of astronomy and geophysics, however the key questions driving the field of exoplanet research require an understanding of their surface chemistries: what is the composition of the surface? What minerals and rock types are available for surface geochemical reactions that could potentially support life? Answering these questions, as well as understanding the volcanic contribution to any atmosphere present, necessitates applying methods from the field of igneous petrology.

Here we present the results of petrological experiments to determine the melt compositions, melting reactions, and exoplanet mantle mineral modes for two hypothetical rocky exoplanets, as well as estimate the volatile solubilities of these magmas. We compare experimental melt compositions to rocky planet melts from our solar system and discuss implications for decompression melting and magma oceans. Our data can be used to calibrate future exoplanet petrologic models and to predict differences in crust compositions of exoplanets with similar bulk compositions to those explored herein. NASA's James Webb Space Telescope and ESA's Atmospheric Remote-sensing Infrared Exoplanet Large-survey will soon enable the spectroscopic characterization of exoplanet atmospheres. It may be possible to make inferences about the bulk silicate exoplanets capable of exhibiting certain atmospheric compositions, and so this empirical study represents an early step in our effort to prepare to interpret these future observations.

4.1 Introduction

Since the confirmation of the first exoplanet in 1992 (Wolszczan and Frail 1992), our biggest questions about exoplanets have to do with their ability to support life. Over 4000 exoplanets have been identified in the last 30 years, with active missions such as NASA's Transiting Exoplanet Survey Satellite (TESS) and the University of Liège's Transiting Planets and Planetesimals Small Telescope (TRAPPIST) aiming to double this number in the next few years. Investigations of exoplanets have primarily utilized methods from the fields of astronomy and geophysics; what we know about exoplanets is overwhelmingly limited to parameters that can be calculated from astronomical observations (e.g., mass and radius). These data have allowed for the classification of exoplanets by their size and stellar irradiance (e.g., Fulton et al. 2017; Weiss et al. 2018), but have a limited ability to produce models of exoplanet atmospheres and interior structure (e.g., Hu et al. 2012; Dorn et al. 2018; Schwieterman et al. 2018; Unterborn and Panero 2019).
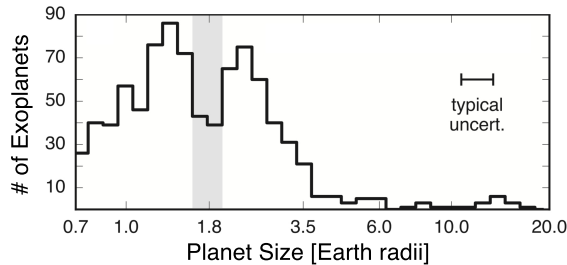
Figure 4.1: Histogram of number of exoplanets binned by their size in Earth radii. The gray bar highlights the gap in planet distribution around 1.8 Earth radii. Kepler exoplanet candidates were edited to this population of 900 exoplanets based on completeness of observational data as well as host star parameters that yield the most reliable data for the exoplanet and its host star. After Fulton et al. (2017), Figure 2g.

However, as we endeavor to answer questions about exoplanets' compositions, interior structures, and near surface conditions with regards to their suitability for life, incorporating knowledge from a broad array of Earth and planetary science disciplines becomes critical. Most exoplanets from the California-*Kepler* Survey (CKS), a collection of stellar and planetary data for *Kepler* candidate exoplanets (Johnson et al. 2017; Petigura et al. 2017), are less than 4 Earth radii ($R_\oplus$) in size with a gap

in the distribution at $\sim$1.5–2 R$_\oplus$, regardless of the size of the host star (Fig. 4.1.) (Owen and Wu 2013; Fulton et al. 2017; Martinez et al. 2019). This gap separates small exoplanets into two populations: those more likely to have thick gas envelopes and those more likely to be rocky planets with thin atmospheres. The latter are similar to Earth and so are sometimes referred to as "super-Earths" (Fig. 4.1.) (Fulton et al. 2017; Martinez et al. 2019). Super-Earths are attractive targets for study not only because of their potential to orbit in their stars' habitable zone (HZ; the orbital region where liquid water is possible on a planetary surface) (Kasting et al. 1993; Kopparapu et al. 2014; Kane et al. 2016) but because of their abundance (Fulton et al. 2017; Johnson et al. 2017). For the $\sim$50% of exoplanets likely to be rocky, knowledge of geologic characteristics such as composition and mineralogy, surface recycling mechanisms (e.g., plate tectonics versus stagnant lid), and volcanic behavior are key to addressing the aforementioned questions.

Experimental petrology has been used to study other planets and moons in our solar system and have led to insights such as redox conditions, degree of differentiation, melt compositions, location of solidi, magma sources, and planetary cooling rates for these bodies (e.g., Wadhwa 2008; Grove and Krawczynski 2009; Krawczynski and Grove 2012; Filiberto 2014; Kiefer et al. 2015, 2015; Namur et al. 2016; Putirka 2016; Vander Kaaden et al. 2017 and references therein). Only recently have workers begun to apply concepts from traditional mineralogy and petrology to exoplanets (e.g., Nisr et al. 2017; Hakim et al. 2019), and the field of igneous petrology is particularly relevant, as it provides constraints on the conditions necessary for melting rocky planetary interiors, mechanisms to understand controls on resulting magma compositions and volatile cargoes, and their relationship to subsequent planetary crusts.

An understanding of these petrological parameters is crucial in the creation of models that can be applied to planets that do not orbit stars of a similar composition to our own. Planetary formation models interpret solar nebulae to comprise essentially all of the elemental building blocks for the resulting star and its orbiting bodies, as established by the correlation between the compositions of condensed planetary material (i.e., carbonaceous chondrites) and the solar photosphere (Feldman 1992). Thus, planetary compositions (the rocky portion of which are mostly composed of refractory elements) can be directly related to the composition of the host star (Hinkel and Unterborn 2018). However, ex-

isting geochemical models for melt formation and mineral equilibria do not work well with planetary compositions that deviate from those of our inner solar system (see "Discussion"), which is not surprising as they rely on the mineralogy and relationships characteristic of Earth's interior, a geochemical scope we suspect is quite narrow as compared to the profusion of known stellar compositions (Fig. 4.2) (Hinkel et al. 2014; Unterborn and Panero 2019).
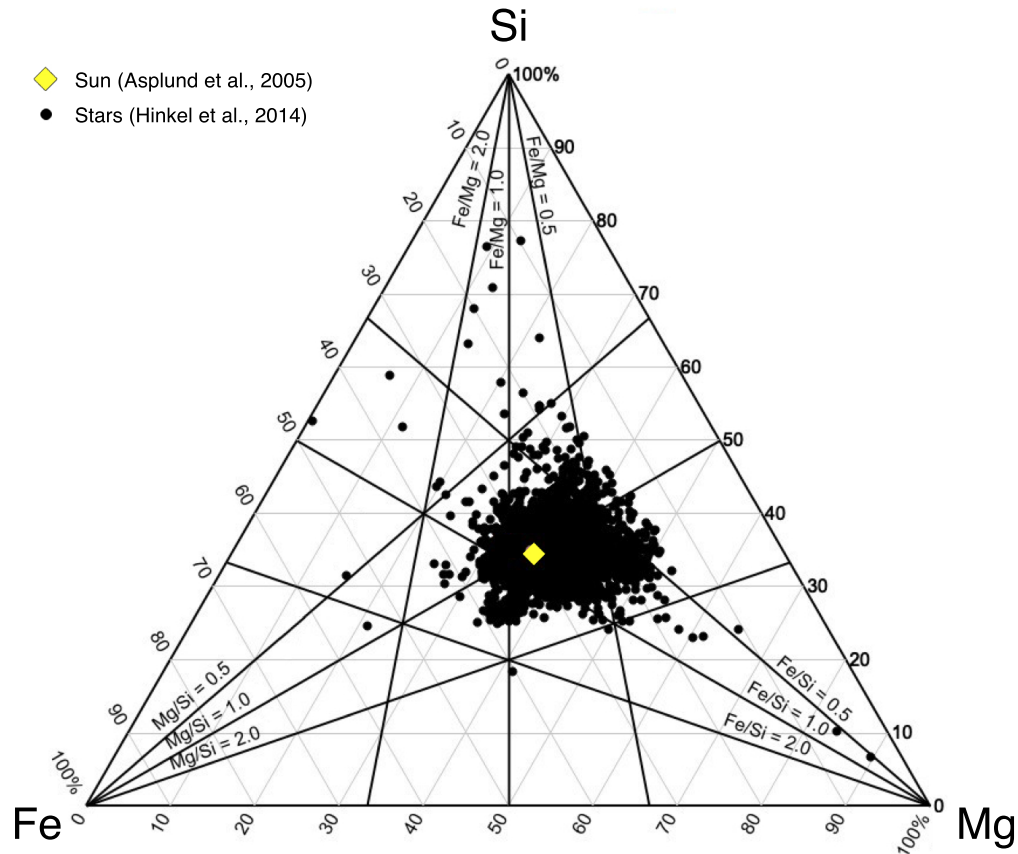
Figure 4.2: Ternary diagram of molar abundances of Fe, Si, and Mg for stars in our galaxy. Solid black lines show lines of equal molar ratio. After Unterborn and Panero (2019), Figure 1.

Here we use established techniques from the field of experimental petrology to produce the empirical data needed to begin to close this knowledge gap and ultimately build better geochemical models for application to exoplanetary systems. We present the experimentally determined solidi, mineral modes, melting reactions, and compositions of partial mantle melts for two hypothetical super-Earth-

type exoplanets. Our new data may be used to calibrate future models for extrasolar planets, as understanding the composition of exoplanet partial mantle melts is crucial to understanding element cycling from subsurface to surface, weathering on the exoplanet's surface, and the outgassing that contributes to secondary atmospheres.

4.2   Methods

4.2.1   Starting Compositions

A first order proxy to exoplanet solid rock (bulk) compositional data is the composition of the host star (Young et al. 2014; Hinkel and Unterborn 2018). Stellar compositions may vary significantly relative to our star, particularly in Mg, Fe, Al, Ca, and Si, elements critical in rock-forming minerals (Hinkel et al. 2014). The molar abundances of three of these elements, Fe, Si, and Mg, are plotted on Figure 4.2. As evident here, our star has an Mg/Si molar ratio of 1.06 while the known stars in our galaxy cover a broad range of 0.7–1.6. Thus, we concentrated our geological experiments near these Mg/Si extrema in order to constrain a range of possible exoplanets.

Table 4.1: Experiment starting compositions [wt%]

Oxide	HEX1	HEX2
SiO_2	40	49.21
TiO_2	0.18	0
Al_2O_3	4.06	3.1
Cr_2O_3	0.47	0
FeO^{tot}	7.55	7.69
MnO	0.13	0
MgO	44	35.43
CaO	3.21	4.15
Na_2O	0.33	0.41
K_2O	0.03	0
P2O5	0.02	0
NiO	0.28	0
Mg#	91	89

Two non-Earth silicate exoplanet compositions were selected for partial melting experiments based on areas of Figure 4.2 that represent under-investigated compositional space. These experimental starting compositions are not intended to directly simulate specific exoplanets, but rather to establish experimental calibration points for rocky exoplanets that are significantly outside the compositional space of our solar system and are likely to be relevant for exoplanetary systems.

The first hypothetical exoplanet starting composition (HEX1) was created by adjusting the bulk silicate Earth (BSE) composition to produce a molar Mg/Si ratio of 1.42, as an end member of those exoplanet compositions with Mg/Si ratios greater than BSE (Mg/Si = 1.06) (Table 4.1) (Hart and Zindler 1986). The second hypothetical exoplanet starting composition (HEX2) was created to have Mg/Si similar to that of Earth (0.93), but a higher molar Ca/Al ratio (1.81 vs. 1.07) similar to a region of composition space where clinopyroxene and other Ca-bearing phases may be more prevalent (Table 4.1) (Hart and Zindler 1986).

4.2.2 Experimental Procedure

All preparation and experiments were conducted at the Experimental Petrology and Igneous processes Center (EPIC) at Arizona State University (ASU). Starting mixes were produced from high purity oxide powders and were ground in an agate mortar for two hours under ethanol. All Fe was added as Fe_2O_3 powder. The mixes, which included Na as Na_2CO_3 and K as as K_2CO_3 were then decarbonated in a box furnace at 850°C. Approximately 0.03 g of starting mix was pressed into $Au_{80}Pd_{20}$ capsules that were then triple-crimped and welded using a PUK TIG welder with a tungsten electrode under Ar gas. Capsules were reweighed to check for mass loss or gain that may have occurred during welding, then checked for leakage by soaking in acetone for 10+ minutes before weighing a third time. All experiments were nominally anhydrous.

Experiments were conducted in an end-loaded solid-medium piston-cylinder apparatus from Rockland Research (Boyd and England 1960) with automated pressure and temperature control following the assembly arrangement and the heating and pressurization procedure of Médard and Grove

Table 4.2: Piston-cylinder experimental conditions and run products

Expt.	P [kbar]	T [°C]	t [hrs]	Phases				
				ol	opx	cpx	sp	melt
HEX1								
R61	10	1100	24	73	6	13	8	x
R57	10	1200	24	72	6	14	8	x
R85	10	1250	24	67	12	8	3	10
R89	10	1250	24	64	13	7	4	12
R80	10	1300	24	75	1	x	4	20
R74	10	1350	24	75	x	x	5	20
R99	10	1375	24	78	x	x	5	17
R34	20	1200	24	68	8	14	9	x
R44	20	1300	24	69	6	16	9	x
R77	20	1350	24	70	4	17	9	x
R79	20	1400	24	72	2	2	3	21
R39*	20	1450	24	78	x	x	4	18
HEX2								
R108	10	1100	72	21	55	17	6	x
R105	10	1150	24	20	58	16	6	x
R112	10	1300	24	22	60	13	4	x
R125	10	1325	24	34	39	x	x	26
R122	10	1350	24	43	28	x	x	28
R110	15	1100	24	18	61	18	5	x
R95	15	1150	24	20	57	17	6	x
R78	15	1200	24	18	61	16	4	x
R114	15	1250	24	23	56	17	4	x
R129	15	1350	24	29	47	x	1	23
R117	15	1400	24	43	32	x	x	24
R107	20	1100	24	20	55	19	7	x
R109	20	1150	24	18	58	18	5	x
R127	20	1250	24	23	55	18	4	x
R115	20	1400	24	34	47	x	1	18

*R39 experienced 25% Fe loss and therefore was used only to constrain the solidus; liq = liquid (glass), ol = olivine, opx = orthopyroxene, cpx = clinopyroxene, sp = spinel

(2006). To summarize, the $\frac{1}{2}$" experimental assembly consisted of a Pb-foil-wrapped sintered BaCO3 pressure sleeve, MgO spacers and thermocouple shield, an alumina ring and thermocouple sheath, and a graphite furnace and base. The $BaCO_3$ pressure medium was found to have no pressure correction through calibration against the albite = jadeite + quartz and Ca-tschermak pyroxene = anorthite + gehlenite + corundum reactions (Hays 1966; Longhi 2005). Pressures are thought to be accurate to $\pm$0.05 GPa. Temperature was controlled with a Eurotherm 2404 to $\pm$20°C and monitored using a Type D W3%Re/W25%Re thermocouple which is thought to be accurate to $\pm$10°C (Médard and Grove 2006). A temperature correction of 18–39°C was calculated for each experiment depending on the geometry of the capsule and assembly, ensuring the capsule was positioned in the hotspot of the furnace. This correction was determined by spinel growth temperature calibration experiments conducted after Watson et al. (2002).

Experiments were pressurized to 10 kbar at room temperature then heated at $\sim$100°C/min. to 865°C. If the target pressure was above 10 kbar, pressure was increased to the final experimental pressure during a 6-minute dwell time. The piston-cylinder was then heated to the final experimental temperature. We conducted piston-cylinder experiments over 10–20 kbar and 1100–1450°C with run durations of 24–72 hours (Table 4.2). To mitigate the nucleation of crystals upon quenching, experiments were "pressure quenched" by simultaneously turning off heat and releasing pressure on the piston (e.g., Putirka et al. 1996; Krawczynski and Grove 2012).

4.2.3   Analytical Procedure

The experimental charges were prepared for analysis by cutting each capsule in half longitudinally with a low-speed saw and vacuum-impregnating one half of the capsule in epoxy. Mounts were polished using diamond suspension pastes, carbon coated, and then analyzed using energy-dispersive X-ray spectroscopy (EDS) and wavelength-dispersive X-ray spectroscopy (WDS) on the JXA-8530F EPMA at ASU's Eyring Materials Center using an accelerating voltage of 15 kV and beam current of 15 nA. Beam sizes were 1 micron for minerals and 1–3 microns for HEX1 melt and 5–10 microns for HEX2 melt. Time-dependent intensity (TDI) corrections were applied to melt analyses to mitigate mi-

gration of light elements away from the electron beam, however usually this correction did not have a statistically significant effect on the measurements.

4.3   Results

Mineral phases from accepted experiments are compositionally homogenous throughout each charge, are free of zoning or reaction rims, and have Mg#s and Fe-Mg partition coefficients consistent with values for Earth as is expected for experiments that produce a similar mineral assemblage. Experiments were considered unsuccessful if they did not pass the criteria described above or failed to maintain mass balance, and were therefore excluded from the results and discussion below.

Table 4.3: Average experimental melt compositions [wt%]

Oxide	HEX1	s.d.	HEX2	s.d.
$SiO2$	47.8	2.20	51.6	1.8
TiO_2	0.84	0.16		
Al_2O_3	15.3	1.9	8.08	0.62
Cr_2O_3	0.13	0.09		
FeO^{tot}	10.5	1.8	14.8	1.47
MnO	0.18	0.02		
MgO	10.8	5.0	11.3	4.07
CaO	13.8	1.3	13.7	1.92
Na_2O	0.66	0.14	0.72	0.08
K_2O	0.15	0.06		
Mg#	61.5	11.8	54.2	0.17
n =	109		103	

EPMA

Experimental phase assemblages represent the mineralogy of these hypothetical exoplanets' mantles (Table 4.2). Experiments for both HEX1 and HEX2 crystallized only olivine (ol), clinopyroxene (cpx), orthopyroxene (opx), and spinel (sp), with all four minerals present in all experiments $\leqslant 1275^\circ$C (Fig. 4.3). For HEX1 the most abundant mineral is olivine; for HEX2 the dominant mineral is opx (Table 4.2).
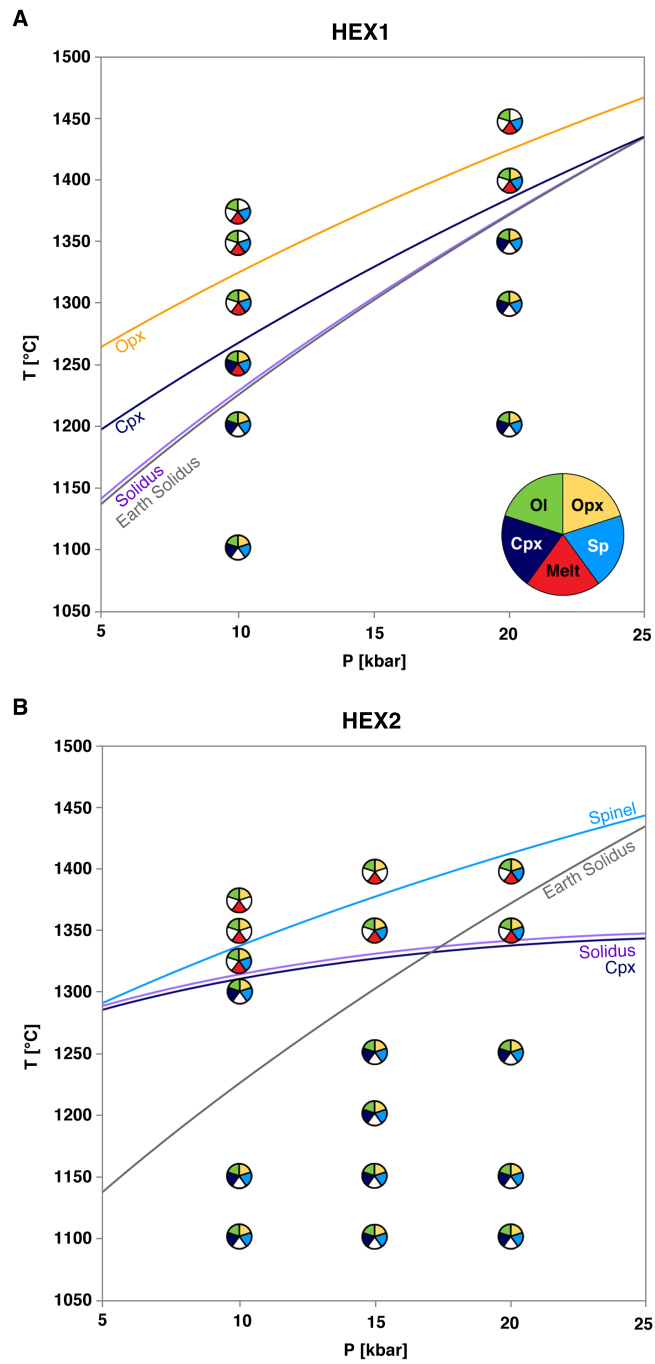
Figure 4.3: Phase diagrams for A: HEX1 and B: HEX2. Wedges are filled if that phase was present. Earth's dry mantle solidus is plotted in gray for reference.

For HEX1 experimental charges, olivine are subhedral to anhedral (2–80 microns), opx are sub-hedral to anhedral (1–40 microns), cpx are euhedral to anhedral (< 1–20 microns), and spinel are euhedral to anhedral (< 1–10 microns). Crystals tend to be equant. Opx are sometimes present as needle-like laths that protrude into cpx. Charges run at temperatures < 1300°C have a generally finer-grained texture composed of similarly sized crystals distributed homogenously throughout the charge, although cpx tends to clump together in ribbons. For experiments run $\geqslant$ 1300°C, crystals sizes are bimodal and when present, cpx and melt tend to be located at the hot end (top) of the charge.

In HEX2 run products, olivine are euhedral to subhedral (10–80 microns), opx are subhedral to anhedral (10–50 microns), cpx are subhedral to anhedral (1–50 microns), and spinel are euhedral to anhedral (< 1–20 microns, rarely 40–90 microns). The majority of the crystals are equant with rare larger phases being tabular. Opx are sometimes present as equant or tabular chadacrysts inside cpx at lower P-T conditions, or in olivine at higher P-T conditions. Experimental products $\leqslant$ 1300°C have a generally finer-grained texture composed of similarly sized crystals distributed homogenously throughout the charge. Experiments run > 1300°C have a wider variety of crystal sizes and when present, spinel and melt are usually preferentially located at the hot end (top) of the charge. For HEX1, the location of the dry solidus did not change relative to Earth's dry peridotite solidus (Fig. 4.3 A). However, for HEX2, we found a change in the location of the solidus as well as a shallowing in the slope from $\sim$15°C/kbar for Earth to $\sim$3°C/kbar (Fig. 4.3 B).

By examining the abundance of each mineral phase and melt, we can construct melting reactions to describe how the exoplanet mantle mineralogy changes as melt is extracted. They are as follows, normalized to 1 unit mass of melt:

HEX1 (high Mg/Si)

      10 kbar: 0.72 cpx + 0.42 opx + 0.14 sp $\Rightarrow$ 0.28 ol + 1.0 melt

      20 kbar: 0.91 cpx + 0.24 opx + 0.30 sp $\Rightarrow$ 0.36 ol + 1.0 melt

HEX2 (high Ca/Al)

      10 kbar: 0.48 cpx + 1.1 opx + 0.14 sp $\Rightarrow$ 0.77 ol + 1.0 melt

15 kbar: 0.67 cpx + 0.83 opx + 0.17 sp ⟹ 0.67 ol + 1.0 melt

20 kbar: 1.0 cpx + 0.42 opx + 0.17 sp ⟹ 0.58 ol + 1.0 melt
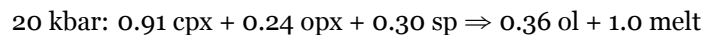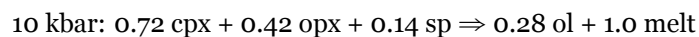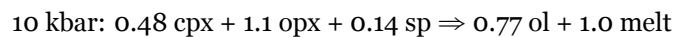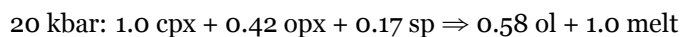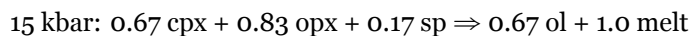
For comparison, a melting reaction for Earth (Kinzler and Grove 1992) is:

9 kbar: 0.31 cpx + 0.16 opx + 0.58 sp ⟹ 0.06 ol + 1.0 melt
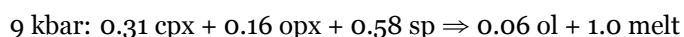
4.4   Discussion

4.4.1   Melting Reactions, Melt Compositions, and Exoplanet Mantle Solidi

The melting reactions for Earth and our hypothetical exoplanets are superficially similar—they each involve the same minerals, and for lower pressures (i.e., < 13 kbar) Earth reactions (Kinzler and Grove 1992) have the same products and reactants as HEX1 and HEX2 (see "Results"). However, the rates of these reactions are not identical, nor are the compositions of the mantles or mantle-derived melts. Mantle partial melts produced by HEX1 and HEX2 were basaltic with similar SiO_2, MgO, and FeO content as Earth and rocky solar system planet melts: 44–50 wt% SiO_2 for HEX1 and 49–54 wt% SiO_2 for HEX 2, and Mg# 50–78 for HEX1 and Mg# 45–61 for HEX2 (Table 4.4, Fig. 4.4 A).

Table 4.4: Average mantle modes

	Olivine	Cpx	Opx	Spinel
Earth*	60%	15%	15%	10%
HEX1	71%	15%	6%	8%
HEX2	22%	16%	58%	4%

*From PUM of Hart & Zindler (1986)

However, the exoplanet melts are enriched in CaO (10–15 wt%, Table 4.4) compared to a CaO content of < 15 wt% for Earth melts and < 12 wt% for other solar system melts (Squyres et al. 2007; Treiman 2007; Gale et al. 2013; Santos et al. 2015; Vander Kaaden et al. 2017, and PetDB) (Fig. 4.4
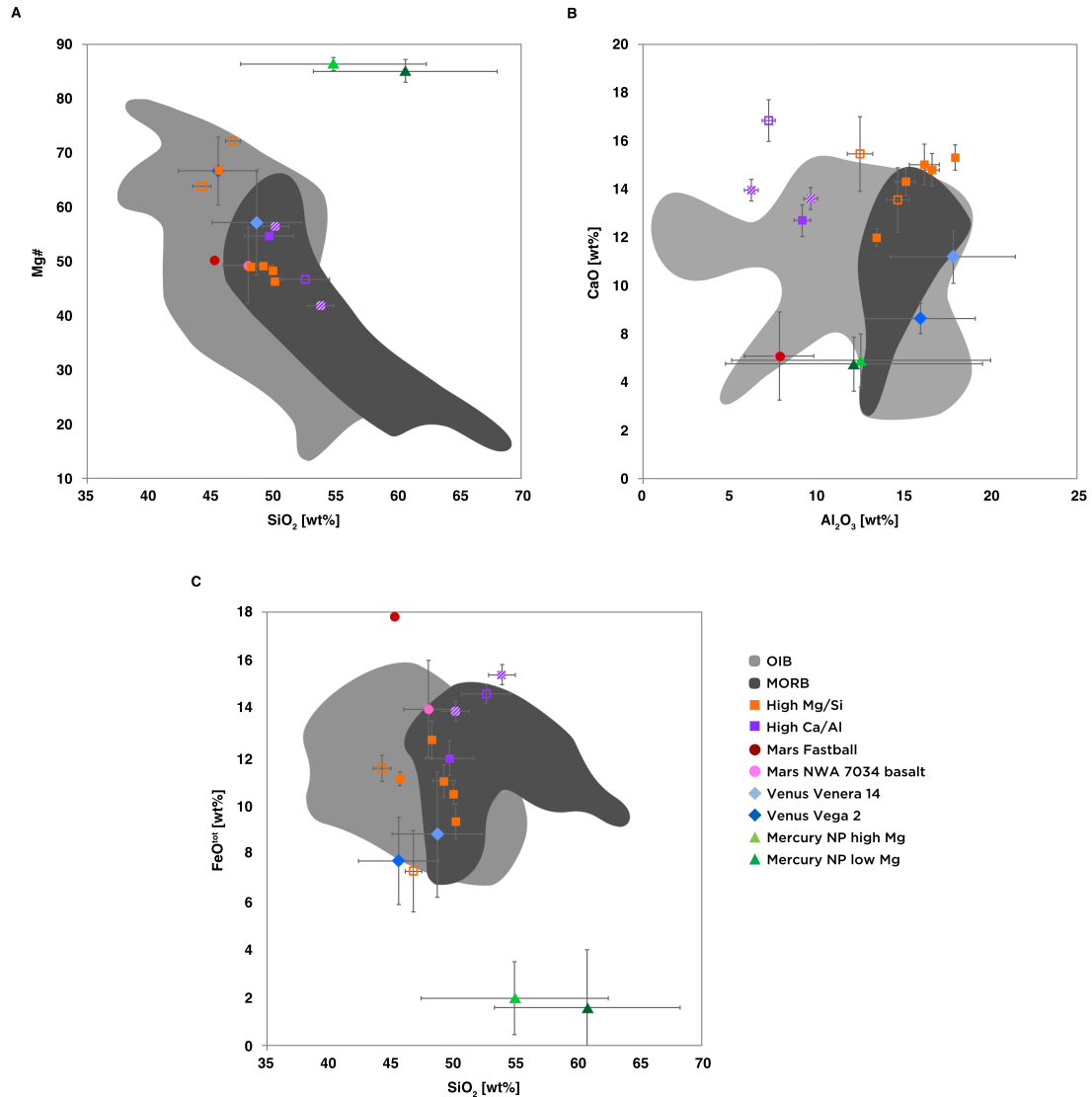
Figure 4.4: Composition of experimental exoplanet melts, as well as Earth and rocky solar system planet melts. A: Mg# vs. SiO_2, B: CaO vs Al_2O_3, and C: FeO^{tot} vs SiO_2. For this study, open symbols are 20 kbar experiments. Diagonal-barred symbols are 15 kbar experiments. Filled symbols are 10 kbar experiments. Bars indicate 1 sigma error; some are smaller than the symbols. Data from Squyres et al. (2007); Treiman (2007); Gale et al. (2013); Santos et al. (2015); Vander Kaaden et al. (2017).

B). Compared to the mantle mineralogy of a non-depleted bulk Earth mantle composition (Hart and Zindler 1986), HEX1 yields the same amount or less of the Ca-bearing phases: clinopyroxene (15% for both) and orthopyroxene (6% for HEX1 versus 15% for Earth), and about the same amount of spinel (8% versus 10% for Earth) (Table 4.3). However, HEX1's mantle is composed of ∼10% more olivine

than Earth's primitive upper mantle (Table 4.3). When a eutectic melt composition for HEX1 (experiment R85: 10 kbar 1250°C) is plotted on an olivine-cpx-quartz pseudoternary (Fig. 4.5), the mantle multiple saturation point (MSP)—where the melt is in equilibrium with all the mantle minerals—is shifted away from the olivine vertex as compared to the predicted 10 kbar MSP for a dry Earth mid-ocean ridge basalt (MORB), demarcating the expansion of the olivine primary phase field for HEX1. As the HEX1 mantle is principally composed of olivine and this mineral does not incorporate Ca, the result is melt that contains 11–15 wt% CaO, which is at the extrema of Earth dry melts and higher than other solar system melts (Fig. 4.4 B).
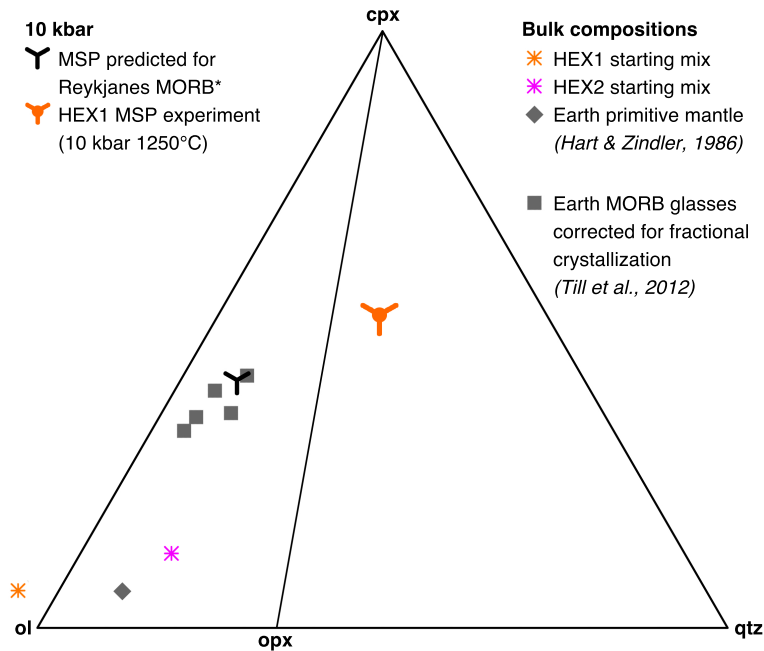
Figure 4.5: Pseudoternary of experimental starting mix compositions, Earth bulk primitive mantle (Hart and Zindler 1986), Earth MORB glasses that have been corrected for fractional crystallization (Till et al. 2012), and multiple saturation points (MSP) predicted using Reykjanes MORB glass at 10 kbar. Also plotted is the actual multiple saturation point for HEX1 (HEX2 did not yield any multiply saturated experimental products). *Calculated using equations from Till et al. (2012), Table 5.

HEX2 also exhibits a high CaO content (12–16.5 wt%). This starting composition yields $\sim$3.5x more orthopyroxene than clinopyroxene (Table 4.3); given the stoichiometry of orthopyroxene $((Fe,Mg)SiO_3)$, it is stabilized at the expense of clinopyroxene $(Ca(Fe, Mg)Si_2O_6)$ and so there is addi-

tional CaO partitioned into the melt. HEX2's low bulk Al_2O_3 content (3.10 wt%, Table 4.1) relative to the non-depleted bulk Earth mantle (4.06 wt%, Hart and Zindler 1986), as well as the abundance of Fe-bearing orthopyroxene results in a lower phase proportion of spinel relative to Earth's non-depleted mantle (only 4% versus 10%) (Hart and Zindler 1986).

CaO content affects the predicted solidus for Earth dry peridotites by affecting alkali (Na, K) partitioning behavior. Alkalis in the melt tend to lower the solidus temperature of dry peridotites, and as CaO increases, clinopyroxene increases, and alkalis such as Na become more compatible in the solid phases (Hirschmann 2000). For HEX1, alkali and Ca content are the same as for Earth's undepleted mantle (Hart and Zindler 1986) and so as expected, HEX1's solidus does not deviate from that of Earth (Fig. 4.3 A). However HEX2, whose solidus deviates quite a bit from that of Earth and HEX1 (Fig. 4.3 B), has a bulk composition with almost 1 wt% more CaO and a similar amount of alkalis as Earth's undepleted mantle, although they are solely in the form of Na_2O (Table 4.1). HEX2 melts are enriched in CaO and low in alkalis as described above, although here we do not observe a wholesale increase or decrease in the solidus temperature at each pressure, rather the HEX2 solidus is shallow compared to that of Earth and HEX1 (Fig. 4.3 B). Although workers have used similar experiments to predict the location of mantle solidi for other rocky bodies in our solar system (e.g., Yao and Liang 2012; Kiefer et al. 2015), the HEX2 solidus remains unusual in its slope and location.

4.4.2 Decompression Melting

The petrological conditions explored herein are relevant for silicate planets with a differentiated core. Decompression melting is the most simple—and widely-applicable—mantle melting scenario to which our results may be applied. Decompression melting is melting caused by the adiabatic ascent of mantle material. This process does not require Earth-style plate tectonics and could result instead from rebound of the crust due to impacts or ice removal, destruction of crust via delamination as could occur on a stagnant lid planet, or other recycling mechanisms.

Current models indicate that the adiabatic gradients ($\frac{dT}{dP}$) of rocky exoplanets are most sensitive to interior structure as represented by core-mass fraction (CMF; a ratio indicating what proportion

of the bulk planet's Fe resides in the core) (Unterborn and Panero 2019). Therefore when considering decompression melting within these exoplanets, if we assume HEX1 and HEX2 have the same CMF as Earth ($\sim$0.323) and a similar size, we may also assume they have a similar adiabatic gradient ($\sim$1.2°C/kbar or $\sim$0.3°C/km) (Grove and Till 2015). If we pin this mantle adiabat to the surface at modern-day estimates for Earth's mantle potential temperature (T_{pot}), 1350–1476°C (Putirka 2005; Herzberg et al. 2010), we find that the HEX1 dry solidus is steep enough such that adiabatically ascending material will cross this solidus and begin to melt by $\sim$20 kbar (with higher pressures of first melting expected as T_{pot} increases). However, the solidus of HEX2 is so shallow, that there is a narrow range of T_{pot} that would ensure the adiabat crossed the solidus but did not remain above or below it throughout the upper mantle. As T_{pot} is thought to have been higher (1500–1600°C) throughout much of Earth's history (Herzberg et al. 2010) it is reasonable to consider the possibility that for HEX2, mantle melting could begin a much greater pressures and perhaps depths than we're used to considering, and thus could result in greater total extents of melting.

After the mantle begins to melt, the liquid must segregate from the solid residuum and ascend, where it may either erupt onto the surface or stall in the crust. We can estimate the effect the difference between the densities of the melt and of the residuum has on the relative velocities of each (Daines and Pec 2015). Using DensityX (Iacovino and Till 2018), a program that calculates the density of dry and hydrous silicate melts based on pressure, temperature, and composition, we calculate the anhydrous densities of HEX1 and HEX2 melt at near-solidus conditions to be 2.92 g/cm^3 and 2.93 g/cm^3, respectively. These values are at the high end of Earth dry natural magma densities (Iacovino and Till 2018). Residuum densities were determined using the mantle modes (Table 4.3) and average densities of the appropriate minerals (mindat.org) and found to be 3.39 g/cm^3 for HEX1 and 3.29 g/cm^3 for HEX2. We completed the same procedure for average MORB (Gale et al. 2013) and Earth mantle modes (Hart and Zindler 1986). In comparing Earth, HEX1, and HEX2, we find that for the same porosity, viscosity, g, and melt fraction extracted, Earth will have the fastest melt migration velocity and HEX2 the slowest (Daines and Pec 2015); compared to the velocity of Earth melts, HEX1's melt migration velocity will be $\sim$20% slower and HEX2's melt migration velocity will be $\sim$55% slower.

This slower migration rate indicates that perhaps HEX2's melts are more likely to stall and crystallize as igneous intrusions, or that generated melt may fail to coalesce into an eruptible melt altogether.

4.4.3 Magma Ocean Crystallization

These experiments may be applied to exoplanets with magma oceans, as we have ascertained part of the crystallization sequence for these hypothetical exoplanets, and so can make inferences about the minerals available to form flotation crusts or cumulates. Although we have not observed the beginning of the crystallization sequences for our hypothetical exoplanets, we can use the phase assemblages and melting reactions we derived from them (Table 4.2, Fig. 4.3) to infer that in a HEX1 magma ocean, olivine would be the first phase to crystallize, followed by spinel, opx, and cpx. In a HEX2 magma ocean, the first mineral would likely be olivine, then opx, spinel, and cpx. All of these minerals are more dense than the melt, and so it is possible that an olivine-rich cumulate may form.

Formation of a flotation crust on either of these exoplanets is unlikely; we usually think of flotation crusts as being composed of a low-density phase such as plagioclase, specifically the Ca-rich end member, anorthite, as on the Moon. Plagioclase is not present in HEX1 or HEX2, but we cannot rule out the possibility that a flotation crust would form—we did not conduct experiments below 10 kbar which is the pressure range where plagioclase generally becomes stable on Earth. However, our starting compositions were Na-limited, which may preclude plagioclase stability in these systems.

4.4.4 Implications for Volcanic Degassing

Our knowledge of rocky exoplanets is largely limited to their host star composition, amount of stellar irradiance, orbital radius, mass, and planetary radius (atmospheric thickness is included in this measurement). There are methods to detect or infer the presence of an atmosphere (e.g., Kreidberg 2018; Koll et al. 2019; Kreidberg et al. 2019; Mansfield et al. 2019) and spectroscopic characterization of exoplanet atmospheres will soon be possible via missions such as NASA's James Webb Space Telescope (JWST) and ESA's Atmospheric Remote-sensing Infrared Exoplanet Large-survey

(ARIEL). Unfortunately, we are not likely to measure surface spectra until missions such as NASA's Large UV/Optical/IR Surveyor (LUVOIR), so it behooves us to experimentally investigate exoplanet melt compositions because the link between atmospheric composition, outgassed volatiles, and melt composition may allow us to deduce geochemical properties of the solid interior from atmospheric spectra. This capability will continue to grow rapidly in the next 5–10 years as missions such as JWST and ARIEL become active.

H_2O and CO_2 are the two most abundant volcanic volatiles. A solubility model based on experimental and natural data shows that as SiO_2 content increases, H_2O solubility increases but CO_2 solubility decreases (Papale et al. 2006). This model predicts that at 4 kbar HEX1 and HEX2 melts may be able to carry $\sim$2.5 wt% H_2O and > 2700 ppm CO_2 (Papale et al. 2006). Unfortunately, although H_2O and CO_2 may be measured via telescopic spectrometry, at present we lack the ability to confirm a volcanic origin for these volatiles.

Sulfur compounds are more distinctly-volcanic fingerprints than H_2O or CO_2. The volcanic volatile SO_2 is less vulnerable to photolysis in the stratosphere than H_2S and so is a promising candidate for detection in exoplanet atmospheres (Robock 2000). The solubility of sulfur in basaltic melts has been the subject of much study (e.g., Keppler 1999; Holzheid and Grove 2002; Oppenheimer et al. 2011; Webster et al. 2014; Wykes et al. 2015): above $\sim$5 wt%, as the FeO content of a melt increases, so does the amount of sulfur that can be carried in that melt (O'Neill and Mavrogenes 2002), regardless of water content (Wykes et al. 2015). The FeO content of HEX1 and HEX2 melts (7–15 wt%) is comparable to that of Earth ocean island basalts (OIB; 7–16 wt%) and MORBs (7–15 wt%) (Fig. 4.4) and so based on this we may expect these hypothetical exoplanets to carry approximately the same amount of sulfur as Earth ($\sim$1500–2000 ppm at sulfur saturation; O'Neill and Mavrogenes 2002).

The melts produced by melting the variety of bulk silicate compositions that we infer from Figure 4.2 could result in outgassed secondary atmospheres that are very different from our own, as well as give us clues to eruption styles. Note that on Figure 4.2, our sun plots in the midrange of FeO content with many stars containing more or less FeO, indicating that exoplanets originating from the same solar nebulae as these stars may have a far different sulfur carrying capacity than Earth. It is possible that putative exoplanets could also have different solubilities of H_2O and CO_2. Since the amount of

volatiles dissolved in magma affects its viscosity and density and because these parameters affect the explosivity of eruptions, these volatile solubilities directly influence the eruption style of a volcanic system (e.g., Hess and Dingwell 1996; Ochs and Lange 1999). And, the more explosive the eruption, the more likely it is that volcanic gasses could be injected into the stratosphere where they may persist long enough to be measured.

4.5   Conclusions

An experimental determination of rocky exoplanet mantle mineralogy and mantle-derived melt compositions is the foundation for understanding the geochemical relationships between the subsurface, surface, and atmosphere of these foreign bodies. This work represents an early step towards a future when the discipline of exoplanet science is not limited to extrapolation from Earth-composition data. Most, if not all, of our existing models depend on the melting reactions, mineral assemblages, and general rules of thumb that are based on our petrological understanding of how bodies in our solar system—mainly Earth—work. Using a few available petrologic models (Brown et al. in review; Ghiorso and Sack 1995; Ghiorso et al. 2002; Stixrude and Lithgow-Bertelloni 2005; Gualda et al. 2012; Behn and Grove 2015), we attempted to replicate the melt compositions and phase assemblages produced by our experiments. All failed to yield comparable or realistic results e.g., major phases were omitted, liquidi were calculated at subsolidus temperatures, or models never converged on a solution.

New models for exoplanet petrology are needed if we want to assess the chemical composition of exoplanet crusts in order to eventually evaluate their potential to support life. However, more experiments are needed. There is a vast composition space yet to be explored (Fig. 4.2) and in addition to determining melt compositions and volatile solubilities, we need to be able to better calculate equations of state for the higher pressures and temperatures of super-Earths so we aren't forced to extrapolate these equations far beyond their empirical foundation (Unterborn and Panero 2019). As it is not practical to conduct experiments on every potential HZ exoplanet, to calibrate these models we suggest targeting experiments at end member compositions of exoplanets, as well as exoplanets that occupy

regions of geochemistry that have not been studied due to their dissimilarity to the compositions of rocky planets in our solar system.

Using JWST and ARIEL atmospheric spectra and volatile solubilities, it may be possible to make inferences about the bulk silicate exoplanets capable of exhibiting certain atmospheric compositions. Workers are already constructing models and striving to optimize instrumental and observing modes to interpret these future data (e.g., Greene et al. 2016; Batalha et al. 2018; Lustig-Yaeger et al. 2019). Although it may be decades before we have sufficient exoplanet models and observations to test these results, it is critical to begin creating the exoplanet partial mantle melt compositional data needed to facilitate such investigations so that we are prepared for these future opportunities.

Acknowledgements

References

Batalha, N.E., Lewis, N.K., Line, M.R., Valenti, J., and Stevenson, K. (2018) Strategies for Constraining the Atmospheres of Temperate Terrestrial Planets with JWST. The Astrophysical Journal, 856, L34.

Behn, M.D., and Grove, T.L. (2015) Melting systematics in mid-ocean ridge basalts: Application of a plagioclase-spinel melting model to global variations in major element chemistry and crustal thickness: MID-OCEAN RIDGE MELTING SYSTEMATICS. Journal of Geophysical Research: Solid Earth, 120, 4863–4886.

Boyd, F.R., and England, J.L. (1960) Apparatus for Phase-Equilibrium Measurements at Pressures up to 50 Kilobars and Temperatures up to 17500C. Journal of Geophysical Research, 65, 741–748.

Brown, S.B., Behn, M.D., and Grove, T.L. (in review) The Origin of Major Element, Trace Element, and Isotope Garnet Signatures in Mid-Ocean Ridge Basalts. Journal of Geophysical Research: Solid Earth.

Daines, M.J., and Pec, M. (2015) Ch. 2: Migration of Melt. In The Encyclopedia of Volcanoes. Elsevier/AP, Amsterdam; Boston. Desch, S. (2014) Exoplanetary Ecosystems: Exploring life's detectability on chemically diverse exoplanets.

Dorn, C., Noack, L., and Rozel, A.B. (2018) Outgassing on stagnant-lid super-Earths. Astronomy & Astrophysics, 614, A18. Feldman, U. (1992) Elemental abundances in the upper solar atmosphere. Physica Scripta, 46, 202–220.

Filiberto, J. (2014) Magmatic diversity on Venus: Constraints from terrestrial analog crystallization experiments. Icarus, 231, 131–136.

Fulton, B.J., Petigura, E.A., Howard, A.W., Isaacson, H., Marcy, G.W., Cargile, P.A., Hebb, L., Weiss, L.M., Johnson, J.A., Morton, T.D., and others (2017) The California-*Kepler* Survey. III. A Gap in the Radius Distribution of Small Planets. The Astronomical Journal, 154, 109.

Gale, A., Dalton, C.A., Langmuir, C.H., Su, Y., and Schilling, J.-G. (2013) The mean composition of ocean ridge basalts: MEAN MORB. Geochemistry, Geophysics, Geosystems, 14, 489–518.

Ghiorso, M.S., and Sack, R.O. (1995) Chemical mass transfer in magmatic processes IV. A revised and internally consistent thermodynamic model for the interpolation and extrapolation of liquid-solid equilibria in magmatic systems at elevated temperatures and pressures. Contributions to Mineralogy and Petrology, 119, 197–212.

Ghiorso, M.S., Hirschmann, M.M., Reiners, P.W., and Kress, V.C. (2002) The pMELTS: A revision of MELTS for improved calculation of phase relations and major element partitioning related to partial melting of the mantle to 3 GPa: pMELTS, A REVISION OF MELTS. Geochemistry, Geophysics, Geosystems, 3, 1–35.

Greene, T.P., Line, M.R., Montero, C., Fortney, J.J., Lustig-Yaeger, J., and Luther, K. (2016) Characterizing Transiting Exoplanet Atmospheres with JWST. The Astrophysical Journal, 817, 17. Grove, T.L., and Krawczynski, M.J. (2009) Lunar Mare Volcanism: Where Did the Magmas Come From? Elements, 5, 29–34.

Grove, T.L., and Till, C.B. (2015) Melting the Earth's Upper Mantle. In Encyclopedia of Volcanos. Elsevier/AP, Amsterdam; Boston. Gualda, G.A.R., Ghiorso, M.S., Lemons, R.V., and Carley,

T.L. (2012) Rhyolite-MELTS: a Modified Calibration of MELTS Optimized for Silica-rich, Fluid-bearing Magmatic Systems. Journal of Petrology, 53, 875–890.

Hakim, K., Spaargaren, R., Grewal, D.S., Rohrbach, A., Berndt, J., Dominik, C., and van Westrenen, W. (2019) Mineralogy, Structure, and Habitability of Carbon-Enriched Rocky Exoplanets: A Laboratory Approach. Astrobiology, 19, 867–884.

Hart, S.R., and Zindler, A. (1986) In Search of a Bulk-Earth Composition. Chemical Geology, 57, 247–267. Hays, J.F. (1966) Lime-Alumina-Silica, 234–239.

Herzberg, C., Condie, K., and Korenaga, J. (2010) Thermal history of the Earth and its petrological expression. Earth and Planetary Science Letters, 292, 79–88.

Hess, K.-U., and Dingwell, D.D. (1996) Viscosities of hydrous leucogranitic melts: A non-Arrhenian model. American Mineralogist, 81, 1297–1300.

Hinkel, N.R., and Unterborn, C.T. (2018) The Star–Planet Connection. I. Using Stellar Composition to Observationally Constrain Planetary Mineralogy for the 10 Closest Stars. The Astrophysical Journal, 853, 83.

Hinkel, N.R., Timmes, F.X., Young, P.A., Pagano, M.D., and Turnbull, M.C. (2014) Stellar Abundances in the Solar Neighborhood: The Hypatia Catalog. The Astronomical Journal, 148, 54.

Hirschmann, M.M. (2000) Mantle solidus: Experimental constraints and the effects of peridotite composition. Geochemistry, Geophysics, Geosystems, 1.

Holzheid, A., and Grove, T.L. (2002) Sulfur saturation limits in silicate melts and their implications for core formation scenarios for terrestrial planets. American Mineralogist, 87, 227–237.

Hu, R., Seager, S., and Bains, W. (2012) Photochemistry in Terrestrial Exoplanet Atmospheres. I. Photochemistry Model and Benchmark Cases. The Astrophysical Journal, 761, 166.

Iacovino, K., and Till, C. (2018) DensityX: A program for calculating the densities of hydrous magmatic liquids from 427-1,627 °C and up to 30 kbar. Volcanica, 2, 1–10.

Johnson, J.A., Petigura, E.A., Fulton, B.J., Marcy, G.W., Howard, A.W., Isaacson, H., Hebb, L., Cargile, P.A., Morton, T.D., Weiss, L.M., and others (2017) The California-*Kepler* Survey. II. Precise Physical Properties of 2025 *Kepler* Planets and Their Host Stars. The Astronomical Journal, 154, 108.

Kane, S.R., Hill, M.L., Kasting, J.F., Kopparapu, R.K., Quintana, E.V., Barclay, T., Batalha, N.M., Borucki, W.J., Ciardi, D.R., Haghighipour, N., and others (2016) A Catalog of *Kepler* Habitable Zone Exoplanet Candidates. The Astrophysical Journal, 830, 1.

Kasting, J.F., Whitmire, D.P., and Reynolds, R.T. (1993) Habitable Zones around Main Sequence Stars. Icarus, 101, 108–128.

Keppler, H. (1999) Experimental Evidence for the Source of Excess Sulfur in Explosive Volcanic Eruptions. Science, 284, 1652–1654.

Kiefer, W.S., Filiberto, J., Sandu, C., and Li, Q. (2015) The effects of mantle composition on the peridotite solidus: Implications for the magmatic history of Mars. Geochimica et Cosmochimica Acta, 162, 247–258.

Kinzler, R.J., and Grove, T.L. (1992) Primary magmas of mid-ocean ridge basalts 1. Experiments and methods. Journal of Geophysical Research, 97, 6885.

Koll, D.D.B., Malik, M., Mansfield, M., Kempton, E.M.-R., Kite, E., Abbot, D., and Bean, J.L. (2019) Identifying Candidate Atmospheres on Rocky M dwarf Planets via Eclipse Photometry. arXiv:1907.13138 [astro-ph].

Kopparapu, R.K., Ramirez, R.M., SchottelKotte, J., Kasting, J.F., Domagal-Goldman, S., and Eymet, V. (2014) Habitable zones around main-sequence stars: dependence on planetary mass. The Astrophysical Journal, 787, L29.

Krawczynski, M.J., and Grove, T.L. (2012) Experimental investigation of the influence of oxygen fugacity on the source depths for high titanium lunar ultramafic magmas. Geochimica et Cosmochimica Acta, 79, 1–19. Kreidberg, L. (2018) Exoplanet Atmosphere Measurements from Transmission Spectroscopy and Other Planet Star Combined Light Observations. In H. Deeg and J. Belmonte, Eds., Handbook of Exoplanets pp. 1–23. Springer, Cham.

Kreidberg, L., Koll, D.D.B., Morley, C., Hu, R., Schaefer, L., Deming, D., Stevenson, K.B., Dittmann, J., Vanderburg, A., Berardo, D., and others (2019) Absence of a thick atmosphere on the terrestrial exoplanet LHS 3844b. Nature, 573, 87–90.

Longhi, J. (2005) Temporal stability and pressure calibration of barium carbonate and talc/pyrex pressure media in a piston-cylinder apparatus. American Mineralogist, 90, 206–218.

Lustig-Yaeger, J., Meadows, V.S., and Lincowski, A.P. (2019) The Detectability and Characterization of the TRAPPIST-1 Exoplanet Atmospheres with JWST. The Astronomical Journal, 158, 27.

Mansfield, M., Kite, E.S., Hu, R., Koll, D.D.B., Malik, M., Bean, J.L., and Kempton, E.M.-R. (2019) Identifying Atmospheres on Rocky Exoplanets Through Inferred High Albedo. arXiv:1907.13150 [astro-ph].

Martinez, C.F., Cunha, K., Ghezzi, L., and Smith, V.V. (2019) A Spectroscopic Analysis of the California-*Kepler* Survey Sample. I. Stellar Parameters, Planetary Radii, and a Slope in the Radius Gap. The Astrophysical Journal, 875, 29.

Médard, E., and Grove, T.L. (2006) Early hydrous melting and degassing of the Martian interior. Journal of Geophysical Research, 111.

Namur, O., Collinet, M., Charlier, B., Grove, T.L., Holtz, F., and McCammon, C. (2016) Melting processes and mantle sources of lavas on Mercury. Earth and Planetary Science Letters, 439, 117–128.

Nisr, C., Meng, Y., MacDowell, A.A., Yan, J., Prakapenka, V., and Shim, S.-H. (2017) Thermal Expansion of SiC at High Pressure–Temperature and Implications for Thermal Convection in the Deep Interiors of Carbide Exoplanets. Journal of Geophysical Research: Planets, 122, 124–133.

Ochs, F.A.I., and Lange, R.A. (1999) The density of hydrous magmatic liquids. Science, 283, 1314–1317.

O'Neill, H.S.C., and Mavrogenes, J.A. (2002) The Sulfide Capacity and the Sulfur Content at Sulfide Saturation of Silicate Melts at 1400°C and 1 bar, 43, 39.

Oppenheimer, C., Scaillet, B., and Martin, R.S. (2011) Sulfur Degassing From Volcanoes: Source Conditions, Surveillance, Plume Chemistry and Earth System Impacts. Reviews in Mineralogy and Geochemistry, 73, 363–421.

Owen, J.E., and Wu, Y. (2013) *Kepler* Planets: A Tale of Photoevaporation. The Astrophysical Journal, 775, 105.

Papale, P., Moretti, R., and Barbato, D. (2006) The compositional dependence of the saturation surface of H_2O+CO_2 fluids in silicate melts. Chemical Geology, 229, 78–95.

Petigura, E.A., Howard, A.W., Marcy, G.W., Johnson, J.A., Isaacson, H., Cargile, P.A., Hebb, L., Fulton, B.J., Weiss, L.M., Morton, T.D., and others (2017) The California-*Kepler* Survey. I. High-resolution Spectroscopy of 1305 Stars Hosting *Kepler* Transiting Planets. The Astronomical Journal, 154, 107.

Putirka, K. (2016) Rates and styles of planetary cooling on Earth, Moon, Mars, and Vesta, using new models for oxygen fugacity, ferric-ferrous ratios, olivine-liquid Fe-Mg exchange, and mantle potential temperature. American Mineralogist, 101, 819–840.

Putirka, K., Johnson, M., Kinzler, R., Longhi, J., and Walker, D. (1996) Thermobarometry of mafic igneous rocks based on clinopyroxene-liquid equilibria, 0–30 kbar. Contributions to Mineralogy and Petrology, 123, 92–108.

Putirka, K.D. (2005) Mantle potential temperatures at Hawaii, Iceland, and the mid-ocean ridge system, as inferred from olivine phenocrysts: Evidence for thermally driven mantle plumes. Geochemistry, Geophysics, Geosystems, 6.

Robock, A. (2000) Volcanic eruptions and climate. Reviews of Geophysics, 38, 191–219.

Santos, A.R., Agee, C.B., McCubbin, F.M., Shearer, C.K., Burger, P.V., Tartèse, R., and Anand, M. (2015) Petrology of igneous clasts in Northwest Africa 7034: Implications for the petrologic diversity of the martian crust. Geochimica et Cosmochimica Acta, 157, 56–85.

Schwieterman, E.W., Kiang, N.Y., Parenteau, M.N., Harman, C.E., DasSarma, S., Fisher, T.M., Arney, G.N., Hartnett, H.E., Reinhard, C.T., Olson, S.L., and others (2018) Exoplanet Biosignatures: A Review of Remotely Detectable Signs of Life. Astrobiology, 18, 663–708.

Squyres, S.W., Aharonson, O., Clark, B.C., Cohen, B.A., Crumpler, L., de Souza, P.A., Farrand, W.H., Gellert, R., Grant, J., Grotzinger, J.P., and others (2007) Pyroclastic Activity at Home Plate in Gusev Crater, Mars. Science, 316, 738–742.

Stixrude, L., and Lithgow-Bertelloni, C. (2005) Thermodynamics of mantle minerals - I. Physical properties. Geophysical Journal International, 162, 610–632.

Treiman, A.H. (2007) Geochemistry of Venus' Surface: Current limitations as future opportunities. In L.W. Esposito, E.R. Stofan, and T.E. Cravens, Eds., Geophysical Monograph Series Vol. 176, pp. 7–22. American Geophysical Union, Washington, D. C.

Unterborn, C.T., and Panero, W.R. (2019) The Pressure and Temperature Limits of Likely Rocky Exoplanets. Journal of Geophysical Research: Planets, 124, 1704–1716.

Vander Kaaden, K.E., McCubbin, F.M., Nittler, L.R., Peplowski, P.N., Weider, S.Z., Frank, E.A., and McCoy, T.J. (2017) Geochemistry, mineralogy, and petrology of boninitic and komatiitic rocks on the mercurian surface: Insights into the mercurian mantle. Icarus, 285, 155–168.

Wadhwa, M. (2008) Redox Conditions on Small Bodies, the Moon and Mars. Reviews in Mineralogy and Geochemistry, 68, 493–510.

Watson, E., Wark, D., Price, J., and Van Orman, J. (2002) Mapping the thermal structure of solid-media pressure assemblies. Contributions to Mineralogy and Petrology, 142, 640–652.

Webster, J.D., Goldoff, B., Sintoni, M.F., Shimizu, N., and De Vivo, B. (2014) C-O-H-Cl-S-F Volatile Solubilities, Partitioning, and Mixing in Phonolitic-Trachytic Melts and Aqueous-Carbonic Vapor Saline Liquid at 200 MPa. Journal of Petrology, 55, 2217–2248.

Weiss, L.M., Marcy, G.W., Petigura, E.A., Fulton, B.J., Howard, A.W., Winn, J.N., Isaacson, H.T., Morton, T.D., Hirsch, L.A., Sinukoff, E.J., and others (2018) The California-*Kepler* Survey. V. Peas in a Pod: Planets in a *Kepler* Multi-planet System Are Similar in Size and Regularly Spaced. The Astronomical Journal, 155, 48.

Wolszczan, A., and Frail, D. (1992) A planetary system around the millisecond pulsar PSR1257 + 12. Nature, 355, 145–147.

Wykes, J.L., O'Neill, H.St.C., and Mavrogenes, J.A. (2015) The Effect of FeO on the Sulfur Content at Sulfide Saturation (SCSS) and the Selenium Content at Selenide Saturation of Silicate Melts. Journal of Petrology, 56, 1407–1424.

Yao, L., and Liang, Y. (2012) An experimental study of the solidus of a hybrid lunar cumulate mantle: implications for the temperature at the core-mantle boundary of the moon. Presented at the Lunar and Planetary Science Conference, Woodlands, TX.

Young, P.A., Desch, S.J., Anbar, A.D., Barnes, R., Hinkel, N.R., Kopparapu, R., Madhusudhan, N., Monga, N., Pagano, M.D., Riner, M.A., and others (2014) Astrobiological Stoichiometry. Astrobiology, 14, 603–626.

Chapter 5

PROSPECTUS

The work presented in this dissertation describes how I have refined tools petrologists use to investigate magmatic and volcanic systems and how I used them to improve our understanding of specific magmatic settings. I have endeavored to address gaps and faulty assumptions in our knowledge: the unique characteristics of a mineral in a given system may require a specialized tool (in Chapter 2, a specially-calibrated geothermometer); in some cases the thermal and physical characteristics of the magmatic system render typical assumptions insufficient (in Chapter 3, utilizing a proxy to the initial condition instead of a step-function shape when calculating diffusion timescales in cases of crystal growth followed by chemical diffusion); and the petrological relationships we are accustomed to relying on as shorthand may not apply when the bulk composition is significantly shifted, so they must be tested via experimentation (in Chapter 4, when turning our attention to planets orbiting stars whose composition deviate from that of Earth and the sun).

As igneous petrology increasingly moves towards thermodynamic and qualitative models, it is crucial that these simulations are appropriately calibrated and benchmarked. I anticipate the demand for petrological experiments similar to those presented in Chapter 4 to rise as interest in exoplanets flourishes and efforts move towards modeling more complex systems, as well as an increased interest in unification of models e.g., the ENKI project (enki-portal.org), an open source Bayesian update of MELTS (Ghiorso and Sack 1995; Ghiorso et al. 2002; Gualda et al. 2012; Ghiorso and Gualda 2015). If we wish to interpret exoplanet atmospheric compositions, it is essential to understand the amount of volatiles that could be released into the atmosphere by volcanism. Determining the volatile solubilities of exoplanet mantle-derived melts is surely the next step in understanding the petrology of these exotic worlds.

The use of diffusion chronometry is becoming more popular, and as this is a method whose results must be interpreted in concert with information such as phase equilibria and crystal growth and dissolution rates (Ch. 3), it is incumbent on the experimental petrology community to determine diffusion

rates of elements in rhyolitic melts as well as growth and dissolution rates of minerals in high-silica systems. These experiments are generally considered to be risky, as the low temperatures and slow kinetics of these systems require long equilibration times and therefore very long experimental run times. However, it is difficult to properly contextualize diffusion modeling results if we are unsure of the amount of time, and what magmatic conditions are required, in order to a) deliver elements to a mineral crystal's growth surface fast enough to prevent formation of a boundary layer; and b) grow a thick enough rim such that we could expect chemical variation in the new growth to be measurable at the spatial resolution of our analytical techniques.

One of the main goals of volcanological and petrological research is to amass enough data to create a statistically driven eruption forecasting model. But to calibrate such a model requires a full understanding of the uncertainty attached to the input data; in the case of magmatic timescales calculated using diffusion chronometry, uncertainty has thus far been underreported and the timescales themselves may be gross overestimates. In Chapter 3 I have attempted to bolster this aspect of diffusion chronometry and welcome further refinements in this area.

Experimental petrology has been used to study other planets and moons in our solar system (Wadhwa 2008; Grove and Krawczynski 2009; Krawczynski and Grove 2012; Filiberto 2014; Kiefer et al. 2015; Namur et al. 2016; Putirka 2016; Vander Kaaden et al. 2017; and references therein) and these studies have helped to contextualize satellite observations and influence the types of measurements and instrumentation used on subsequent missions. In essence, experimental petrology has helped us ask better questions as we endeavor to better understand not only Earth, but the behavior and composition of all planetary bodies. I look forward to seeing the fields of igneous diffusion chronometry and exoplanet petrology mature in coming years and am eager to help expand our understanding of magmatic processes, whether they are based on Earth, elsewhere in our solar system, or beyond.

References

Filiberto, J. (2014) Magmatic diversity on Venus: Constraints from terrestrial analog crystallization experiments. Icarus, 231, 131–136.

Ghiorso, M.S., and Gualda, G.A.R. (2015) An H_2O–CO_2 mixed fluid saturation model compatible with rhyolite-MELTS. Contributions to Mineralogy and Petrology, 169.

Ghiorso, M.S., and Sack, R.O. (1995) Chemical mass transfer in magmatic processes IV. A revised and internally consistent thermodynamic model for the interpolation and extrapolation of liquid-solid equilibria in magmatic systems at elevated temperatures and pressures. Contributions to Mineralogy and Petrology, 119, 197–212.

Ghiorso, M.S., Hirschmann, M.M., Reiners, P.W., and Kress, V.C. (2002) The pMELTS: A revision of MELTS for improved calculation of phase relations and major element partitioning related to partial melting of the mantle to 3 GPa: pMELTS, A REVISION OF MELTS. Geochemistry, Geophysics, Geosystems, 3, 1–35.

Grove, T.L., and Krawczynski, M.J. (2009) Lunar Mare Volcanism: Where Did the Magmas Come From? Elements, 5, 29–34.

Gualda, G.A.R., Ghiorso, M.S., Lemons, R.V., and Carley, T.L. (2012) Rhyolite-MELTS: a Modified Calibration of MELTS Optimized for Silica-rich, Fluid-bearing Magmatic Systems. Journal of Petrology, 53, 875–890.

Kiefer, W.S., Filiberto, J., Sandu, C., and Li, Q. (2015) The effects of mantle composition on the peridotite solidus: Implications for the magmatic history of Mars. Geochimica et Cosmochimica Acta, 162, 247–258.

Krawczynski, M.J., and Grove, T.L. (2012) Experimental investigation of the influence of oxygen fugacity on the source depths for high titanium lunar ultramafic magmas. Geochimica et Cosmochimica Acta, 79, 1–19.

Namur, O., Collinet, M., Charlier, B., Grove, T.L., Holtz, F., and McCammon, C. (2016) Melting processes and mantle sources of lavas on Mercury. Earth and Planetary Science Letters, 439, 117–128.

Putirka, K. (2016) Rates and styles of planetary cooling on Earth, Moon, Mars, and Vesta, using new models for oxygen fugacity, ferric-ferrous ratios, olivine-liquid Fe-Mg exchange, and mantle potential temperature. American Mineralogist, 101, 819–840.

Vander Kaaden, K.E., McCubbin, F.M., Nittler, L.R., Peplowski, P.N., Weider, S.Z., Frank, E.A., and McCoy, T.J. (2017) Geochemistry, mineralogy, and petrology of boninitic and komatiitic rocks on the mercurian surface: Insights into the mercurian mantle. Icarus, 285, 155–168.

Wadhwa, M. (2008) Redox Conditions on Small Bodies, the Moon and Mars. Reviews in Mineralogy and Geochemistry, 68, 493–510.

REFERENCES

Albert, H., Costa, F., and Martí, J. (2015) Timing of Magmatic Processes and Unrest Associated with Mafic Historical Monogenetic Eruptions in Tenerife Island. Journal of Petrology, egv058.

Allan, A.S.R., Morgan, D.J., Wilson, C.J.N., and Millet, M.-A. (2013) From mush to eruption in centuries: assembly of the super-sized Oruanui magma body. Contributions to Mineralogy and Petrology, 166, 143–164.

Almeev, R.R., Bolte, T., Nash, B.P., Holtz, F., Erdmann, M., and Cathey, H.E. (2012) High-temperature, low-H_2O Silicic Magmas of the Yellowstone Hotspot: an Experimental Study of Rhyolite from the Bruneau-Jarbidge Eruptive Center, Central Snake River Plain, USA. Journal of Petrology, 53, 1837–1866.

Andersen, N.L., Singer, B.S., Costa, F., Fournelle, J., Herrin, J.S., and Fabbro, G.N. (2018) Petrochronologic perspective on rhyolite volcano unrest at Laguna del Maule, Chile. Earth and Planetary Science Letters, 493, 57–70.

Anderson, A.T., Davis, A.M., and Lu, F. (2000) Evolution of Bishop Tuff Rhyolitic Magma Based on Melt and Magnetite Inclusions and Zoned Phenocrysts. Journal of Petrology, 41, 449–473.

Anderson, D.J., Lindsley, D.H., and Davidson, P.M. (1993) QUILF: A pascal program to assess equilibria among Fe, Mg, Mn, Ti oxides, pyroxenes, olivine, and quartz. Computers & Geosciences, 19, 1333–1350.

Azough, F., and Freer, R. (2000) Iron diffusion in single-crystal diopside. Phys Chem Minerals, 27, 732–740.

Bachmann, O., and Bergantz, G.W. (2006) Gas percolation in upper-crustal silicic crystal mushes as a mechanism for upward heat advection and rejuvenation of near-solidus magma bodies. Journal of Volcanology and Geothermal Research, 149, 85–102.

Bartels, K.S., Kinzler, R.J., and Grove, T.L. (1991) High pressure phase relations of primitive high-alumina basalts from Medicine Lake volcano, northern California. Contributions to Mineralogy and Petrology, 108, 253–270.

Batalha, N.E., Lewis, N.K., Line, M.R., Valenti, J., and Stevenson, K. (2018) Strategies for Constraining the Atmospheres of Temperate Terrestrial Planets with JWST. The Astrophysical Journal, 856, L34.

Befus, K.S., and Gardner, J.E. (2016) Magma storage and evolution of the most recent effusive and explosive eruptions from Yellowstone Caldera. Contributions to Mineralogy and Petrology, 171.

Befus, K.S., Bruyere, R.H., and Manga, M. (2018) Lava Creek Tuff Love. Presented at the Goldschmidt, Boston, MA, USA.

Beghein, C. (2010) Radial anisotropy and prior petrological constraints: A comparative study. Journal of Geophysical Research, 115.

Behn, M.D., and Grove, T.L. (2015) Melting systematics in mid-ocean ridge basalts: Application of a plagioclase-spinel melting model to global variations in major element chemistry and crustal thickness: MID-OCEAN RIDGE MELTING SYSTEMATICS. Journal of Geophysical Research: Solid Earth, 120, 4863–4886.

Bindeman, I.N., and Valley, J.W. (2001) Low-δ18O Rhyolites from Yellowstone: Magmatic Evolution Based on Analyses of Zircons and Individual Phenocrysts. Journal of Petrology, 42, 1491–1517.

——— (2002) Oxygen isotope study of the Long Valley magma system, California: isotope thermometry and convection in large silicic magma bodies. Contributions to Mineralogy and Petrology, 144, 185–205.

Bindeman, I.N., Fu, B., Kita, N.T., and Valley, J.W. (2008) Origin and Evolution of Silicic Magmatism at Yellowstone Based on Ion Microprobe Analysis of Isotopically Zoned Zircons. Journal of Petrology, 49, 163–193.

Bolte, T., Holtz, F., Almeev, R., and Nash, B. (2015) The Blacktail Creek Tuff: an analytical and experimental study of rhyolites from the Heise volcanic field, Yellowstone hotspot system. Contributions to Mineralogy and Petrology, 169.

Bouvet de Maisonneuve, C., Costa, F., Huber, C., Vonlanthen, P., Bachmann, O., and Dungan, M.A. (2016) How do olivines record magmatic events? Insights from major and trace element zoning. Contributions to Mineralogy and Petrology, 171.

Boyd, F.R., and England, J.L. (1960) Apparatus for Phase-Equilibrium Measurements at Pressures up to 50 Kilobars and Temperatures up to 1750°C. Journal of Geophysical Research, 65, 741–748.

Brown, S.B., Behn, M.D., and Grove, T.L. (in review) The Origin of Major Element, Trace Element, and Isotope Garnet Signatures in Mid-Ocean Ridge Basalts. Journal of Geophysical Research: Solid Earth.

Brugman, K.K., and Till, C.B. (2019) A low-aluminum clinopyroxene-liquid geothermometer for high-silica magmatic systems. American Mineralogist, 104, 996–1004.

Budd, D.A., Troll, V.R., Deegan, F.M., Jolis, E.M., Smith, V.C., Whitehouse, M.J., Harris, C., Freda, C., Hilton, D.R., Halldórsson, S.A., and others (2017) Magma reservoir dynamics at Toba caldera, Indonesia, recorded by oxygen isotope zoning in quartz. Scientific Reports, 7, 40624.

Byrne, P.K. (2019) A comparison of inner Solar System volcanism. Nature Astronomy, 4, 321–327.

Cashman, K.V., and Giordano, G. (2014) Calderas and magma reservoirs. Journal of Volcanology and Geothermal Research, 288, 28–45.

Chamberlain, K.J., Morgan, D.J., and Wilson, C.J.N. (2014) Timescales of mixing and mobilisation in

the Bishop Tuff magma body: perspectives from diffusion chronometry. Contributions to Mineralogy and Petrology, 168.

Chen, Y., and Zhang, Y. (2009) Clinopyroxene dissolution in basaltic melt. Geochimica et Cosmochimica Acta, 73, 5730–5747.

Christiansen, R.L. (2001) The Quaternary and Pliocene Yellowstone Plateau volcanic field of Wyoming, Idaho, and Montana, 145 p. U.S. Geological Survey, Reston, Va.

Christiansen, R.L., Lowenstern, J.B., Smith, R.B., Heasler, H., Morgan, L.A., Nathenson, M., Mastin, L.G., Muffler, L.J.P., and Robinson, J.E. (2007) Preliminary Assessment of Volcanic and Hydrothermal Hazards in Yellowstone National Park and Vicinity p. 94. USGS.

Civetta, L., D 'Antonio, M., Orsi, G., and Tilton, G.R. (1998) The geochemistry of volcanic rocks from Pantelleria Island, Sicily Channel: petrogenesis and characteristics of the mantle source region. Journal of Petrology, 39, 1453–1491.

Cooper, G.F., Morgan, D.J., and Wilson, C.J.N. (2017) Rapid assembly and rejuvenation of a large silicic magmatic system: Insights from mineral diffusive profiles in the Kidnappers and Rocky Hill deposits, New Zealand. Earth and Planetary Science Letters, 473, 1–13.

Cooper, K.M., and Kent, A.J.R. (2014) Rapid remobilization of magmatic crystals kept in cold storage. Nature, 506, 480–483.

Costa, F., and Chakraborty, S. (2004) Decadal time gaps between mafic intrusion and silicic eruption obtained from chemical zoning patterns in olivine. Earth and Planetary Science Letters, 227, 517–530.

Costa, F., and Dungan, M. (2005) Short time scales of magmatic assimilation from diffusion modeling of multiple elements in olivine. Geology, 33, 837–840.

Costa, F., and Morgan, D. (2011) Time Constraints from Chemical Equilibration in Magmatic Crystals. In Timescales of Magmatic Processes: From Core to Atmosphere pp. 123–159. Blackell Publishing, Ltd.

Costa, F., Chakraborty, S., and Dohmen, R. (2003) Diffusion coupling between trace and major elements and a model for calculation of magma residence times using plagioclase. Geochimica et Cosmochimica Acta, 67, 2189–2200.

Costa, F., Dohmen, R., and Chakraborty, S. (2008) Time Scales of Magmatic Processes from Modeling the Zoning Patterns of Crystals. Reviews in Mineralogy and Geochemistry, 69, 545–594.

Daines, M.J., and Pec, M. (2015) Migration of Melt. In The Encyclopedia of Volcanoes. Elsevier/AP, Amsterdam; Boston.

Degruyter, W., Huber, C., Bachmann, O., Cooper, K.M., and Kent, A.J.R. (2016) Magma reservoir response to transient recharge events: The case of Santorini volcano (Greece). Geology, 44, 23–26.

Dimanov, A., and Wiedenbeck, M. (2006) (Fe,Mn)-Mg interdiffusion in natural diopside: effect of pO$_2$. European Journal of Mineralogy, 18, 705–718.

Dorn, C., Noack, L., and Rozel, A.B. (2018) Outgassing on stagnant-lid super-Earths. Astronomy & Astrophysics, 614, A18.

Druitt, T.H., Costa, F., Deloule, E., Dungan, M., and Scaillet, B. (2012) Decadal to monthly timescales of magma transfer and reservoir growth at a caldera volcano. Nature, 482, 77–80.

Elkins, L.T., and Grove, T.L. (1990) Ternary feldspar experiments and thermodynamic models. American Mineralogist, 75, 544–559.

Elthon, D., and Scarfe, C.M. (1984) High-pressure phase equilibria of a high-magnesian basalt and the genesis of primary oceanic basalts. American Mineralogist, 69, 1–15.

Feig, S.T., Koepke, J., and Snow, J.E. (2006) Effect of water on tholeiitic basalt phase equilibria: an experimental study under oxidizing conditions. Contributions to Mineralogy and Petrology, 152, 611–638.

——— (2010) Effect of oxygen fugacity and water on phase equilibria of a hydrous tholeiitic basalt. Contributions to Mineralogy and Petrology, 160, 551–568.

Feldman, U. (1992) Elemental abundances in the upper solar atmosphere. Physica Scripta, 46, 202–220.

Filiberto, J. (2014) Magmatic diversity on Venus: Constraints from terrestrial analog crystallization experiments. Icarus, 231, 131–136.

Filiberto, J., Trang, D., Treiman, A.H., and Gilmore, M.S. (2020) Present-day volcanism on Venus as evidenced from weathering rates of olivine. Science Advances, 6, eaax7445.

Flaherty, T., Druitt, T.H., Tuffen, H., Higgins, M.D., Costa, F., and Cadoux, A. (2018) Multiple timescale constraints for high-flux magma chamber assembly prior to the Late Bronze Age eruption of Santorini (Greece). Contributions to Mineralogy and Petrology, 173.

Frost, B.R., and Lindsley, D.H. (1992) Equilibria among Fe-Ti oxides, pyroxenes, olivine, and quartz: Part II. Application. American Mineralogist, 77, 1004–1020.

Fulton, B.J., Petigura, E.A., Howard, A.W., Isaacson, H., Marcy, G.W., Cargile, P.A., Hebb, L., Weiss, L.M., Johnson, J.A., Morton, T.D., and others (2017) The California-Kepler Survey. III. A Gap in the Radius Distribution of Small Planets. The Astronomical Journal, 154, 109.

Gale, A., Dalton, C.A., Langmuir, C.H., Su, Y., and Schilling, J.-G. (2013) The mean composition of ocean ridge basalts: MEAN MORB. Geochemistry, Geophysics, Geosystems, 14, 489–518.

Gansecki, C. A. (1998) [40]Ar/[39]Ar geochronology and pre-eruptive geochemistry of the Yellowstone Plateau volcanic field rhyolites. Stanford University.

Gardner, J.E., Befus, K.S., Gualda, G.A.R., and Ghiorso, M.S. (2014) Experimental constraints on

rhyolite-MELTS and the Late Bishop Tuff magma body. Contributions to Mineralogy and Petrology, 168.

Gelman, S.E., Gutiérrez, F.J., and Bachmann, O. (2013) On the longevity of large upper crustal silicic magma reservoirs. Geology, 41, 759–762.

Ghiorso, M.S., and Evans, B.W. (2008) Thermodynamics of Rhombohedral Oxide Solid Solutions and a Revision of the FE-TI Two-Oxide Geothermometer and Oxygen-Barometer. American Journal of Science, 308, 957–1039.

Ghiorso, M.S., and Gualda, G.A.R. (2013) A method for estimating the activity of titania in magmatic liquids from the compositions of coexisting rhombohedral and cubic iron–titanium oxides. Contributions to Mineralogy and Petrology, 165, 73–81.

——— (2015) An H_2O–C_2 mixed fluid saturation model compatible with rhyolite-MELTS. Contributions to Mineralogy and Petrology, 169.

Ghiorso, M.S., and Sack, R.O. (1995) Chemical mass transfer in magmatic processes IV. A revised and internally consistent thermodynamic model for the interpolation and extrapolation of liquid-solid equilibria in magmatic systems at elevated temperatures and pressures. Contributions to Mineralogy and Petrology, 119, 197–212.

Ghiorso, M.S., Hirschmann, M.M., Reiners, P.W., and Kress, V.C. (2002) The pMELTS: A revision of MELTS for improved calculation of phase relations and major element partitioning related to partial melting of the mantle to 3 GPa: pMELTS, A REVISION OF MELTS. Geochemistry, Geophysics, Geosystems, 3, 1–35.

Girard, G., and Stix, J. (2009) Magma Recharge and Crystal Mush Rejuvenation Associated with Early Post-collapse Upper Basin Member Rhyolites, Yellowstone Caldera, Wyoming. Journal of Petrology, 50, 2095–2125.

——— (2010) Rapid extraction of discrete magma batches from a large differentiating magma chamber: the Central Plateau Member rhyolites, Yellowstone Caldera, Wyoming. Contributions to Mineralogy and Petrology, 160, 441–465.

——— (2012) Future volcanism at Yellowstone caldera: Insights from geochemistry of young volcanic units and monitoring of volcanic unrest. GSA Today, 4–10.

Gordeychik, B., Churikova, T., Kronz, A., Sundermeyer, C., Simakin, A., and Wörner, G. (2018) Growth of, and diffusion in, olivine in ultra-fast ascending basalt magmas from Shiveluch volcano. Scientific Reports, 8.

Greene, T.P., Line, M.R., Montero, C., Fortney, J.J., Lustig-Yaeger, J., and Luther, K. (2016) Characterizing Transiting Exoplanet Atmospheres with JWST. The Astrophysical Journal, 817, 17.

Grove, T.L., and Juster, T.C. (1989) Experimental investigations of low-Ca pyroxene stability and olivine-pyroxene-liquid equilibria at 1-atm in natural basaltic and andesitic liquids. Contributions to Mineralogy and Petrology, 103, 287–305.

Grove, T.L., and Krawczynski, M.J. (2009) Lunar Mare Volcanism: Where Did the Magmas Come From? Elements, 5, 29–34.

Grove, T.L., and Till, C.B. (2015) Melting the Earth's Upper Mantle. In Encyclopedia of Volcanos. Elsevier/AP, Amsterdam ; Boston.

Grove, T.L., Kinzler, R.J., and Bryan, W.B. (1992) Fractionation of Mid-Ocean Ridge Basalt (MORB). Geophysical Monograph, 71, 281–310.

Gualda, G.A.R., and Ghiorso, M.S. (2013) The Bishop Tuff giant magma body: an alternative to the Standard Model. Contributions to Mineralogy and Petrology, 166, 755–775.

——— (2015) MELTS_Excel: A Microsoft Excel-based MELTS interface for research and teaching of magma properties and evolution. Geochemistry, Geophysics, Geosystems, 16, 315–324.

Gualda, G.A.R., and Sutton, S.R. (2016) The Year Leading to a Supereruption. (A.K. Schmitt, Ed.) PLOS ONE, 11, e0159200.

Gualda, G.A.R., Ghiorso, M.S., Lemons, R.V., and Carley, T.L. (2012a) Rhyolite-MELTS: a Modified Calibration of MELTS Optimized for Silica-rich, Fluid-bearing Magmatic Systems. Journal of Petrology, 53, 875–890.

Gualda, G.A.R., Pamukcu, A.S., Ghiorso, M.S., Anderson, A.T., Sutton, S.R., and Rivers, M.L. (2012b) Timescales of Quartz Crystallization and the Longevity of the Bishop Giant Magma Body. (N. Houlie, Ed.) PLoS ONE, 7, e37492.

Hakim, K., Spaargaren, R., Grewal, D.S., Rohrbach, A., Berndt, J., Dominik, C., and van Westrenen, W. (2019) Mineralogy, Structure, and Habitability of Carbon-Enriched Rocky Exoplanets: A Laboratory Approach. Astrobiology, 19, 867–884.

Hart, S.R., and Zindler, A. (1986) In Search of a Bulk-Earth Composition. Chemical Geology, 57, 247–267.

Hartley, M.E., Morgan, D.J., Maclennan, J., Edmonds, M., and Thordarson, T. (2016) Tracking timescales of short-term precursors to large basaltic fissure eruptions through Fe–Mg diffusion in olivine. Earth and Planetary Science Letters, 439, 58–70.

Hays, J.F. (1966) Lime-Alumina-Silica, 234–239.

Hervig, R.L., and Dunbar, N.W. (1992) Cause of chemical zoning in the Bishop (California) and Bandelier (New Mexico) magma chambers. Earth and Planetary Science Letters, 111, 97–108.

Herzberg, C., Condie, K., and Korenaga, J. (2010) Thermal history of the Earth and its petrological expression. Earth and Planetary Science Letters, 292, 79–88.

Hess, K.-U., and Dingwell, D.D. (1996) Viscosities of hydrous leucogranitic melts: A non-Arrhenian model. American Mineralogist, 81, 1297–1300.

Hess, K.-U., Cordonnier, B., Lavallée, Y., and Dingwell, D.B. (2008) Viscous heating in rhyolite: An in situ experimental determination. Earth and Planetary Science Letters, 275, 121–126.

Hildreth, E.W. (1977) The magma chamber of the Bishop Tuff: Gradients in temperature, pressure, and composition. Ph.D. thesis, University of California, Berkeley.

Hildreth, W. (1981) Gradients in silicic magma chambers: Implications for lithospheric magmatism. Journal of Geophysical Research: Solid Earth, 86, 10153–10192.

——— (2004) Volcanological perspectives on Long Valley, Mammoth Mountain, and Mono Craters: several contiguous but discrete systems. Journal of Volcanology and Geothermal Research, 136, 169–198.

Hildreth, W., and Wilson, C.J.N. (2007) Compositional Zoning of the Bishop Tuff. Journal of Petrology, 48, 951–999.

Hildreth, W., Christiansen, R.L., and O'Neil, J.R. (1984) Catastrophic isotopic modification of rhyolitic magma at times of caldera subsidence, Yellowstone Plateau Volcanic Field. Journal of Geophysical Research: Solid Earth, 89, 8339–8369.

Hinkel, N.R., and Unterborn, C.T. (2018) The Star–Planet Connection. I. Using Stellar Composition to Observationally Constrain Planetary Mineralogy for the 10 Closest Stars. The Astrophysical Journal, 853, 83.

Hinkel, N.R., Timmes, F.X., Young, P.A., Pagano, M.D., and Turnbull, M.C. (2014) Stellar Abundances in the Solar Neighborhood: The Hypatia Catalog. The Astronomical Journal, 148, 54.

Hirschmann, M.M. (2000) Mantle solidus: Experimental constraints and the effects of peridotite composition. Geochemistry, Geophysics, Geosystems, 1.

Holzheid, A., and Grove, T.L. (2002) Sulfur saturation limits in silicate melts and their implications for core formation scenarios for terrestrial planets. American Mineralogist, 87, 227–237.

Horn, S., and Schmincke, H.-U. (2000) Volatile emission during the eruption of Baitoushan Volcano (China/North Korea) ca. 969 AD. Bulletin of Volcanology, 61, 0537–0555.

Horstwood, M.S.A., Košler, J., Gehrels, G., Jackson, S.E., McLean, N.M., Paton, C., Pearson, N.J., Sircombe, K., Sylvester, P., Vermeesch, P., and others (2016) Community-Derived Standards for LA-ICP-MS U-(Th-)Pb Geochronology - Uncertainty Propagation, Age Interpretation and Data Reporting. Geostandards and Geoanalytical Research, 40, 311–332.

Hu, R., Seager, S., and Bains, W. (2012) Photochemistry in Terrestrial Exoplanet Atmospheres. I. Photochemistry Model and Benchmark Cases. The Astrophysical Journal, 761, 166.

Huang, R., and Audétat, A. (2012) The titanium-in-quartz (TitaniQ) thermobarometer: A critical examination and re-calibration. Geochimica et Cosmochimica Acta, 84, 75–89.

Huebner, J.S. (1980) Pyroxene phase equilibria at low pressure. In C.T. Preweitt, Ed., Pyroxenes Vol. 7. Mineralogical Society of America.

Humphreys, M.C.S., Edmonds, M., and Klöcking, M.S. (2016) The validity of plagioclase-melt geothermometry for degassing-driven magma crystallization. American Mineralogist, 101, 769–779.

Iacovino, K., and Till, C. (2018) DensityX: A program for calculating the densities of hydrous magmatic liquids from 427–1,627 °C and up to 30 kbar. Volcanica, 2, 1–10.

Iacovino, K., Kim, J.S., Sisson, T.W., Lowenstern, J.B., Jang, J.N., Song, K.H., Ham, H.H., Ri, K.H., Donovan, A.R., Oppenheimer, C., and others (2015) New Constraints on the Geochemistry of the Millennium Eruption of Mount Paektu (Changbaishan), Democratic People's Republic of Korea/China. In 2015 AGU Fall Meeting. San Francisco, CA, USA.

Iacovino, K., Kim, J.-S., Sisson, T., Lowenstern, J., Ri, K.-H., Jang, J.-N., Song, K.-H., Ham, S.-H., Oppenheimer, C., Hammond, J.O.S., and others (2016) Quantifying gas emissions from the "Millennium Eruption" of Paektu volcano Democratic People's Republic of Korea/China. Science Advances, 2, 1–11.

Johnson, J.A., Petigura, E.A., Fulton, B.J., Marcy, G.W., Howard, A.W., Isaacson, H., Hebb, L., Cargile, P.A., Morton, T.D., Weiss, L.M., and others (2017) The California-Kepler Survey. II. Precise Physical Properties of 2025 Kepler Planets and Their Host Stars. The Astronomical Journal, 154, 108.

Juster, T.C., Grove, T.L., and Perfit, M.R. (1989) Experimental constraints on the generation of FeTi basalts, andesites, and rhyodacites at the Galapagos Spreading Center, 85°W and 95°W. Journal of Geophysical Research, 94, 9251.

Kane, S.R., Hill, M.L., Kasting, J.F., Kopparapu, R.K., Quintana, E.V., Barclay, T., Batalha, N.M., Borucki, W.J., Ciardi, D.R., Haghighipour, N., and others (2016) A Catalog of Kepler Habitable Zone Exoplanet Candidates. The Astrophysical Journal, 830, 1.

Kasting, J.F., Whitmire, D.P., and Reynolds, R.T. (1993) Habitable Zones around Main Sequence Stars. Icarus, 101, 108–128.

Keppler, H. (1999) Experimental Evidence for the Source of Excess Sulfur in Explosive Volcanic Eruptions. Science, 284, 1652–1654.

Kiefer, W.S., Filiberto, J., Sandu, C., and Li, Q. (2015) The effects of mantle composition on the peridotite solidus: Implications for the magmatic history of Mars. Geochimica et Cosmochimica Acta, 162, 247–258.

Kinzler, R.J., and Grove, T.L. (1992) Primary magmas of mid-ocean ridge basalts 1. Experiments and methods. Journal of Geophysical Research, 97, 6885.

Koll, D.D.B., Malik, M., Mansfield, M., Kempton, E.M.-R., Kite, E., Abbot, D., and Bean, J.L. (2019) Identifying Candidate Atmospheres on Rocky M dwarf Planets via Eclipse Photometry. arXiv:1907.13138 [astro-ph].

Kopparapu, R.K., Ramirez, R.M., SchottelKotte, J., Kasting, J.F., Domagal-Goldman, S., and Eymet, V. (2014) Habitable zones around main-sequence stars: dependence on planetary mass. The Astrophysical Journal, 787, L29.

Krawczynski, M.J., and Grove, T.L. (2012) Experimental investigation of the influence of oxygen fugacity on the source depths for high titanium lunar ultramafic magmas. Geochimica et Cosmochimica Acta, 79, 1–19.

Kreidberg, L. (2018) Exoplanet Atmosphere Measurements from Transmission Spectroscopy and Other Planet Star Combined Light Observations. In H. Deeg and J. Belmonte, Eds., Handbook of Exoplanets pp. 1–23. Springer, Cham.

Kreidberg, L., Koll, D.D.B., Morley, C., Hu, R., Schaefer, L., Deming, D., Stevenson, K.B., Dittmann, J., Vanderburg, A., Berardo, D., and others (2019) Absence of a thick atmosphere on the terrestrial exoplanet LHS 3844b. Nature, 573, 87–90.

Liang, Y., Sun, C., and Yao, L. (2013) A REE-in-two-pyroxene thermometer for mafic and ultramafic rocks. Geochimica et Cosmochimica Acta, 102, 246–260.

Lindsley, D.H. (1983) Pyroxene thermometry. American Mineralogist, 68, 477–493.

Lindsley, D.H., and Andersen, D.J. (1983) A two-pyroxene thermometer. Journal of Geophysical Research, 88, A887.

Loewen, M.W., and Bindeman, I.N. (2015) Oxygen isotope and trace element evidence for three-stage petrogenesis of the youngest episode (260–79 ka) of Yellowstone rhyolitic volcanism. Contributions to Mineralogy and Petrology, 170.

Lofgren, G.E., Huss, G.R., and Wasserburg, G.J. (2006) An experimental study of trace-element partitioning between Ti-Al-clinopyroxene and melt: Equilibrium and kinetic effects including sector zoning. American Mineralogist, 91, 1596–1606.

Longhi, J. (2005) Temporal stability and pressure calibration of barium carbonate and talc/pyrex pressure media in a piston-cylinder apparatus. American Mineralogist, 90, 206–218.

Lopes, R.M.C., Gregg, T.K.P., Harris, A., Radebaugh, J., Byrne, P., Kerber, L., and Mouginis-Mark, P. (2018) Extraterrestrial lava lakes. Journal of Volcanology and Geothermal Research, 366, 74–95.

Lustig-Yaeger, J., Meadows, V.S., and Lincowski, A.P. (2019) The Detectability and Characterization of the TRAPPIST-1 Exoplanet Atmospheres with JWST. The Astronomical Journal, 158, 27.

Lynn, K.J., Garcia, M.O., Shea, T., Costa, F., and Swanson, D.A. (2017) Timescales of mixing and storage for Keanakākoʻi Tephra magmas (1500–1820 C.E.), Kīlauea Volcano, Hawaiʻi. Contributions to Mineralogy and Petrology, 172.

Mahood, G., and Hildreth, W. (1983) Large partition coefficients for trace elements in high-silica rhyolites. Geochimica et Cosmochimica Acta, 47, 11–30.

Mansfield, M., Kite, E.S., Hu, R., Koll, D.D.B., Malik, M., Bean, J.L., and Kempton, E.M.-R. (2019) Identifying Atmospheres on Rocky Exoplanets Through Inferred High Albedo. arXiv:1907.13150 [astro-ph].

Martin, V.M., Morgan, D.J., Jerram, D.A., Caddick, M.J., Prior, D.J., and Davidson, J.P. (2008) Bang! Month-Scale Eruption Triggering at Santorini Volcano. Science, 321, 1178–1178.

Martinez, C.F., Cunha, K., Ghezzi, L., and Smith, V.V. (2019) A Spectroscopic Analysis of the California-Kepler Survey Sample. I. Stellar Parameters, Planetary Radii, and a Slope in the Radius Gap. The Astrophysical Journal, 875, 29.

Masotta, M., Mollo, S., Freda, C., Gaeta, M., and Moore, G. (2013) Clinopyroxene–liquid thermometers and barometers specific to alkaline differentiated magmas. Contributions to Mineralogy and Petrology, 166, 1545–1561.

Matthews, N.E., Vazquez, J.A., and Calvert, A.T. (2015) Age of the Lava Creek supereruption and magma chamber assembly from combined $^{40}Ar/^{39}Ar$ and U-Pb dating of sanidine and zircon crystals. Geochemistry, Geophysics, Geosystems, 16, 2508–2528.

Médard, E., and Grove, T.L. (2006) Early hydrous melting and degassing of the Martian interior. Journal of Geophysical Research, 111.

Milman-Barris, M.S., Beckett, J.R., Baker, M.B., Hofmann, A.E., Morgan, Z., Crowley, M.R., Vielzeuf, D., and Stolper, E. (2008) Zoning of phosphorus in igneous olivine. Contributions to Mineralogy and Petrology, 155, 739–765.

Mollo, S., and Hammer, J.E. (2017) Dynamic crystallization in magmas. In W. Heinrich and R. Abart, Eds., Mineral reaction kinetics: Microstructures, textures, chemical and isotopic signatures Vol. 16, pp. 378–418. Mineralogical Society of Great Britain & Ireland.

Mollo, S., Del Gaudio, P., Ventura, G., Iezzi, G., and Scarlato, P. (2010) Dependence of clinopyroxene composition on cooling rate in basaltic magmas: Implications for thermobarometry. Lithos, 118, 302–312.

Morgado, E., Morgan, D.J., Castruccio, A., Ebmeier, S.K., Parada, M.-Á., Brahm, R., Harvey, J., Gutiérrez, F., and Walshaw, R. (2019) Old magma and a new, intrusive trigger: using diffusion chronometry to understand the rapid-onset Calbuco eruption, April 2015 (Southern Chile). Contributions to Mineralogy and Petrology, 174.

Morgan, D.J., and Blake, S. (2006) Magmatic residence times of zoned phenocrysts: introduction and application of the binary element diffusion modelling (BEDM) technique. Contributions to Mineralogy and Petrology, 151, 58–70.

Morgan, D.J., Blake, S., Rogers, N.W., DeVivo, B., Rolandi, G., Macdonald, R., and Hawkesworth, C.J. (2004) Time scales of crystal residence and magma chamber volume from modelling of diffusion profiles in phenocrysts: Vesuvius 1944. Earth and Planetary Science Letters, 222, 933–946.

Morgan, D.J., Blake, S., Rogers, N.W., De Vivo, B., Rolandi, G., and Davidson, J.P. (2006) Magma

chamber recharge at Vesuvius in the century prior to the eruption of AD 79. Geology, 34, 845–848.

Müller, T., Dohmen, R., Becker, H.W., ter Heege, J.H., and Chakraborty, S. (2013) Fe–Mg interdiffusion rates in clinopyroxene: experimental data and implications for Fe–Mg exchange geothermometers. Contributions to Mineralogy and Petrology, 166, 1563–1576.

Mutch, E.J.F., Maclennan, J., Shorttle, O., Edmonds, M., and Rudge, J.F. (2019) Rapid transcrustal magma movement under Iceland. Nature Geoscience.

Myers, M.L., Wallace, P.J., Wilson, C.J.N., Morter, B.K., and Swallow, E.J. (2016) Prolonged ascent and episodic venting of discrete magma batches at the onset of the Huckleberry Ridge supereruption, Yellowstone. Earth and Planetary Science Letters, 451, 285–297.

Namur, O., Collinet, M., Charlier, B., Grove, T.L., Holtz, F., and McCammon, C. (2016) Melting processes and mantle sources of lavas on Mercury. Earth and Planetary Science Letters, 439, 117–128.

Nisr, C., Meng, Y., MacDowell, A.A., Yan, J., Prakapenka, V., and Shim, S.-H. (2017) Thermal Expansion of SiC at High Pressure–Temperature and Implications for Thermal Convection in the Deep Interiors of Carbide Exoplanets. Journal of Geophysical Research: Planets, 122, 124–133.

Ochs, F.A.I., and Lange, R.A. (1999) The density of hydrous magmatic liquids. Science, 283, 1314–1317.

O'Neill, H.S.C., and Mavrogenes, J.A. (2002) The Sulfide Capacity and the Sulfur Content at Sulfide Saturation of Silicate Melts at 1400°C and 1 bar, 43, 39.

Oppenheimer, C., Scaillet, B., and Martin, R.S. (2011) Sulfur Degassing From Volcanoes: Source Conditions, Surveillance, Plume Chemistry and Earth System Impacts. Reviews in Mineralogy and Geochemistry, 73, 363–421.

Orlando, A., D'Orazio, M., Armienti, P., and Borrini, D. (2008) Experimental determination of plagioclase and clinopyroxene crystal growth rates in an anhydrous trachybasalt from Mt Etna (Italy). European Journal of Mineralogy, 20, 653–664.

Owen, J.E., and Wu, Y. (2013) Kepler Planets: A Tale of Photoevaporation. The Astrophysical Journal, 775, 105.

Pamukcu, A.S., Gualda, G.A.R., and Anderson, A.T. (2012) Crystallization Stages of the Bishop Tuff Magma Body Recorded in Crystal Textures in Pumice Clasts. Journal of Petrology, 53, 589–609.

Pamukcu, A.S., Ghiorso, M.S., and Gualda, G.A.R. (2016) High-Ti, bright-CL rims in volcanic quartz: a result of very rapid growth. Contributions to Mineralogy and Petrology, 171.

Papale, P., Moretti, R., and Barbato, D. (2006) The compositional dependence of the saturation surface of H_2O+CO_2 fluids in silicate melts. Chemical Geology, 229, 78–95.

Petigura, E.A., Howard, A.W., Marcy, G.W., Johnson, J.A., Isaacson, H., Cargile, P.A., Hebb, L., Fulton, B.J., Weiss, L.M., Morton, T.D., and others (2017) The California-Kepler Survey. I. High-resolution Spectroscopy of 1305 Stars Hosting Kepler Transiting Planets. The Astronomical Journal, 154, 107.

Pistone, M., Blundy, J., and Brooker, R.A. (2017) Water transfer during magma mixing events: Insights into crystal mush rejuvenation and melt extraction processes. American Mineralogist, 102, 766–776.

Pritchard, C.J., and Larson, P.B. (2012) Genesis of the post-caldera eastern Upper Basin Member rhyolites, Yellowstone, WY: from volcanic stratigraphy, geochemistry, and radiogenic isotope modeling. Contributions to Mineralogy and Petrology, 164, 205–228.

Putirka, K. (2016) Rates and styles of planetary cooling on Earth, Moon, Mars, and Vesta, using new models for oxygen fugacity, ferric-ferrous ratios, olivine-liquid Fe-Mg exchange, and mantle potential temperature. American Mineralogist, 101, 819–840.

Putirka, K., Johnson, M., Kinzler, R., Longhi, J., and Walker, D. (1996) Thermobarometry of mafic igneous rocks based on clinopyroxene-liquid equilibria, 0–30 kbar. Contributions to Mineralogy and Petrology, 123, 92–108.

Putirka, K.D. (2005) Mantle potential temperatures at Hawaii, Iceland, and the mid-ocean ridge system, as inferred from olivine phenocrysts: Evidence for thermally driven mantle plumes. Geochemistry, Geophysics, Geosystems, 6.

——— (2008) Thermometers and Barometers for Volcanic Systems. Minerals, Inclusions and Volcanic Processes, 69, 61–120.

Putirka, K.D., Mikaelian, H., Ryerson, F., and Shaw, H. (2003) New clinopyroxene-liquid thermobarometers for mafic, evolved, and volatile-bearing lava compositions, with applications to lavas from Tibet and the Snake River Plain, Idaho. American Mineralogist, 88, 1542–1554.

Reid, M.R., and Vazquez, J.A. (2017) Fitful and protracted magma assembly leading to a giant eruption, Youngest Toba Tuff, Indonesia. Geochemistry, Geophysics, Geosystems, 18, 156–177.

Reid, M.R., Vazquez, J.A., and Schmitt, A.K. (2011) Zircon-scale insights into the history of a Supervolcano, Bishop Tuff, Long Valley, California, with implications for the Ti-in-zircon geothermometer. Contributions to Mineralogy and Petrology, 161, 293–311.

Rivera, T.A., Schmitz, M.D., Crowley, J.L., and Storey, M. (2014) Rapid magma evolution constrained by zircon petrochronology and $^{40}Ar/^{39}Ar$ sanidine ages for the Huckleberry Ridge Tuff, Yellowstone, USA. Geology, 42, 643–646.

Rivera, T.A., Schmitz, M.D., Jicha, B.R., and Crowley, J.L. (2016) Zircon Petrochronology and $^{40}Ar/^{39}Ar$ Sanidine Dates for the Mesa Falls Tuff: Crystal-scale Records of Magmatic Evolution and the Short Lifespan of a Large Yellowstone Magma Chamber. Journal of Petrology, 57, 1677–1704.

Robock, A. (2000) Volcanic eruptions and climate. Reviews of Geophysics, 38, 191–219.

Rubin, A., Cooper, K.M., Leever, M., Wimpenny, J., Deering, C., Rooney, T., Gravley, D., and Yin, Q. (2016) Changes in magma storage conditions following caldera collapse at Okataina Volcanic Center, New Zealand. Contributions to Mineralogy and Petrology, 171.

Rubin, A., Cooper, K.M., Till, C.B., Kent, A.J.R., Costa, F., Gravley, D., Deering, C., and Cole, J. (2017) Rapid cooling and cold storage in a silicic magma reservoir recorded in individual crystals. Science, 356.

Sack, R.O., and Ghiorso, M.S. (1994) Thermodynamics of multicomponent pyroxenes: II. Phase relations in the quadrilateral. Contributions to Mineralogy and Petrology, 116, 287–300.

Salviulo, G., Secco, L., Marzoli, A., Piccirillo, E.M., and Nyobe, J.B. (2000) Ca-rich pyroxene from basic and silicic volcanic rocks from the Cameroon Volcanic Line (West-Africa): crystal chemistry and petrological relationships. Mineralogy and Petrology, 70, 73–88.

Sambridge, M. (1999) Geophysical inversion with a neighbourhood algorithm - II. Appraising the ensemble. Geophysical Journal International, 138, 727–746.

Santos, A.R., Agee, C.B., McCubbin, F.M., Shearer, C.K., Burger, P.V., Tartèse, R., and Anand, M. (2015) Petrology of igneous clasts in Northwest Africa 7034: Implications for the petrologic diversity of the martian crust. Geochimica et Cosmochimica Acta, 157, 56–85.

Saunders, K., Blundy, J., Dohmen, R., and Cashman, K. (2012) Linking Petrology and Seismology at an Active Volcano. Science, 336, 1023–1027.

Schwieterman, E.W., Kiang, N.Y., Parenteau, M.N., Harman, C.E., DasSarma, S., Fisher, T.M., Arney, G.N., Hartnett, H.E., Reinhard, C.T., Olson, S.L., and others (2018) Exoplanet Biosignatures: A Review of Remotely Detectable Signs of Life. Astrobiology, 18, 663–708.

Shaffer, J.S., and Till, C.B. (2016) New Temperature and H_2O Estimates for Post Caldera Yellowstone Rhyolite Lavas using Feldspar Geothermometry and Rhyolite-MELTS. In 2016 AGU Fall Meeting. San Francisco, CA, USA.

Shamloo, H.I., and Till, C.B. (2017) Petrologic Insights into the Timing and Triggering Mechanism of the Lava Creek Tuff Supereruption, Yellowstone Caldera, WY, USA. In 2017 IAVCEI Scientific Assembly p. 995. Presented at the IAVCEI, Portland, OR.

——— (2019) Decadal transition from quiescence to supereruption: petrologic investigation of the Lava Creek Tuff, Yellowstone Caldera, WY. Contributions to Mineralogy and Petrology, 174.

Shea, T., Lynn, K.J., and Garcia, M.O. (2015) Cracking the olivine zoning code: Distinguishing between crystal growth and diffusion. Geology, 43, 935–938.

Simakin, A.G., and Bindeman, I.N. (2012) Remelting in caldera and rift environments and the genesis of hot, "recycled" rhyolites. Earth and Planetary Science Letters, 337–338, 224–235.

Singer, B.S., Costa, F., Herrin, J.S., Hildreth, W., and Fierstein, J. (2016) The timing of compositionally-zoned magma reservoirs and mafic 'priming' weeks before the 1912 Novarupta-Katmai rhyolite eruption. Earth and Planetary Science Letters, 451, 125–137.

Sisson, T.W. (1991) Pyroxene-high silica rhyolite trace element partition coefficients measured by ion microprobe. Geochimica et Cosmochimica Acta, 55, 1575–1585.

Smrekar, S.E., Stofan, E.R., Mueller, N., Treiman, A., Elkins-Tanton, L., Helbert, J., Piccioni, G., and Drossart, P. (2010) Recent Hotspot Volcanism on Venus from VIRTIS Emissivity Data. Science, 328, 605–608.

Squyres, S.W., Aharonson, O., Clark, B.C., Cohen, B.A., Crumpler, L., de Souza, P.A., Farrand, W.H., Gellert, R., Grant, J., Grotzinger, J.P., and others (2007) Pyroclastic Activity at Home Plate in Gusev Crater, Mars. Science, 316, 738–742.

Stelten, M.E., Cooper, K.M., Vazquez, J.A., Calvert, A.T., and Glessner, J.J.G. (2015) Mechanisms and Timescales of Generating Eruptible Rhyolitic Magmas at Yellowstone Caldera from Zircon and Sanidine Geochronology and Geochemistry. Journal of Petrology, 56, 1607–1642.

Stelten, M.E., Cooper, K.M., Wimpenny, J.B., Vazquez, J.A., and Yin, Q.-Z. (2017) The role of mantle-derived magmas in the isotopic evolution of Yellowstone's magmatic system. Geochemistry, Geophysics, Geosystems, 18, 1350–1365.

Stelten, M.E., Champion, D.E., and Kuntz, M.A. (2018) The timing and origin of pre- and post-caldera volcanism associated with the Mesa Falls Tuff, Yellowstone Plateau volcanic field. Journal of Volcanology and Geothermal Research, 350, 47–60.

Stixrude, L., and Lithgow-Bertelloni, C. (2005) Thermodynamics of mantle minerals - I. Physical properties. Geophysical Journal International, 162, 610–632.

Stock, M.J., Humphreys, M.C.S., Smith, V.C., Isaia, R., and Pyle, D.M. (2016) Late-stage volatile saturation as a potential trigger for explosive volcanic eruptions. Nature Geoscience, 9, 249–254.

Streck, M.J. (1994) Volcanology and Petrology of the Rattlesnake Ash-Flow Tuff, Eastern Oregon. Oregon State University.

Sundermeyer, C., Di Muro, A., Gordeychik, B., and Wörner, G. (2020) Timescales of magmatic processes during the eruptive cycle 2014–2015 at Piton de la Fournaise, La Réunion, obtained from Mg–Fe diffusion modelling in olivine. Contributions to Mineralogy and Petrology, 175.

Swallow, E.J., Wilson, C.J.N., Myers, M.L., Wallace, P.J., Collins, K.S., and Smith, E.G.C. (2018) Evacuation of multiple magma bodies and the onset of caldera collapse in a supereruption, captured in glass and mineral compositions. Contributions to Mineralogy and Petrology, 173.

Swanson, S.E. (1977) Relation of nucleation and crystal-growth rate to the development of granitic textures. American Mineralogist, 62, 966–978.

Till, C.B. (2017) An Integrated Approach for Identifying P-T-X-t Histories and Eruption Triggers for

Silicic Magmas; An Example Examining the Scaup Lake Rhyolite Yellowstone Caldera, WY. In 2017 Scientific Assembly. Presented at the IAVCEI, Portland, OR.

Till, C.B., Grove, T.L., and Krawczynski, M.J. (2012) A melting model for variably depleted and enriched lherzolite in the plagioclase and spinel stability fields. Journal of Geophysical Research: Solid Earth, 117.

Till, C.B., Vazquez, J.A., and Boyce, J.W. (2015) Months between rejuvenation and volcanic eruption at Yellowstone caldera, Wyoming. Geology, 43, 695–698.

Till, C.B., Vazquez, J.A., Stelten, M.E., Shamloo, H.I., and Shaffer, J.S. (2019) Coexisting Discrete Bodies of Rhyolite and Punctuated Volcanism Characterize Yellowstone's Post☐Lava Creek Tuff Caldera Evolution. Geochemistry, Geophysics, Geosystems, 20, 3861–3881.

Treiman, A.H. (2007) Geochemistry of Venus' Surface: Current limitations as future opportunities. In L.W. Esposito, E.R. Stofan, and T.E. Cravens, Eds., Geophysical Monograph Series Vol. 176, pp. 7–22. American Geophysical Union, Washington, D.C.

Unterborn, C.T., and Panero, W.R. (2019) The Pressure and Temperature Limits of Likely Rocky Exoplanets. Journal of Geophysical Research: Planets, 124, 1704–1716.

Van Orman, J.A., Grove, T.L., and Shimizu, N. (2001) Rare earth element diffusion in diopside: influence of temperature, pressure, and ionic radius, and an elastic model for diffusion in silicates. Contributions to Mineralogy and Petrology, 141, 687–703.

Vander Kaaden, K.E., McCubbin, F.M., Nittler, L.R., Peplowski, P.N., Weider, S.Z., Frank, E.A., and McCoy, T.J. (2017) Geochemistry, mineralogy, and petrology of boninitic and komatiitic rocks on the mercurian surface: Insights into the mercurian mantle. Icarus, 285, 155–168.

Vazquez, J.A., Kyriazis, S.F., Reid, M.R., Sehler, R.C., and Ramos, F.C. (2009) Thermochemical evolution of young rhyolites at Yellowstone: Evidence for a cooling but periodically replenished postcaldera magma reservoir. Journal of Volcanology and Geothermal Research, 188, 186–196.

Wadhwa, M. (2008) Redox Conditions on Small Bodies, the Moon and Mars. Reviews in Mineralogy and Geochemistry, 68, 493–510.

Wark, D.A., and Watson, E.B. (2006) TitaniQ: a titanium-in-quartz geothermometer. Contributions to Mineralogy and Petrology, 152, 743–754.

Wark, D.A., Hildreth, W., Watson, E.B., and Cherniak, D.J. (2004) Origin of Thermal and Compositional Zoning in the Bishop Magma Reservoir: Insights from Zoned Quartz Phenocrysts p. 3. Presented at the 2004 AGU Fall Meeting, San Francisco, CA, USA.

Wark, D.A., Hildreth, W., Spear, F.S., Cherniak, D.J., and Watson, E.B. (2007) Pre-eruption recharge of the Bishop magma system. Geology, 35, 235.

Warshaw, C.M., and Smith, R.L. (1988) Pyroxenes and fayalites in the Bandelier Tuff, New Mexico: temperatures and comparison with other rhyolites. American Mineralogist, 73, 1025–1037.

Watson, E., Wark, D., Price, J., and Van Orman, J. (2002) Mapping the thermal structure of solid-media pressure assemblies. Contributions to Mineralogy and Petrology, 142, 640–652.

Watts, K.E., Bindeman, I.N., and Schmitt, A.K. (2012) Crystal scale anatomy of a dying supervolcano: an isotope and geochronology study of individual phenocrysts from voluminous rhyolites of the Yellowstone caldera. Contributions to Mineralogy and Petrology, 164, 45–67.

Webster, J.D., Goldoff, B., Sintoni, M.F., Shimizu, N., and De Vivo, B. (2014) C-O-H-Cl-S-F Volatile Solubilities, Partitioning, and Mixing in Phonolitic-Trachytic Melts and Aqueous-Carbonic Vapor Saline Liquid at 200 MPa. Journal of Petrology, 55, 2217–2248.

Weiss, L.M., Marcy, G.W., Petigura, E.A., Fulton, B.J., Howard, A.W., Winn, J.N., Isaacson, H.T., Morton, T.D., Hirsch, L.A., Sinukoff, E.J., and others (2018) The California-Kepler Survey. V. Peas in a Pod: Planets in a Kepler Multi-planet System Are Similar in Size and Regularly Spaced. The Astronomical Journal, 155, 48.

Wen, S., and Nekvasil, H. (1994) SOLVALC: An interactive graphics program package for calculating the ternary feldspar solvus and for two-feldspar geothermometry. Computers & Geosciences, 20, 1025–1040.

Wilcock, J., Goff, F., Minarik, W.G., and Stix, J. (2013) Magmatic Recharge during the Formation and Resurgence of the Valles Caldera, New Mexico, USA: Evidence from Quartz Compositional Zoning and Geothermometry. Journal of Petrology, 54, 635–664.

Wilson, C.J.N., and Hildreth, W. (1997) The Bishop Tuff: New Insights From Eruptive Stratigraphy. The Journal of Geology, 105, 407–440.

Wolszczan, A., and Frail, D. (1992) A planetary system around the millisecond pulsar PSR1257 + 12. Nature, 355, 145–147.

Wotzlaw, J.-F., Bindeman, I.N., Stern, R.A., D'Abzac, F.-X., and Schaltegger, U. (2015) Rapid heterogeneous assembly of multiple magma reservoirs prior to Yellowstone supereruptions. Scientific Reports, 5, 14026.

Wykes, J.L., O'Neill, H.St.C., and Mavrogenes, J.A. (2015) The Effect of FeO on the Sulfur Content at Sulfide Saturation (SCSS) and the Selenium Content at Selenide Saturation of Silicate Melts. Journal of Petrology, 56, 1407–1424.

Yao, L., and Liang, Y. (2012) An experimental study of the solidus of a hybrid lunar cumulate mantle: implications for the temperature at the core-mantle boundary of the moon. Presented at the Lunar and Planetary Science Conference, Woodlands, TX.

Young, P.A., Desch, S.J., Anbar, A.D., Barnes, R., Hinkel, N.R., Kopparapu, R., Madhusudhan, N., Monga, N., Pagano, M.D., Riner, M.A., and others (2014) Astrobiological Stoichiometry. Astrobiology, 14, 603–626.

Zhang, Y. (2008) Geochemical Kinetics, 631 p. Princeton University Press, Princeton, New Jersey.

APPENDIX A

SUPPLEMENTARY MATERIAL FOR CHAPTER 2

Table A.1: Clinopyroxene and liquid component calculation procedure

Clinopyroxene	
Step	Formula
1. Normalize oxides to 100 wt%	
2. Convert oxides to mole proportions	oxide/oxide molecular mass
3. Calculate number of oxygens	mole proportion * #oxygens in oxide
4. Sum number of oxygens	
5. Calculate oxygen renormalization factor (ORF)	6/sum
6. Calculate cations on basis of 6 oxygens (CBO)	mole proportion * ORF * #cations in oxide

All following calculations for clinopyroxene use CBO values for stated elements

7. Calculate CBO for Al^{IV} and Al^{VI}		
a. CBO for Al^{IV} (tetrahedral)	2 - Si	
b. CBO for Al^{VI} (octahedral)	If $Al^{tot} - Al^{IV} < 0$: 0	
	If $Al^{tot} - Al^{IV} \geq 0$: $Al^{tot} - Al^{IV}$	
8. Calculate components		
a. Jd ($NaAlSi_2O_6$)	If Na < Al^{VI} : Na; If Na $\geq Al^{VI}$: Al^{VI}	
b. CaTs (Ca Tschermak's pyroxene)	If Al^{VI} > Na : Al^{VI} - Na	
	If $Al^{VI} \leq$ Na : 0	
c. CaTi ($CaTiAl_2O_6$)	If Al^{IV} > CaTs : (Al^{IV} - CaTs)/2	
	If $Al^{IV} \leq$ CaTs : 0	
d. CrCaTs ($CaCr_2SiO_6$)	Cr/2	
e. $DiHd_{1996}$	If Ca - CaTi - CaTs - CrCaTs > 0 : Ca - CaTi - CaTs - CrCaTs	
	If Ca - CaTi - CaTs - CrCaTs $\leq$ 0 : 0	
f. $DiHd_{2003}$	Ca - CaTi - CaTs - CrCaTs	
g. EnFs	[(Fe + Mg) - $DiHd_{1996}$)]/2	
9. Calculate a(cpx-En)	$(1 - Ca - Na - K) * [1 - 0.5 * (Al^{tot} + Na + K + Cr)]$	

Liquid	
Step	Formula
1. Normalize oxides to 100 wt%	
2. Convert oxides to cation proportions	oxide * #cations in oxide/oxide molecular mass
3. Sum cation proportions	
4. Calculate cation fractions (CF)	cation proportion/sum
5. Calculate $Mg\#^{liq}$	$CF_{MgO}/(CF_{MgO} + CF_{FeO})$

Based on Putirka (2003) and references therein. Parameter Group A: clinopyroxene step 8, liquid steps 4–5. Parameter Group B: Group A, clinopyroxene steps 6–7, 9

Table A.2: Calibration Dataset: Experimental Products

Experiment	Reference	Locality	Experimental Conditions			Phase assemblage
			T [°C]	P [Mpa]	t [hrs]	
BJR-50	Almeev et al., 2012	Cougar Point Tuff	975	204	240	Gl, Aug, Mt
BJR-55	Almeev et al., 2012	Cougar Point Tuff	950	204	336	Gl, Aug, Pig, Fsp, Qtz, Fa
BJR-57	Almeev et al., 2012	Cougar Point Tuff	950	204	336	Gl, Aug, Fsp, Mt
BJR-60	Almeev et al., 2012	Cougar Point Tuff	925	200	504	Gl, Aug, Fsp, Qtz, Mt
BJR-59	Almeev et al., 2012	Cougar Point Tuff	925	200	504	Gl, Aug, Fsp, Qtz, Mt
BJR-58	Almeev et al., 2012	Cougar Point Tuff	925	200	504	Gl, Aug, Mt
BJR-72	Almeev et al., 2012	Cougar Point Tuff	900	200	168	Gl, Aug, Pig, Fsp, Qtz, Mt, Fa
BJR-62	Almeev et al., 2012	Cougar Point Tuff	875	200	504	Gl, Aug, Pig, Fsp, Qtz, Fa
BJR-64	Almeev et al., 2012	Cougar Point Tuff	875	200	504	Gl, Aug, Fsp, Qtz, Mt
BJR-66	Almeev et al., 2012	Cougar Point Tuff	875	200	504	Gl, Aug, Fsp, Mt
BJR-71	Almeev et al., 2012	Cougar Point Tuff	825	200	624	Gl, Aug, Fsp, Qtz, Mt
BJR-69	Almeev et al., 2012	Cougar Point Tuff	825	200	624	Gl, Aug, Fsp, Qtz, Mt
IBR2-29	Almeev et al., 2012	Indian Batt rhyolite	1000	200	168	Gl, Aug, Pig, Pl
IBR2-31	Almeev et al., 2012	Indian Batt rhyolite	1000	200	168	Gl, Aug, Pig, Pl, Mt
IBR2-53	Almeev et al., 2012	Indian Batt rhyolite	975	204	240	Gl, Aug, Pig, Pl, Mt
IBR2-10	Almeev et al., 2012	Indian Batt rhyolite	950	204	336	Gl, Aug, Pig, Pl?, Fsp, Qtz, Mt
IBR2-12	Almeev et al., 2012	Indian Batt rhyolite	950	204	336	Gl, Aug, Pl, Mt
IBR2-18	Almeev et al., 2012	Indian Batt rhyolite	925	200	504	Gl, Aug, Pig, Pl, Fsp, Qtz, Mt
IBR2-15	Almeev et al., 2012	Indian Batt rhyolite	925	200	504	Gl, Aug, Pl, Fsp, Qtz, Mt?
IBR2-17	Almeev et al., 2012	Indian Batt rhyolite	925	200	504	Gl, Aug, Mt
IBR2-25	Almeev et al., 2012	Indian Batt rhyolite	900	204	168	Gl, Aug, Pl?, Fsp, Qtz, Mt?
IBR2-27	Almeev et al., 2012	Indian Batt rhyolite	900	204	168	Gl, Aug, Pl, Mt
IBR2-24	Almeev et al., 2012	Indian Batt rhyolite	900	204	168	Gl, Aug, Pl, Mt
IBR2-26	Almeev et al., 2012	Indian Batt rhyolite	900	204	168	Gl, Aug, Mt
IBR2-20	Almeev et al., 2012	Indian Batt rhyolite	875	200	504	Gl, Aug, Pl?, Fsp, Qtz, Mt
IBR2-21	Almeev et al., 2012	Indian Batt rhyolite	875	200	504	Gl, Aug, Pl?, Fsp, Qtz, Mt
IBR2-48	Almeev et al., 2012	Indian Batt rhyolite	1025	200	284	Gl, Aug
IBR2-53r	Almeev et al., 2012	Indian Batt rhyolite	975	204	288	Gl, Aug, Mt
IBR2-14	Almeev et al., 2012	Indian Batt rhyolite	930	207	163	Gl, Aug, Pig?, Pl, Fsp, Qtz, Mt
IBR2-35	Almeev et al., 2012	Indian Batt rhyolite	930	207	163	Gl, Aug, Pl, Mt

Experiment	Reference	Locality	Experimental Conditions			Phase assemblage
			T [°C]	P [Mpa]	t [hrs]	
IBR2-59	Almeev et al., 2012	Indian Batt rhyolite	1025	501	163	Gl, Aug, Pig
IBR2-60	Almeev et al., 2012	Indian Batt rhyolite	1025	501	163	Gl, Aug
IBR2-63	Almeev et al., 2012	Indian Batt rhyolite	1000	503	161	Gl, Aug
IBR2-64	Almeev et al., 2012	Indian Batt rhyolite	1000	503	161	Gl, Aug, Pig
IBR2-67	Almeev et al., 2012	Indian Batt rhyolite	975	499	235	Gl, Aug, Ilm
IBR2-69	Almeev et al., 2012	Indian Batt rhyolite	975	499	235	Gl, Aug
M12	Bolte et al., 2015	Blacktail Creek Tuff	850	200	672	Gl, Aug, Pl, Tm
JI 63	Bolte et al., 2015	Blacktail Creek Tuff	815	200	336	Gl, Aug, Tm
JI 53	Bolte et al., 2015	Blacktail Creek Tuff	790	200	336	Gl, Aug, Bt, Pl, Tm
JII 34	Bolte et al., 2015	Blacktail Creek Tuff	790	200	672	Gl, Aug, Pl, Tm
G-1189	Gardner et al., 2014	Late-erupted Bishop Tuff	800	100	118	Gl, Aug
G-1190	Gardner et al., 2014	Late-erupted Bishop Tuff	775	100	115	Gl, Aug, Mt
G-1194	Gardner et al., 2014	Late-erupted Bishop Tuff	760	175	185	Gl, Aug, Bt
G-1197	Gardner et al., 2014	Late-erupted Bishop Tuff	740	100	362	Gl, Aug, Sa, Mt
G-1202	Gardner et al., 2014	Late-erupted Bishop Tuff	740	175	337	Gl, Aug, Bt
G-1203	Gardner et al., 2014	Late-erupted Bishop Tuff	720	175	337	Gl, Aug, Sa, Ilm, Bt
G-1206	Gardner et al., 2014	Late-erupted Bishop Tuff	750	100	362	Gl, Aug, Sa, Ox
G-1219	Gardner et al., 2014	Late-erupted Bishop Tuff	720	100	621	Gl, Aug, Sa, Qtz, Pg, Ilm, Mt
G-1225	Gardner et al., 2014	Late-erupted Bishop Tuff	700	150	501	Gl, Aug, Sa, Pl, Qtz, Ox
G-1230	Gardner et al., 2014	Late-erupted Bishop Tuff	700	200	351	Gl, Aug, Sa, Bt, Mt, Ilm
CS-1	Iacovino et al., 2015	Paektu Millenium	725	75	504	Gl, Aug, Fsp, Mt, Ch, Zir, Po
CS-7	Iacovino et al., 2015	Paektu Millenium	675	150	744	???
CS-8	Iacovino et al., 2015	Paektu Millenium	700	150	744	Gl, Mt, Aug, Ap, Fl, Po, Ch
CS-11	Iacovino et al., 2015	Paektu Millenium	675	125	744	Gl, Aug, Fsp, Qtz, Mt, Amp, Ilm, Po, Ch, Zir
CS-16	Iacovino et al., 2015	Paektu Millenium	700	100	768	Gl, Aug, Fsp, Mt, Ch, Zir
CS-26	Iacovino et al., 2015	Paektu Millenium	700	100	696	Gl, Aug, Fsp, Co, Qtz, Ch
CS-28	Iacovino et al., 2015	Paektu Millenium	700	150	696	Gl, Aug, Co, Mt
CS-32	Iacovino et al., 2015	Paektu Millenium	725	50	792	Gl, Aug, Fsp, Qtz, Mt
CS-40	Iacovino et al., 2015	Paektu Millenium	725	100	624	Gl, Aug, Fsp, Amp, Mt, Ch
CS-44	Iacovino et al., 2015	Paektu Millenium	750	50	720	Gl, Aug, Fsp, Qtz, Mt
SCL01-1	this work	Scaup Lake, Yellowstone	825	100	573	Gl, Aug, Ox, Amp, Qtz
SCL01-3	this work	Scaup Lake, Yellowstone	775	100	572	Gl, Aug, Amp, Qtz
SCL01-4	this work	Scaup Lake, Yellowstone	750	100	385	Gl, Aug, Fsp, Amp, Plag
SCL01-5	this work	Scaup Lake, Yellowstone	800	100	410	Gl, Aug, Amp

Gl = glass, Aug = augite, Mt = , Pig = pigeonite, Fsp = k-feldspar, Qtz = quartz, Pl = plagioclase, Sa = sanidine, Amp = amphibole, Bt = biotite, Fa = fayalite, Ch = chevkenite, Zir = zircon, Ap = apatite, Fl = fluorite, Po = pyrrhotite, Mt = magnetite, Ilm = ilmenite, Tm = titanomagnetite, Ox = FeTi oxide (not determined which), Co = Co silicate

Table A.2: continued

Experiment	SiO2	TiO2	Al2O3	Cr2O3	FeO	MnO	MgO	CaO	Na2O	K2O	TOTAL
					Clinopyroxene - Normalized wt%						
BJR-50	51.18	0.48	2.75	0.00	20.86	0.64	8.54	14.49	0.45	0.60	100
BJR-55	50.34	0.51	3.72	0.00	19.60	0.67	8.00	16.34	0.38	0.45	100
BJR-57	50.41	0.17	1.68	0.00	20.19	0.69	6.41	19.89	0.37	0.20	100
BJR-60	53.67	0.39	4.53	0.00	18.05	0.44	4.72	15.86	0.70	1.64	100
BJR-59	47.45	0.54	1.95	0.00	24.46	0.57	3.76	21.09	0.02	0.16	100
BJR-58	49.43	0.72	2.25	0.00	15.40	0.44	11.09	20.15	0.34	0.19	100
BJR-72	48.31	0.51	4.91	0.00	26.19	0.68	5.13	13.28	0.42	0.58	100
BJR-62	49.22	0.56	4.66	0.00	27.56	0.73	4.03	12.23	0.40	0.61	100
BJR-64	50.43	0.88	5.42	0.00	20.22	0.55	5.81	15.21	0.55	0.94	100
BJR-66	54.53	0.42	3.95	0.00	12.96	0.45	7.39	18.67	0.55	1.07	100
BJR-71	56.33	0.41	4.40	0.00	12.63	0.40	6.96	16.54	0.80	1.54	100
BJR-69	58.12	0.38	5.72	0.00	12.72	0.68	6.10	13.96	1.26	1.07	100
IBR2-29	50.37	0.58	2.94	0.00	19.08	0.36	12.29	14.11	0.28	0.00	100
IBR2-31	51.68	0.56	3.03	0.00	10.30	0.47	14.46	18.77	0.43	0.29	100
IBR2-53	51.46	0.82	2.84	0.00	18.58	0.52	10.10	15.50	0.19	0.00	100
IBR2-10	49.27	1.57	6.34	0.00	15.30	0.30	8.98	16.73	0.66	0.85	100
IBR2-12	52.02	0.55	3.14	0.00	8.83	0.25	15.92	18.89	0.31	0.09	100
IBR2-18	48.71	1.09	7.08	0.00	13.79	0.41	9.89	17.73	0.69	0.61	100
IBR2-15	48.15	0.79	4.81	0.00	17.51	0.56	10.34	17.70	0.14	0.00	100
IBR2-17	51.39	0.52	2.40	0.00	8.15	0.35	15.02	21.64	0.34	0.18	100
IBR2-25	51.13	0.88	2.33	0.00	18.60	0.73	10.28	15.71	0.05	0.29	100
IBR2-27	49.10	1.31	1.99	0.00	21.46	0.69	8.19	16.80	0.38	0.07	100
IBR2-24	51.77	0.56	2.75	0.00	11.64	0.61	12.67	19.37	0.38	0.26	100
IBR2-26	51.81	0.63	3.11	0.00	9.02	0.35	12.89	21.49	0.37	0.33	100
IBR2-20	54.48	0.44	3.53	0.00	15.14	0.65	10.82	13.66	0.45	0.84	100
IBR2-21	53.17	0.88	3.38	0.00	16.36	0.68	10.12	13.67	0.68	1.06	100
IBR2-48	52.78	0.43	0.94	0.00	8.89	0.38	15.87	20.45	0.19	0.08	100
IBR2-53r	51.54	0.53	1.42	0.00	15.85	0.47	13.81	16.05	0.21	0.13	100
IBR2-14	49.48	0.93	6.60	0.00	22.04	0.52	8.29	10.94	0.46	0.73	100
IBR2-35	50.44	1.15	6.45	0.00	11.94	0.36	10.04	18.38	0.62	0.63	100

Table A.2: continued

Experiment	Clinopyroxene - Normalized wt%										
	SiO2	TiO2	Al2O3	Cr2O3	FeO	MnO	MgO	CaO	Na2O	K2O	TOTAL
IBR2-59	51.97	0.57	2.74	0.00	20.09	0.48	11.65	11.55	0.45	0.50	100
IBR2-60	51.87	0.48	1.51	0.00	14.14	0.42	13.70	17.45	0.29	0.12	100
IBR2-63	50.48	0.67	2.78	0.00	20.72	0.48	10.92	13.34	0.34	0.27	100
IBR2-64	50.69	0.50	1.75	0.00	22.16	0.51	12.54	11.52	0.23	0.10	100
IBR2-67	48.14	0.97	4.01	0.00	24.26	0.53	9.09	12.56	0.32	0.13	100
IBR2-69	51.59	0.47	1.25	0.00	15.25	0.49	13.50	17.09	0.24	0.12	100
M12	56.42	0.37	4.00	0.00	7.83	0.00	11.76	18.06	0.80	0.76	100
JI 63	53.12	0.28	1.45	0.00	12.76	0.70	12.37	18.96	0.26	0.09	100
JI 53	52.74	0.40	4.76	0.00	12.80	0.68	9.28	17.77	0.85	0.73	100
JII 34	53.90	0.66	5.20	0.00	10.08	0.00	10.42	18.00	0.95	0.80	100
G-1189	51.97	0.32	1.09	0.00	11.95	0.61	12.83	20.73	0.39	0.11	100
G-1190	51.81	0.20	0.70	0.00	13.24	0.65	12.11	20.86	0.40	0.02	100
G-1194	53.04	0.20	0.65	0.00	9.76	0.46	13.30	22.03	0.46	0.10	100
G-1197	52.98	0.25	1.25	0.00	9.94	0.43	12.97	21.60	0.45	0.14	100
G-1202	51.70	0.36	1.55	0.00	12.68	0.75	10.89	21.33	0.59	0.16	100
G-1203	51.60	0.40	1.34	0.00	13.40	0.59	10.35	21.68	0.51	0.13	100
G-1206	51.60	0.45	1.72	0.00	12.30	0.61	11.33	21.32	0.53	0.14	100
G-1219	53.51	0.28	2.77	0.00	11.61	0.56	10.41	19.96	0.59	0.30	100
G-1225	50.63	0.60	2.50	0.00	14.04	0.81	9.36	21.17	0.71	0.16	100
G-1230	51.14	0.41	1.67	0.00	15.11	0.70	9.18	21.07	0.61	0.11	100
CS-1	50.51	0.60	0.50	0.00	25.65	1.23	1.84	15.88	3.67	0.11	100
CS-7	50.65	0.33	0.31	0.01	28.25	0.95	0.71	15.49	3.20	0.10	100
CS-8	50.94	0.31	0.67	0.00	27.22	1.06	1.35	14.65	3.63	0.16	100
CS-11	50.93	0.25	0.29	0.00	28.50	0.78	0.42	14.14	4.63	0.06	100
CS-16	51.50	0.27	0.50	0.00	25.93	0.89	1.86	15.00	4.05	0.00	100
CS-26	49.74	0.28	0.23	0.00	27.89	0.83	0.97	17.77	2.16	0.14	100
CS-28	50.15	0.19	0.25	0.00	28.33	0.79	0.81	16.75	2.62	0.12	100
CS-32	50.05	0.25	0.27	0.00	27.58	0.82	0.87	17.18	2.83	0.16	100
CS-40	49.96	0.33	0.48	0.01	27.69	0.90	0.74	16.67	3.10	0.12	100
CS-44	50.80	0.00	1.25	0.00	26.93	0.98	1.08	15.49	3.03	0.45	100
SCL01-1	52.29	0.17	0.95	0.01	15.08	0.73	10.95	19.36	0.33	0.14	100
SCL01-3	52.08	0.29	1.50	0.01	15.29	0.78	10.08	19.40	0.35	0.22	100
SCL01-4	52.90	0.18	1.35	0.00	14.67	0.71	10.78	18.77	0.35	0.30	100
SCL01-5	51.89	0.18	1.17	0.01	15.94	0.76	10.20	19.37	0.34	0.15	100

Table A.2: continued

Experiment	SiO2	TiO2	Al2O3	Cr2O3	FeO	MnO	MgO	CaO	Na2O	K2O	TOTAL
					Glass - Normalized wt%						
BJR-50	74.21	0.39	11.71	0.00	3.82	0.08	0.19	1.10	2.43	6.08	100
BJR-55	74.57	0.39	12.36	0.00	3.04	0.01	0.11	0.99	2.28	6.25	100
BJR-57	75.54	0.25	12.33	0.00	2.14	0.00	0.22	0.99	2.39	6.14	100
BJR-60	74.33	0.45	12.17	0.00	3.54	0.07	0.11	0.88	2.33	6.10	100
BJR-59	74.73	0.37	12.36	0.00	2.96	0.05	0.12	0.89	2.40	6.12	100
BJR-58	75.81	0.24	12.41	0.00	1.73	0.03	0.15	1.03	2.35	6.24	100
BJR-72	75.29	0.32	12.21	0.00	2.95	0.08	0.07	0.86	2.29	5.94	100
BJR-62	76.94	0.41	12.25	0.00	1.62	0.00	0.01	0.69	2.33	5.74	100
BJR-64	76.85	0.23	12.20	0.00	1.69	0.16	0.06	0.84	2.24	5.72	100
BJR-66	77.12	0.17	12.16	0.00	1.60	0.13	0.11	0.77	2.20	5.73	100
BJR-71	76.96	0.19	12.07	0.00	1.23	0.05	0.11	0.90	2.51	5.98	100
BJR-69	76.60	0.17	12.65	0.00	0.98	0.00	0.06	0.95	2.78	5.80	100
IBR2-29	72.42	0.64	12.93	0.00	3.47	0.06	0.32	1.61	2.81	5.72	100
IBR2-31	72.29	0.65	12.95	0.00	3.51	0.04	0.41	1.75	2.92	5.49	100
IBR2-53	73.41	0.52	12.94	0.00	2.88	0.09	0.26	1.25	2.64	6.01	100
IBR2-10	74.58	0.46	12.60	0.00	2.35	0.08	0.12	0.97	2.64	6.20	100
IBR2-12	73.48	0.39	13.38	0.00	2.31	0.01	0.52	1.33	2.59	5.99	100
IBR2-18	75.86	0.42	12.10	0.00	2.08	0.00	0.16	0.77	2.45	6.16	100
IBR2-15	76.36	0.38	12.02	0.00	1.89	0.13	0.08	0.71	2.36	6.07	100
IBR2-17	73.31	0.50	13.67	0.00	1.99	0.02	0.41	1.83	2.84	5.42	100
IBR2-25	76.16	0.30	12.48	0.00	1.65	0.06	0.09	0.74	2.41	6.11	100
IBR2-27	75.31	0.32	12.80	0.00	1.58	0.11	0.18	1.03	2.69	5.99	100
IBR2-24	75.30	0.41	12.93	0.00	1.60	0.06	0.23	1.08	2.54	5.86	100
IBR2-26	73.54	0.47	14.11	0.00	1.73	0.05	0.34	1.75	2.65	5.37	100
IBR2-20	76.48	0.36	12.36	0.00	1.48	0.01	0.05	0.74	2.35	6.17	100
IBR2-21	76.81	0.26	12.65	0.00	1.23	0.10	0.12	0.67	2.36	5.81	100
IBR2-48	71.80	0.67	13.52	0.00	2.79	0.00	0.62	2.28	3.20	5.10	100
IBR2-53r	71.91	0.69	13.37	0.00	3.25	0.00	0.51	1.97	2.95	5.34	100
IBR2-14	73.55	0.53	12.55	0.00	2.81	0.05	0.20	1.04	2.88	6.39	100
IBR2-35	73.91	0.51	12.81	0.00	2.47	0.00	0.26	1.23	3.11	5.70	100

Table A.2: continued

Experiment	Glass - Normalized wt%										
	SiO2	TiO2	Al2O3	Cr2O3	FeO	MnO	MgO	CaO	Na2O	K2O	TOTAL
IBR2-59	71.52	0.67	13.14	0.00	3.84	0.00	0.50	1.97	3.15	5.22	100
IBR2-60	71.80	0.66	13.50	0.00	3.10	0.00	0.58	2.06	3.10	5.20	100
IBR2-63	71.43	0.66	13.34	0.00	3.72	0.00	0.41	2.00	3.09	5.34	100
IBR2-64	71.69	0.64	13.32	0.00	3.57	0.00	0.46	2.00	3.00	5.32	100
IBR2-67	72.14	0.54	13.49	0.00	3.20	0.00	0.30	1.90	3.05	5.37	100
IBR2-69	72.56	0.67	13.52	0.00	2.49	0.00	0.51	1.97	2.92	5.36	100
M12	76.58	0.25	12.80	0.00	0.78	0.05	0.19	0.82	3.15	5.38	100
JI 63	75.24	0.20	13.20	0.00	1.39	0.05	0.19	1.23	3.22	5.28	100
JI 53	76.61	0.13	12.50	0.00	1.10	0.05	0.11	0.79	2.99	5.71	100
JII 34	76.37	0.23	13.01	0.00	0.94	0.06	0.18	1.15	2.85	5.22	100
G-1189	76.12	0.13	13.10	0.00	0.84	0.03	0.02	0.31	3.89	5.56	100
G-1190	76.68	0.14	12.82	0.00	0.61	0.04	0.05	0.29	3.82	5.55	100
G-1194	76.30	0.13	12.99	0.00	0.77	0.03	0.11	0.42	3.81	5.44	100
G-1197	76.92	0.10	12.80	0.00	0.69	0.02	0.08	0.30	3.87	5.22	100
G-1202	76.81	0.11	12.86	0.00	0.61	0.01	0.08	0.36	3.88	5.29	100
G-1203	76.75	0.07	12.89	0.00	0.64	0.03	0.05	0.40	4.00	5.17	100
G-1206	77.17	0.10	12.59	0.00	0.70	0.02	0.10	0.29	3.92	5.11	100
G-1219	78.07	0.12	12.31	0.00	0.51	0.04	0.04	0.24	3.90	4.77	100
G-1225	78.02	0.10	12.36	0.00	0.53	0.09	0.03	0.23	3.99	4.65	100
G-1230	77.78	0.07	12.43	0.00	0.56	0.01	0.04	0.38	3.85	4.88	100
CS-1	75.35	0.23	10.70	0.00	3.52	0.09	0.01	0.23	6.02	3.86	100
CS-7	76.52	0.09	11.40	0.00	2.73	0.07	0.00	0.13	5.97	3.08	100
CS-8	76.20	0.12	11.30	0.00	2.44	0.06	0.01	0.19	6.43	3.26	100
CS-11	75.75	0.13	11.37	0.00	3.32	0.07	0.00	0.15	5.97	3.24	100
CS-16	76.86	0.16	11.01	0.00	2.31	0.07	0.01	0.15	6.02	3.41	100
CS-26	75.83	0.17	10.64	0.00	2.68	0.07	0.00	0.07	6.30	4.24	100
CS-28	75.39	0.12	10.89	0.00	2.60	0.07	0.00	0.10	6.72	4.09	100
CS-32	74.69	0.21	9.73	0.00	4.09	0.11	0.00	0.10	6.53	4.55	100
CS-40	75.17	0.16	11.05	0.00	3.64	0.09	0.01	0.16	5.63	4.09	100
CS-44	74.91	0.22	10.24	0.00	4.03	0.13	0.01	0.21	5.69	4.55	100
SCL01-1	76.41	0.21	13.06	0.00	1.06	0.02	0.13	0.88	3.16	5.07	100
SCL01-3	76.61	0.16	13.16	0.00	0.87	0.04	0.07	0.78	3.16	5.15	100
SCL01-4	77.87	0.17	12.44	0.00	0.70	0.06	0.04	0.63	3.06	5.02	100
SCL01-5	77.02	0.18	12.96	0.00	0.78	0.03	0.05	0.72	3.11	5.15	100

Table A.3: Calibration Dataset: Whole Rock

Sample	Reference	Locality	SiO2	TiO2	Al2O3	FeO	MnO	MgO	CaO	Na2O	K2O	P2O5	TOTAL
CPTXVj9j	Almeev et al., 2012	Cougar Point Tuff	74.08	0.43	12.51	3.15	0.04	0.35	1.08	2.40	5.89	0.06	99.99
IB THT-02	Almeev et al., 2012	Indian Batt rhyolite	70.12	0.67	14.13	4.14	0.07	0.67	2.44	2.71	4.91	0.14	100.00
09_018	Bolte et al., 2015	Blacktail Creek Tuff	74.57	0.30	12.82	2.25	0.05	0.25	1.14	3.12	5.26	0.08	99.84
AB-6202	Gardner et al., 2014	Late-erupted Bishop Tuff	76.01	0.19	12.79	1.08	0.02	0.20	0.81	3.38	5.48	0.04	100.00
PEK-62	Iacovino et al., 2015	Paektu	74.59	0.21	10.58	4.21	0.08	0.02	0.22	5.58	4.51	0.01	100.00
SL-32-05	Girard & Stix, 2009	Scaup Lake, Yellowstone	73.26	0.26	12.51	1.69	0.04	0.23	0.84	3.30	5.18	0.04	97.35

Table A.4: Natural System Clinopyroxene & Glass

Sample	Reference	Locality	Clinopyroxene - Normalized wt%										
			SiO2	TiO2	Al2O3	Cr2O3	FeO	MnO	MgO	CaO	Na2O	K2O	TOTAL
AB-6202	Gardner et al., 2014	Late-erupted Bishop Tuff (Ig2)	52.31	0.19	0.63	0.00	12.33	0.69	12.56	20.90	0.40	0.00	100
14	Hildreth, 1977	Late-erupted Bishop Tuff (Ig2)	51.58	0.16	0.71	0.00	13.00	0.57	12.55	21.02	0.40	0.00	100
19	Hildreth, 1977	Late-erupted Bishop Tuff (Ig2)	52.13	0.13	0.77	0.00	12.62	0.60	12.52	20.86	0.38	0.00	100
20	Hildreth, 1977	Late-erupted Bishop Tuff (Ig2)	52.14	0.19	0.76	0.00	12.28	0.51	12.95	20.77	0.39	0.00	100
48	Hildreth, 1977	Late-erupted Bishop Tuff (Ig2)	51.58	0.18	0.88	0.00	13.65	0.55	12.33	19.95	0.39	0.00	100
51	Hildreth, 1977	Late-erupted Bishop Tuff (Ig2)	51.88	0.17	0.94	0.00	12.92	0.57	12.62	20.53	0.36	0.00	100
63	Hildreth, 1977	Late-erupted Bishop Tuff (Ig2)	51.89	0.14	0.77	0.00	12.68	0.57	12.84	20.74	0.36	0.00	100
69	Hildreth, 1977	Late-erupted Bishop Tuff (Ig2)	52.07	0.15	0.75	0.00	12.86	0.54	12.77	20.50	0.37	0.00	100
70a	Hildreth, 1977	Late-erupted Bishop Tuff (Ig2)	51.86	0.22	0.87	0.00	12.15	0.47	13.43	20.59	0.41	0.00	100
70b	Hildreth, 1977	Late-erupted Bishop Tuff (Ig2)	51.55	0.16	0.80	0.00	13.40	0.67	12.51	20.52	0.38	0.00	100
71	Hildreth, 1977	Late-erupted Bishop Tuff (Ig2)	51.93	0.13	0.68	0.00	12.89	0.58	12.70	20.70	0.38	0.00	100
72	Hildreth, 1977	Late-erupted Bishop Tuff (Ig2)	52.25	0.15	0.71	0.00	13.00	0.56	12.50	20.42	0.40	0.00	100
73	Hildreth, 1977	Late-erupted Bishop Tuff (Ig2)	51.89	0.13	0.71	0.00	13.21	0.58	12.52	20.59	0.37	0.00	100
74	Hildreth, 1977	Late-erupted Bishop Tuff (Ig2)	51.97	0.15	0.70	0.00	12.88	0.57	12.62	20.73	0.39	0.00	100
77	Hildreth, 1977	Late-erupted Bishop Tuff (Ig2)	51.72	0.14	0.69	0.00	13.06	0.60	12.62	20.80	0.36	0.00	100
78	Hildreth, 1977	Late-erupted Bishop Tuff (Ig2)	52.39	0.13	0.66	0.00	12.97	0.62	12.29	20.56	0.38	0.00	100
79	Hildreth, 1977	Late-erupted Bishop Tuff (Ig2)	51.70	0.13	0.67	0.00	12.84	0.60	12.91	20.78	0.36	0.00	100
107	Hildreth, 1977	Late-erupted Bishop Tuff (Ig2)	52.21	0.14	0.65	0.00	12.63	0.54	12.86	20.63	0.34	0.00	100
108	Hildreth, 1977	Late-erupted Bishop Tuff (Ig2)	52.29	0.15	0.71	0.00	13.03	0.59	12.37	20.49	0.39	0.00	100
133	Hildreth, 1977	Late-erupted Bishop Tuff (Ig2)	51.96	0.14	0.69	0.00	13.03	0.56	12.52	20.72	0.39	0.00	100
134	Hildreth, 1977	Late-erupted Bishop Tuff (Ig2)	52.11	0.15	0.73	0.00	12.81	0.57	12.75	20.46	0.40	0.00	100
135	Hildreth, 1977	Late-erupted Bishop Tuff (Ig2)	51.88	0.13	0.65	0.00	12.77	0.54	12.84	20.78	0.39	0.00	100
136	Hildreth, 1977	Late-erupted Bishop Tuff (Ig2)	52.20	0.21	0.72	0.00	12.28	0.44	13.25	20.52	0.39	0.00	100
137	Hildreth, 1977	Late-erupted Bishop Tuff (Ig2)	51.88	0.12	0.83	0.00	12.66	0.54	12.87	20.72	0.38	0.00	100
138	Hildreth, 1977	Late-erupted Bishop Tuff (Ig2)	51.99	0.12	0.73	0.00	12.89	0.55	12.70	20.62	0.39	0.00	100
139	Hildreth, 1977	Late-erupted Bishop Tuff (Ig2)	52.05	0.15	0.70	0.00	12.67	0.57	12.64	20.83	0.38	0.00	100
142	Hildreth, 1977	Late-erupted Bishop Tuff (Ig2)	51.97	0.15	1.02	0.00	12.73	0.54	12.60	20.61	0.39	0.00	100
143	Hildreth, 1977	Late-erupted Bishop Tuff (Ig2)	51.92	0.16	0.72	0.00	12.68	0.55	12.71	20.88	0.38	0.00	100
Tshirege bottom	Warshaw & Smith, 1988	Bandelier Tuff	48.67	0.08	0.30	0.00	27.08	2.58	2.47	18.23	0.59	0.00	100
Tshirege top III	Warshaw & Smith, 1988	Bandelier Tuff	55.39	0.11	0.31	0.00	26.31	2.20	6.30	8.83	0.54	0.00	100
Tshirege top V	Warshaw & Smith, 1988	Bandelier Tuff	52.17	0.21	0.92	0.00	13.20	1.11	12.53	19.32	0.54	0.00	100
62-X1	Iacovino et al., 2016	Paektu comendite	48.61	0.22	0.28	0.00	28.83	0.89	0.82	18.69	1.66	0.00	100
62-X2	Iacovino et al., 2016	Paektu comendite	49.31	0.23	0.17	0.00	28.40	0.88	0.93	18.44	1.64	0.00	100
62-X3	Iacovino et al., 2016	Paektu comendite	48.89	0.21	0.13	0.00	29.03	0.87	0.82	18.24	1.80	0.00	100
YS-7 (rim)	Sisson, 1991	Huckleberry Ridge Tuff	48.38	0.16	0.61	0.00	27.35	0.86	3.11	19.23	0.30	0.00	100
YS-8 (rim)	Sisson, 1991	Huckleberry Ridge Tuff	48.60	0.23	0.58	0.00	27.46	0.85	3.45	18.54	0.29	0.00	100
Y82	Befus & Gardner, 2016	Solfatara Plateau	49.13	0.21	0.45	0.00	26.53	0.73	4.09	18.56	0.31	0.00	100
SP138-2	Girard & Stix, 2010	Solfatara Plateau	49.55	0.23	0.52	0.00	26.21	1.01	4.14	18.03	0.29	0.02	100
BS132	Girard & Stix, 2010	South Biscuit Basin	51.81	0.19	0.68	0.00	16.54	0.84	10.76	18.87	0.29	0.02	100
74Y-180-B	Hildreth, personal comm.	Lava Creek Tuff A	49.03	0.22	0.64	0.00	26.75	0.69	4.50	17.83	0.34	0.00	100

Table A.4: continued

Sample	Reference	Locality	Clinopyroxene - Normalized wt%										
			SiO2	TiO2	Al2O3	Cr2O3	FeO	MnO	MgO	CaO	Na2O	K2O	TOTAL
6YC-32	Hildreth, personal comm.	Lava Creek Tuff A	50.83	0.16	0.59	0.00	18.24	0.57	10.37	18.94	0.31	0.00	100
74Y-130-A	Hildreth, personal comm.	Lava Creek Tuff A	48.87	0.17	0.67	0.00	26.43	0.77	4.31	18.45	0.33	0.00	100
8YC-371-A	Hildreth, personal comm.	Lava Creek Tuff A	48.07	0.17	0.62	0.00	25.87	0.75	5.25	18.93	0.33	0.00	100
8YC-401-A	Hildreth, personal comm.	Lava Creek Tuff A	47.92	0.29	0.67	0.00	28.27	0.75	3.53	18.25	0.31	0.00	100
9YC-520-A	Hildreth, personal comm.	Lava Creek Tuff B	48.95	0.23	0.40	0.00	26.02	0.72	5.40	17.98	0.29	0.00	100
7YC-185	Hildreth, personal comm.	Lava Creek Tuff B	48.19	0.27	0.66	0.00	27.74	0.76	3.71	18.36	0.31	0.00	100
8YC-411	Hildreth, personal comm.	Lava Creek Tuff B	48.64	0.28	0.67	0.00	27.30	0.70	3.79	18.31	0.31	0.00	100
6YC-65 (xtl ash)	Hildreth, personal comm.	Lava Creek Tuff B	48.67	0.25	0.72	0.00	27.32	0.74	3.83	18.18	0.30	0.00	100
7YC-325	Hildreth, personal comm.	Lava Creek Tuff B	49.26	0.19	0.52	0.00	24.13	0.71	6.12	18.76	0.31	0.00	100
7YC-315	Hildreth, personal comm.	Lava Creek Tuff B	48.07	0.27	0.74	0.00	27.16	0.74	4.26	18.44	0.32	0.00	100
8YC-408-E	Hildreth, personal comm.	Lava Creek Tuff B	49.37	0.16	0.55	0.00	24.94	0.75	5.29	18.65	0.30	0.00	100
65YR-27-A	Hildreth, personal comm.	Lava Creek Tuff B	48.47	0.22	0.64	0.00	27.17	0.71	4.58	17.91	0.31	0.00	100
9YC-545	Hildreth, personal comm.	Lava Creek Tuff B	49.62	0.18	0.56	0.00	25.41	0.72	4.99	18.23	0.30	0.00	100
9YC-525	Hildreth, personal comm.	Lava Creek Tuff B	48.91	0.23	0.70	0.00	26.80	0.72	4.24	18.13	0.28	0.00	100
6YC-13-B	Hildreth, personal comm.	Lava Creek Tuff B	49.62	0.18	0.56	0.00	25.41	0.72	4.99	18.23	0.30	0.00	100
8YC-455	Hildreth, personal comm.	Lava Creek Tuff B	47.84	0.26	0.70	0.00	27.92	0.73	3.93	18.31	0.30	0.00	100
7YC-321-A	Hildreth, personal comm.	Lava Creek Tuff B	48.07	0.22	0.64	0.00	27.35	0.72	4.16	18.50	0.32	0.00	100
7YC-311-A	Hildreth, personal comm.	Lava Creek Tuff B	48.40	0.17	0.59	0.00	26.80	0.75	4.50	18.50	0.30	0.00	100
8YC-443	Hildreth, personal comm.	Lava Creek Tuff B	48.62	0.27	0.62	0.00	26.77	0.75	4.11	18.55	0.31	0.00	100
9YC-546	Hildreth, personal comm.	Lava Creek Tuff B	47.15	0.23	0.61	0.00	27.99	0.77	4.07	18.86	0.32	0.00	100
6YC-13-E	Hildreth, personal comm.	Lava Creek Tuff B	47.86	0.28	0.72	0.00	27.34	0.77	4.14	18.55	0.34	0.00	100
001-03-1a_cpxrim	Hildreth, personal comm.	Scaup Lake, Yellowstone	51.32	0.18	0.62	0.03	15.54	0.74	11.07	20.12	0.32	0.06	100
001-03-1c_cpxrim	Hildreth, personal comm.	Scaup Lake, Yellowstone	51.53	0.12	0.63	0.00	15.46	0.73	11.14	20.03	0.32	0.02	100
001-04_1a_pxrim	Hildreth, personal comm.	Scaup Lake, Yellowstone	50.69	0.20	0.64	0.00	18.36	0.85	9.82	19.06	0.35	0.02	100
001-04_1d_pxrim	Hildreth, personal comm.	Scaup Lake, Yellowstone	51.61	0.18	0.59	0.00	15.48	0.77	10.97	20.03	0.32	0.04	100
001-07-1b_cpxrim	Hildreth, personal comm.	Scaup Lake, Yellowstone	51.51	0.17	0.67	0.00	15.67	0.76	11.06	19.84	0.28	0.05	100
001-07-1d_cpxrim	Hildreth, personal comm.	Scaup Lake, Yellowstone	51.62	0.18	0.68	0.00	15.47	0.79	11.00	19.88	0.34	0.04	100
001-10-1a_pxrim	Hildreth, personal comm.	Scaup Lake, Yellowstone	51.49	0.15	0.70	0.00	15.54	0.77	11.06	19.99	0.31	0.01	100
001-10-1c_pxrim	Hildreth, personal comm.	Scaup Lake, Yellowstone	51.32	0.17	0.67	0.00	15.43	0.76	11.23	20.04	0.34	0.03	100
001-10-1e_pxrim	Hildreth, personal comm.	Scaup Lake, Yellowstone	51.58	0.17	0.62	0.01	15.01	0.76	11.31	20.16	0.33	0.05	100
001-23-1a_pxrim	Hildreth, personal comm.	Scaup Lake, Yellowstone	51.72	0.20	0.68	0.00	15.41	0.75	11.04	19.81	0.31	0.06	100
001-23-1c_pxrim	Hildreth, personal comm.	Scaup Lake, Yellowstone	51.61	0.17	0.66	0.01	14.99	0.74	11.29	20.19	0.32	0.03	100
001-29-1b_pxrim	Hildreth, personal comm.	Scaup Lake, Yellowstone	51.35	0.15	0.62	0.01	15.53	0.74	11.18	19.99	0.39	0.04	100
001-29-2b_pxrim	Hildreth, personal comm.	Scaup Lake, Yellowstone	51.52	0.18	0.65	0.00	15.33	0.70	11.27	20.01	0.32	0.03	100
001-30-1a_pxrim	Hildreth, personal comm.	Scaup Lake, Yellowstone	51.56	0.16	0.66	0.01	15.06	0.81	11.21	20.19	0.33	0.02	100
001-30-2b_pxrim	Hildreth, personal comm.	Scaup Lake, Yellowstone	51.24	0.17	0.63	0.00	15.72	0.66	11.13	20.07	0.36	0.03	100
001-30-3b_pxrim	Hildreth, personal comm.	Scaup Lake, Yellowstone	51.37	0.17	0.63	0.01	15.70	0.71	11.11	19.97	0.32	0.00	100
001-30-4a_pxrim	Hildreth, personal comm.	Scaup Lake, Yellowstone	51.45	0.21	0.60	0.03	15.14	0.78	11.26	20.18	0.32	0.03	100
002-02-1a_pxrim	Hildreth, personal comm.	Scaup Lake, Yellowstone	51.36	0.18	0.61	0.02	15.15	0.82	11.17	20.30	0.34	0.05	100
002-05-1b_pxrim	Hildreth, personal comm.	Scaup Lake, Yellowstone	51.84	0.20	0.61	0.01	14.64	0.67	11.34	20.34	0.32	0.02	100

Sample	Reference	Locality	Clinopyroxene - Normalized wt%										
			SiO2	TiO2	Al2O3	Cr2O3	FeO	MnO	MgO	CaO	Na2O	K2O	TOTAL
002-05-2a_pxrim	Hildreth, personal comm.	Scaup Lake, Yellowstone	51.41	0.19	0.62	0.00	15.52	0.73	11.21	19.95	0.34	0.02	100
002-13-1a_pxrim	Hildreth, personal comm.	Scaup Lake, Yellowstone	51.49	0.17	0.61	0.00	15.33	0.72	11.26	20.02	0.35	0.04	100
002-27-1a_pxrim	Hildreth, personal comm.	Scaup Lake, Yellowstone	51.45	0.21	0.70	0.01	16.08	0.76	11.05	19.38	0.33	0.03	100
002-27-2a_pxrim	Hildreth, personal comm.	Scaup Lake, Yellowstone	51.58	0.17	0.70	0.01	15.10	0.83	11.03	20.27	0.28	0.03	100
002-28-1b_pxrim	Hildreth, personal comm.	Scaup Lake, Yellowstone	51.44	0.16	0.63	0.00	15.18	0.79	11.23	20.20	0.34	0.02	100
002-28-1d_pxrim	Hildreth, personal comm.	Scaup Lake, Yellowstone	51.60	0.17	0.62	0.01	15.12	0.69	11.25	20.18	0.33	0.03	100
002-28-2b_pxrim	Hildreth, personal comm.	Scaup Lake, Yellowstone	51.44	0.14	0.65	0.00	15.10	0.80	11.33	20.20	0.32	0.03	100
002-31-1a_pxrim	Hildreth, personal comm.	Scaup Lake, Yellowstone	51.26	0.18	0.73	0.00	16.41	0.86	10.99	19.19	0.33	0.04	100
002-31-1c_pxrim	Hildreth, personal comm.	Scaup Lake, Yellowstone	51.62	0.13	0.65	0.00	15.33	0.78	11.18	19.95	0.31	0.03	100
002-31-2a_pxrim	Hildreth, personal comm.	Scaup Lake, Yellowstone	51.56	0.17	0.60	0.00	15.37	0.73	11.23	20.03	0.28	0.04	100
002-34-1b_pxrim	Hildreth, personal comm.	Scaup Lake, Yellowstone	51.37	0.16	0.61	0.01	15.81	0.76	10.95	19.95	0.35	0.03	100
002-41-1b_pxrim	Hildreth, personal comm.	Scaup Lake, Yellowstone	51.48	0.18	0.61	0.01	15.66	0.71	10.99	20.00	0.35	0.01	100
002-43-1b_pxrim	Hildreth, personal comm.	Scaup Lake, Yellowstone	51.48	0.16	0.64	0.00	15.49	0.72	11.18	19.95	0.33	0.04	100
002-43-2b_pxrim	Hildreth, personal comm.	Scaup Lake, Yellowstone	51.68	0.20	0.66	0.01	15.49	0.76	11.15	19.73	0.29	0.04	100
006-04-1a_pxrim	Hildreth, personal comm.	Scaup Lake, Yellowstone	51.69	0.16	0.57	0.00	15.28	0.68	11.28	19.96	0.33	0.05	100
006-06-1a_pxrim	Hildreth, personal comm.	Scaup Lake, Yellowstone	51.54	0.18	0.66	0.00	15.45	0.71	11.27	19.88	0.30	0.01	100
006-06-2a_pxrim	Hildreth, personal comm.	Scaup Lake, Yellowstone	51.54	0.17	0.61	0.00	15.41	0.74	11.13	20.07	0.29	0.03	100
006-12-1b_pxrim	Hildreth, personal comm.	Scaup Lake, Yellowstone	51.40	0.18	0.62	0.00	15.64	0.87	11.05	19.93	0.28	0.03	100
006-27-1a_pxrim	Hildreth, personal comm.	Scaup Lake, Yellowstone	51.80	0.16	0.64	0.00	15.11	0.69	11.20	20.02	0.32	0.05	100
006-35-1b_pxrim	Hildreth, personal comm.	Scaup Lake, Yellowstone	51.53	0.21	0.63	0.02	15.37	0.70	11.08	20.08	0.33	0.02	100
006-35-2a_pxrim	Hildreth, personal comm.	Scaup Lake, Yellowstone	51.52	0.18	0.61	0.00	15.61	0.74	11.11	19.92	0.30	0.02	100
006-43-1c_pxrim	Hildreth, personal comm.	Scaup Lake, Yellowstone	51.80	0.18	0.63	0.01	14.98	0.85	11.28	19.91	0.32	0.04	100
006-44-1c_pxrim	Hildreth, personal comm.	Scaup Lake, Yellowstone	51.74	0.19	0.64	0.00	15.26	0.78	11.09	19.96	0.31	0.03	100
008-08-1b_pxrim	Hildreth, personal comm.	Scaup Lake, Yellowstone	51.11	0.22	0.64	0.00	16.51	0.83	10.73	19.63	0.33	0.00	100
008-09-1a_pxrim	Hildreth, personal comm.	Scaup Lake, Yellowstone	51.26	0.20	0.66	0.01	16.08	0.75	10.94	19.75	0.32	0.03	100
008-09-1c_pxrim	Hildreth, personal comm.	Scaup Lake, Yellowstone	51.51	0.17	0.60	0.01	15.51	0.69	11.09	20.09	0.30	0.03	100
008-10-1a_pxrim	Hildreth, personal comm.	Scaup Lake, Yellowstone	51.63	0.15	0.62	0.00	15.37	0.76	11.05	20.06	0.32	0.04	100
008-11-1a_pxrim	Hildreth, personal comm.	Scaup Lake, Yellowstone	51.64	0.13	0.61	0.00	15.41	0.71	11.25	19.92	0.31	0.02	100
008-12-1b_pxrim	Hildreth, personal comm.	Scaup Lake, Yellowstone	51.35	0.19	0.63	0.01	15.56	0.70	11.17	20.06	0.32	0.02	100
008-12-2a_pxrim	Hildreth, personal comm.	Scaup Lake, Yellowstone	51.23	0.17	0.60	0.00	15.79	0.75	11.09	20.01	0.31	0.05	100
008-13-1b_pxrim	Hildreth, personal comm.	Scaup Lake, Yellowstone	51.58	0.19	0.63	0.00	15.34	0.77	11.13	20.04	0.31	0.01	100
008-19-1b_pxrim	Hildreth, personal comm.	Scaup Lake, Yellowstone	51.38	0.20	0.58	0.02	15.34	0.71	11.25	20.20	0.28	0.04	100
008-24-1b_pxrim	Hildreth, personal comm.	Scaup Lake, Yellowstone	51.52	0.18	0.60	0.01	15.05	0.72	11.42	20.15	0.32	0.03	100
008-24-1d_pxrim	Hildreth, personal comm.	Scaup Lake, Yellowstone	51.32	0.18	0.63	0.00	15.61	0.69	11.37	19.86	0.30	0.02	100
008-25-1a_pxrim	Hildreth, personal comm.	Scaup Lake, Yellowstone	51.53	0.17	0.61	0.00	15.46	0.71	11.09	20.09	0.31	0.02	100
008-26-1b_pxrim	Hildreth, personal comm.	Scaup Lake, Yellowstone	51.55	0.18	0.64	0.00	15.38	0.76	11.14	20.02	0.30	0.03	100
008-29-2c_pxrim	Hildreth, personal comm.	Scaup Lake, Yellowstone	51.74	0.18	0.72	0.01	14.46	0.62	11.79	20.06	0.36	0.05	100
008-29-3a_pxrim	Hildreth, personal comm.	Scaup Lake, Yellowstone	51.53	0.14	0.66	0.00	16.09	0.82	11.19	19.22	0.32	0.03	100
008-31-1a_pxrim	Hildreth, personal comm.	Scaup Lake, Yellowstone	51.33	0.15	0.64	0.00	16.01	0.79	11.12	19.61	0.34	0.01	100
008-34-1a_pxrim	Hildreth, personal comm.	Scaup Lake, Yellowstone	51.63	0.19	0.59	0.00	15.05	0.71	11.29	20.16	0.34	0.04	100

Sample	Reference	Locality	Clinopyroxene - Normalized wt%										
			SiO2	TiO2	Al2O3	Cr2O3	FeO	MnO	MgO	CaO	Na2O	K2O	TOTAL
008-37-1b_pxrim	Hildreth, personal comm.	Scaup Lake, Yellowstone	51.52	0.15	0.60	0.03	15.49	0.66	11.13	20.07	0.32	0.04	100
008-37-1d_pxrim	Hildreth, personal comm.	Scaup Lake, Yellowstone	51.46	0.15	0.66	0.00	15.30	0.72	11.27	20.10	0.31	0.03	100
008-41-1b_pxrim	Hildreth, personal comm.	Scaup Lake, Yellowstone	51.57	0.18	0.63	0.00	15.10	0.80	11.22	20.14	0.32	0.04	100
008-42-1a_pxrim	Hildreth, personal comm.	Scaup Lake, Yellowstone	51.56	0.19	0.66	0.01	15.77	0.76	11.02	19.69	0.32	0.03	100
KB-YS-12_1e_rim_1	Hildreth, personal comm.	Scaup Lake, Yellowstone	51.90	0.15	0.63	0.00	15.33	0.72	10.85	20.09	0.31	0.02	100
KB-YS-12_1e_rim_2	Hildreth, personal comm.	Scaup Lake, Yellowstone	51.84	0.19	0.72	0.00	15.20	0.73	10.81	20.23	0.26	0.00	100
KB-YS-12_1f_rim_1	Hildreth, personal comm.	Scaup Lake, Yellowstone	51.68	0.21	0.68	0.00	15.74	0.76	10.83	19.78	0.30	0.02	100
KB-YS-12_1f_rim_2	Hildreth, personal comm.	Scaup Lake, Yellowstone	52.32	0.22	0.68	0.00	14.92	0.72	10.92	19.94	0.27	0.01	100
KB-YS-12_2f_rim_1	Hildreth, personal comm.	Scaup Lake, Yellowstone	51.68	0.12	0.64	0.00	15.04	0.71	11.42	20.06	0.31	0.02	100
KB-YS-12_2f_rim_2	Hildreth, personal comm.	Scaup Lake, Yellowstone	51.89	0.19	0.63	0.00	14.79	0.72	11.29	20.18	0.28	0.03	100
KB-YS-13_1c_rim_1	Hildreth, personal comm.	Scaup Lake, Yellowstone	52.32	0.18	0.68	0.01	14.58	0.79	11.23	19.86	0.32	0.05	100
KB-YS-13_1c_rim_2	Hildreth, personal comm.	Scaup Lake, Yellowstone	52.03	0.19	0.72	0.00	14.74	0.73	11.19	20.04	0.29	0.06	100
KB-YS-13_2d_rim_1	Hildreth, personal comm.	Scaup Lake, Yellowstone	51.92	0.18	0.68	0.02	14.95	0.66	11.27	19.99	0.30	0.02	100
KB-YS-13_2d_rim_2	Hildreth, personal comm.	Scaup Lake, Yellowstone	52.06	0.18	0.69	0.00	14.82	0.75	11.15	19.99	0.33	0.03	100
KB-YS-13_3a_rim_1	Hildreth, personal comm.	Scaup Lake, Yellowstone	52.02	0.16	0.68	0.00	15.53	0.80	10.76	19.75	0.29	0.01	100
KB-YS-13_3a_rim_2	Hildreth, personal comm.	Scaup Lake, Yellowstone	52.02	0.18	0.66	0.00	15.53	0.79	10.77	19.74	0.28	0.02	100

Table A.4: continued

Sample	SiO2	TiO2	Al2O3	Cr2O3	FeO	MnO	MgO	CaO	Na2O	K2O	TOTAL	Glass Reference (if different)	Sample
					Glass - Normalized wt%								
AB-6202	77.90	0.13	12.27	0.00	0.54	0.02	0.08	0.19	3.70	5.17	100		
14	77.90	0.13	12.27	0.00	0.54	0.02	0.08	0.19	3.70	5.17	100	a	AB-6202
19	77.90	0.13	12.27	0.00	0.54	0.02	0.08	0.19	3.70	5.17	100	a	AB-6202
20	77.90	0.13	12.27	0.00	0.54	0.02	0.08	0.19	3.70	5.17	100	a	AB-6202
48	77.90	0.13	12.27	0.00	0.54	0.02	0.08	0.19	3.70	5.17	100	a	AB-6202
51	77.90	0.13	12.27	0.00	0.54	0.02	0.08	0.19	3.70	5.17	100	a	AB-6202
63	77.90	0.13	12.27	0.00	0.54	0.02	0.08	0.19	3.70	5.17	100	a	AB-6202
69	77.90	0.13	12.27	0.00	0.54	0.02	0.08	0.19	3.70	5.17	100	a	AB-6202
70a	77.90	0.13	12.27	0.00	0.54	0.02	0.08	0.19	3.70	5.17	100	a	AB-6202
70b	77.90	0.13	12.27	0.00	0.54	0.02	0.08	0.19	3.70	5.17	100	a	AB-6202
71	77.90	0.13	12.27	0.00	0.54	0.02	0.08	0.19	3.70	5.17	100	a	AB-6202
72	77.90	0.13	12.27	0.00	0.54	0.02	0.08	0.19	3.70	5.17	100	a	AB-6202
73	77.90	0.13	12.27	0.00	0.54	0.02	0.08	0.19	3.70	5.17	100	a	AB-6202
74	77.90	0.13	12.27	0.00	0.54	0.02	0.08	0.19	3.70	5.17	100	a	AB-6202
77	77.90	0.13	12.27	0.00	0.54	0.02	0.08	0.19	3.70	5.17	100	a	AB-6202
78	77.90	0.13	12.27	0.00	0.54	0.02	0.08	0.19	3.70	5.17	100	a	AB-6202
79	77.90	0.13	12.27	0.00	0.54	0.02	0.08	0.19	3.70	5.17	100	a	AB-6202
107	77.90	0.13	12.27	0.00	0.54	0.02	0.08	0.19	3.70	5.17	100	a	AB-6202
108	77.90	0.13	12.27	0.00	0.54	0.02	0.08	0.19	3.70	5.17	100	a	AB-6202
133	77.90	0.13	12.27	0.00	0.54	0.02	0.08	0.19	3.70	5.17	100	a	AB-6202
134	77.90	0.13	12.27	0.00	0.54	0.02	0.08	0.19	3.70	5.17	100	a	AB-6202
135	77.90	0.13	12.27	0.00	0.54	0.02	0.08	0.19	3.70	5.17	100	a	AB-6202
136	77.90	0.13	12.27	0.00	0.54	0.02	0.08	0.19	3.70	5.17	100	a	AB-6202
137	77.90	0.13	12.27	0.00	0.54	0.02	0.08	0.19	3.70	5.17	100	a	AB-6202
138	77.90	0.13	12.27	0.00	0.54	0.02	0.08	0.19	3.70	5.17	100	a	AB-6202
139	77.90	0.13	12.27	0.00	0.54	0.02	0.08	0.19	3.70	5.17	100	a	AB-6202
142	77.90	0.13	12.27	0.00	0.54	0.02	0.08	0.19	3.70	5.17	100	a	AB-6202
143	77.90	0.13	12.27	0.00	0.54	0.02	0.08	0.19	3.70	5.17	100	a	AB-6202
Tshirege bottom	73.83	0.23	10.39	0.00	4.19	0.09	0.01	0.2	5.41	4.46	100	b	JW08-24 (UBT Tshirege 1g)
Tshirege top III	73.83	0.23	10.39	0.00	4.19	0.09	0.01	0.2	5.41	4.46	100	b	JW08-24 (UBT Tshirege 1g)
Tshirege top V	73.83	0.23	10.39	0.00	4.19	0.09	0.01	0.2	5.41	4.46	100	b	JW08-24 (UBT Tshirege 1g)
62-X1	74.75	0.19	10.55	0.00	4.13	0.08	0.00	0.21	5.71	4.38	100		
62-X2	74.75	0.19	10.55	0.00	4.13	0.08	0.00	0.21	5.71	4.38	100		
62-X3	74.75	0.19	10.55	0.00	4.13	0.08	0.00	0.21	5.71	4.38	100		
YS-7 (rim)	76.77	0.07	12.17	0.00	1.46	0.06	0.02	0.54	3.77	5.13	100		
YS-8 (rim)	76.91	0.09	12.11	0.00	1.44	0.09	0.03	0.56	3.68	5.09	100		
Y82	76.56	0.12	12.01	0.00	1.56	0.09	0.02	0.47	4.06	5.10	100		
SP138-2	76.75	0.11	12.01	0.00	1.60	0.04	0.02	0.34	3.86	5.26	100		
BS132	77.57	0.15	12.24	0.01	0.38	0.02	0.02	0.46	3.44	5.72	100		
74Y-180-B	77.07	0.07	12.07	0.00	1.16	0.03	0.00	0.45	3.22	5.93	100	c	LCTA 8YC-413

Table A.4: continued

Sample	Glass - Normalized wt%											Glass Reference (if different) Sample
	SiO2	TiO2	Al2O3	Cr2O3	FeO	MnO	MgO	CaO	Na2O	K2O	TOTAL	
6YC-32	77.07	0.07	12.07	0.00	1.16	0.03	0.00	0.45	3.22	5.93	100	c LCTA 8YC-413
74Y-130-A	77.07	0.07	12.07	0.00	1.16	0.03	0.00	0.45	3.22	5.93	100	c LCTA 8YC-413
8YC-371-A	77.07	0.07	12.07	0.00	1.16	0.03	0.00	0.45	3.22	5.93	100	c LCTA 8YC-413
8YC-401-A	77.07	0.07	12.07	0.00	1.16	0.03	0.00	0.45	3.22	5.93	100	c LCTA 8YC-413
9YC-520-A	77.44	0.10	11.97	0.00	1.24	0.04	0.01	0.44	3.56	5.20	100	c LCTB 8YC-325
7YC-185	77.44	0.10	11.97	0.00	1.24	0.04	0.01	0.44	3.56	5.20	100	c LCTB 8YC-325
8YC-411	77.44	0.10	11.97	0.00	1.24	0.04	0.01	0.44	3.56	5.20	100	c LCTB 8YC-325
6YC-65 (xtl ash)	77.44	0.10	11.97	0.00	1.24	0.04	0.01	0.44	3.56	5.20	100	c LCTB 8YC-325
7YC-325	77.44	0.10	11.97	0.00	1.24	0.04	0.01	0.44	3.56	5.20	100	c LCTB 8YC-325
7YC-315	77.44	0.10	11.97	0.00	1.24	0.04	0.01	0.44	3.56	5.20	100	c LCTB 8YC-325
8YC-408-E	77.44	0.10	11.97	0.00	1.24	0.04	0.01	0.44	3.56	5.20	100	c LCTB 8YC-325
65YR-27-A	77.44	0.10	11.97	0.00	1.24	0.04	0.01	0.44	3.56	5.20	100	c LCTB 8YC-325
9YC-545	77.44	0.10	11.97	0.00	1.24	0.04	0.01	0.44	3.56	5.20	100	c LCTB 8YC-325
9YC-525	77.44	0.10	11.97	0.00	1.24	0.04	0.01	0.44	3.56	5.20	100	c LCTB 8YC-325
6YC-13-B	77.44	0.10	11.97	0.00	1.24	0.04	0.01	0.44	3.56	5.20	100	c LCTB 8YC-325
8YC-455	77.44	0.10	11.97	0.00	1.24	0.04	0.01	0.44	3.56	5.20	100	c LCTB 8YC-325
7YC-321-A	77.44	0.10	11.97	0.00	1.24	0.04	0.01	0.44	3.56	5.20	100	c LCTB 8YC-325
7YC-311-A	77.44	0.10	11.97	0.00	1.24	0.04	0.01	0.44	3.56	5.20	100	c LCTB 8YC-325
8YC-443	77.44	0.10	11.97	0.00	1.24	0.04	0.01	0.44	3.56	5.20	100	c LCTB 8YC-325
9YC-546	77.44	0.10	11.97	0.00	1.24	0.04	0.01	0.44	3.56	5.20	100	c LCTB 8YC-325
6YC-13-E	77.44	0.10	11.97	0.00	1.24	0.04	0.01	0.44	3.56	5.20	100	c LCTB 8YC-325
001-03-1a_cpxrim	77.95	0.11	12.03	0.00	0.59	0.06	0.02	0.46	2.98	5.79	100	
001-03-1c_cpxrim	77.85	0.14	12.18	0.01	0.48	0.00	0.03	0.41	3.34	5.56	100	
001-04_1a_pxrim	77.17	0.08	13.10	0.00	0.40	0.02	0.01	0.74	5.87	2.62	100	
001-04_1d_pxrim	77.83	0.16	12.18	0.00	0.65	0.00	0.01	0.35	3.18	5.64	100	
001-07-1b_cpxrim	78.09	0.16	12.11	0.00	0.40	0.02	0.02	0.39	3.20	5.60	100	
001-07-1d_cpxrim	77.78	0.17	12.25	0.00	0.75	0.03	0.07	0.36	2.79	5.81	100	
001-10-1a_pxrim	78.20	0.15	12.07	0.01	0.45	0.04	0.02	0.51	2.87	5.67	100	
001-10-1c_pxrim	77.92	0.16	12.11	0.01	0.50	0.04	0.02	0.50	2.95	5.79	100	
001-10-1e_pxrim	77.58	0.16	12.07	0.00	0.69	0.00	0.01	0.48	3.29	5.72	100	
001-23-1a_pxrim	78.11	0.15	12.08	0.00	0.31	0.05	0.01	0.39	3.22	5.66	100	
001-23-1c_pxrim	78.07	0.15	12.05	0.00	0.33	0.00	0.02	0.36	3.21	5.81	100	
001-29-1b_pxrim	78.05	0.17	12.09	0.00	0.44	0.06	0.02	0.39	2.91	5.87	100	
001-29-2b_pxrim	77.98	0.17	12.09	0.00	0.38	0.02	0.02	0.38	3.22	5.73	100	
001-30-1a_pxrim	77.92	0.15	12.16	0.00	0.50	0.02	0.01	0.39	2.99	5.86	100	
001-30-2b_pxrim	78.20	0.18	12.10	0.02	0.46	0.01	0.02	0.39	2.60	6.02	100	
001-30-3b_pxrim	77.62	0.14	12.08	0.00	0.91	0.06	0.01	0.41	3.04	5.74	100	
001-30-4a_pxrim	77.94	0.14	12.15	0.00	0.43	0.09	0.02	0.41	3.13	5.70	100	
002-02-1a_pxrim	77.81	0.15	12.14	0.00	0.55	0.03	0.03	0.46	2.92	5.90	100	
002-05-1b_pxrim	77.82	0.18	12.07	0.00	0.42	0.09	0.02	0.46	3.20	5.74	100	

Table A.4: continued

Sample	SiO2	TiO2	Al2O3	Cr2O3	FeO	MnO	MgO	CaO	Na2O	K2O	TOTAL	Glass Reference (if different) Sample
					Glass - Normalized wt%							
002-05-2a_pxrim	77.90	0.13	12.13	0.00	0.46	0.06	0.02	0.50	3.15	5.65	100	
002-13-1a_pxrim	77.83	0.13	12.26	0.01	0.39	0.00	0.02	0.46	3.28	5.63	100	
002-27-1a_pxrim	77.88	0.16	12.13	0.00	0.42	0.04	0.03	0.47	3.24	5.64	100	
002-27-2a_pxrim	77.83	0.16	12.05	0.00	0.54	0.06	0.02	0.46	3.06	5.81	100	
002-28-1b_pxrim	78.00	0.18	12.08	0.00	0.45	0.04	0.02	0.43	3.14	5.67	100	
002-28-1d_pxrim	78.09	0.15	12.15	0.00	0.32	0.09	0.02	0.40	3.03	5.76	100	
002-28-2b_pxrim	78.05	0.20	12.08	0.00	0.33	0.04	0.02	0.35	3.18	5.74	100	
002-31-1a_pxrim	77.99	0.16	12.07	0.00	0.33	0.03	0.03	0.42	3.17	5.80	100	
002-31-1c_pxrim	78.05	0.16	12.06	0.01	0.35	0.04	0.03	0.45	3.15	5.70	100	
002-31-2a_pxrim	78.07	0.15	12.07	0.00	0.40	0.04	0.01	0.45	3.16	5.66	100	
002-34-1b_pxrim	78.03	0.17	12.11	0.00	0.59	0.03	0.01	0.40	2.82	5.82	100	
002-41-1b_pxrim	77.70	0.16	12.05	0.01	0.69	0.00	0.02	0.45	2.99	5.92	100	
002-43-1b_pxrim	78.39	0.15	11.96	0.00	0.46	0.04	0.01	0.30	3.03	5.66	100	
002-43-2b_pxrim	78.07	0.16	12.09	0.00	0.60	0.00	0.02	0.46	2.98	5.61	100	
006-04-1a_pxrim	78.00	0.15	12.05	0.00	0.58	0.00	0.03	0.29	3.12	5.76	100	
006-06-1a_pxrim	76.55	0.15	12.69	0.02	1.08	0.07	0.02	0.38	4.11	4.91	100	
006-06-2a_pxrim	77.56	0.16	11.87	0.01	1.19	0.04	0.02	0.37	3.11	5.66	100	
006-12-1b_pxrim	77.85	0.16	12.01	0.00	0.55	0.02	0.00	0.46	3.12	5.83	100	
006-27-1a_pxrim	78.11	0.15	11.98	0.00	0.46	0.01	0.02	0.46	3.03	5.78	100	
006-35-1b_pxrim	78.16	0.17	12.04	0.01	0.38	0.08	0.03	0.40	3.11	5.62	100	
006-35-2a_pxrim	77.89	0.16	11.99	0.01	0.66	0.02	0.02	0.43	3.13	5.67	100	
006-43-1c_pxrim	78.19	0.15	12.06	0.00	0.40	0.00	0.02	0.35	3.03	5.80	100	
006-44-1c_pxrim	78.11	0.15	12.06	0.01	0.46	0.00	0.02	0.46	3.28	5.46	100	
008-08-1b_pxrim	62.31	0.00	22.60	0.00	0.35	0.02	0.01	4.89	8.31	1.51	100	
008-09-1a_pxrim	78.06	0.18	12.14	0.00	0.44	0.00	0.02	0.44	3.04	5.67	100	
008-09-1c_pxrim	77.55	0.14	12.04	0.00	0.89	0.05	0.01	0.42	3.22	5.68	100	
008-10-1a_pxrim	77.76	0.15	12.10	0.00	0.79	0.03	0.00	0.37	3.02	5.78	100	
008-11-1a_pxrim	78.02	0.15	12.01	0.02	0.36	0.05	0.01	0.39	3.15	5.83	100	
008-12-1b_pxrim	77.63	0.18	12.10	0.00	1.02	0.02	0.08	0.44	2.87	5.66	100	
008-12-2a_pxrim	77.87	0.16	12.03	0.00	0.54	0.02	0.04	0.49	3.01	5.84	100	
008-13-1b_pxrim	77.89	0.15	11.98	0.00	0.68	0.00	0.02	0.42	3.15	5.71	100	
008-19-1b_pxrim	77.37	0.18	11.90	0.00	1.35	0.04	0.00	0.42	3.10	5.64	100	
008-24-1b_pxrim	78.11	0.17	11.95	0.00	0.42	0.02	0.02	0.40	3.16	5.75	100	
008-24-1d_pxrim	78.07	0.17	12.20	0.00	0.41	0.00	0.01	0.40	3.11	5.64	100	
008-25-1a_pxrim	78.23	0.14	12.11	0.00	0.33	0.02	0.03	0.50	2.92	5.73	100	
008-26-1b_pxrim	78.02	0.16	12.01	0.01	0.53	0.00	0.02	0.46	3.11	5.69	100	
008-29-2c_pxrim	77.96	0.20	12.07	0.00	0.39	0.05	0.02	0.39	3.17	5.75	100	
008-29-3a_pxrim	78.08	0.14	12.11	0.00	0.32	0.05	0.02	0.43	3.13	5.72	100	
008-31-1a_pxrim	78.16	0.17	12.01	0.00	0.38	0.00	0.01	0.38	3.17	5.72	100	
008-34-1a_pxrim	77.64	0.15	11.96	0.02	1.08	0.01	0.02	0.41	3.15	5.57	100	

Table A.4: continued

Sample	Glass - Normalized wt%											Glass Reference (if different) Sample
	SiO2	TiO2	Al2O3	Cr2O3	FeO	MnO	MgO	CaO	Na2O	K2O	TOTAL	
008-37-1b_pxrim	78.30	0.14	12.08	0.01	0.29	0.02	0.02	0.35	2.96	5.83	100	
008-37-1d_pxrim	78.14	0.15	12.14	0.00	0.28	0.00	0.02	0.39	3.18	5.69	100	
008-41-1b_pxrim	78.18	0.13	12.19	0.00	0.43	0.01	0.03	0.41	3.09	5.52	100	
008-42-1a_pxrim	78.11	0.14	12.06	0.00	0.41	0.06	0.00	0.37	3.04	5.81	100	
KB-YS-12_1e_rim_1	78.17	0.16	11.73	0.00	0.58	0.00	0.00	0.38	2.89	6.10	100	
KB-YS-12_1e_rim_2	78.07	0.16	11.68	0.00	0.52	0.04	0.00	0.36	3.13	6.05	100	
KB-YS-12_1f_rim_1	78.35	0.15	11.56	0.00	0.48	0.02	0.00	0.27	3.02	6.15	100	
KB-YS-12_1f_rim_2	78.07	0.16	11.52	0.00	0.49	0.04	0.02	0.45	3.16	6.10	100	
KB-YS-12_2f_rim_1	76.01	0.14	11.46	0.02	3.23	0.10	0.12	0.45	2.47	6.00	100	
KB-YS-12_2f_rim_2	78.05	0.16	11.76	0.00	1.11	0.05	0.03	0.46	2.36	6.02	100	
KB-YS-13_1c_rim_1	77.95	0.14	11.94	0.01	0.52	0.00	0.02	0.51	3.06	5.86	100	
KB-YS-13_1c_rim_2	77.92	0.17	11.88	0.02	0.53	0.05	0.01	0.50	3.15	5.78	100	
KB-YS-13_2d_rim_1	77.87	0.17	12.20	0.00	0.41	0.02	0.00	0.44	3.20	5.68	100	
KB-YS-13_2d_rim_2	77.99	0.15	11.95	0.01	0.54	0.06	0.00	0.46	3.06	5.78	100	
KB-YS-13_3a_rim_1	77.63	0.15	12.24	0.00	0.63	0.01	0.01	0.49	2.76	6.08	100	
KB-YS-13_3a_rim_2	77.25	0.12	12.18	0.00	1.21	0.07	0.01	0.45	2.46	6.25	100	

a: Gardner et al., 2014; b: Wilcock et al. 2012; c: Gansecki 1998. If only one glass measurement was published, it was used for all cpx.

APPENDIX B

SUPPLEMENTARY MATERIAL FOR CHAPTER 3

Table B.1: EPMA data: Clinopyroxene

Sample	SiO2	TiO2	Al2O3	Cr2O3	FeO	MnO	MgO	CaO	Na2O	K2O	TOTAL
001-03-1a_cpxrim	51.32	0.18	0.62	0.03	15.54	0.74	11.07	20.12	0.32	0.06	100
001-03-1c_cpxrim	51.53	0.12	0.63	0.00	15.46	0.73	11.14	20.03	0.32	0.02	100
001-04_1a_pxrim	50.69	0.20	0.64	0.00	18.36	0.85	9.82	19.06	0.35	0.02	100
001-04_1d_pxrim	51.61	0.18	0.59	0.00	15.48	0.77	10.97	20.03	0.32	0.04	100
001-07-1b_cpxrim	51.51	0.17	0.67	0.00	15.67	0.76	11.06	19.84	0.28	0.05	100
001-07-1d_cpxrim	51.62	0.18	0.68	0.00	15.47	0.79	11.00	19.88	0.34	0.04	100
001-10-1a_pxrim	51.49	0.15	0.70	0.00	15.54	0.77	11.06	19.99	0.31	0.01	100
001-10-1c_pxrim	51.32	0.17	0.67	0.00	15.43	0.76	11.23	20.04	0.34	0.03	100
001-10-1e_pxrim	51.58	0.17	0.62	0.01	15.01	0.76	11.31	20.16	0.33	0.05	100
001-23-1a_pxrim	51.72	0.20	0.68	0.00	15.41	0.75	11.04	19.81	0.31	0.06	100
001-23-1c_pxrim	51.61	0.17	0.66	0.01	14.99	0.74	11.29	20.19	0.32	0.03	100
001-29-1b_pxrim	51.35	0.15	0.62	0.01	15.53	0.74	11.18	19.99	0.39	0.04	100
001-29-2b_pxrim	51.52	0.18	0.65	0.00	15.33	0.70	11.27	20.01	0.32	0.03	100
001-30-1a_pxrim	51.56	0.16	0.66	0.01	15.06	0.81	11.21	20.19	0.33	0.02	100
001-30-2b_pxrim	51.24	0.17	0.63	0.00	15.72	0.66	11.13	20.07	0.36	0.03	100
001-30-3b_pxrim	51.37	0.17	0.63	0.01	15.70	0.71	11.11	19.97	0.32	0.00	100
001-30-4a_pxrim	51.45	0.21	0.60	0.03	15.14	0.78	11.26	20.18	0.32	0.03	100
002-02-1a_pxrim	51.36	0.18	0.61	0.02	15.15	0.82	11.17	20.30	0.34	0.05	100
002-05-1b_pxrim	51.84	0.20	0.61	0.01	14.64	0.67	11.34	20.34	0.32	0.02	100
002-05-2a_pxrim	51.41	0.19	0.62	0.00	15.52	0.73	11.21	19.95	0.34	0.02	100
002-13-1a_pxrim	51.49	0.17	0.61	0.00	15.33	0.72	11.26	20.02	0.35	0.04	100
002-27-1a_pxrim	51.45	0.21	0.70	0.01	16.08	0.76	11.05	19.38	0.33	0.03	100
002-27-2a_pxrim	51.58	0.17	0.70	0.01	15.10	0.83	11.03	20.27	0.28	0.03	100
002-28-1b_pxrim	51.44	0.16	0.63	0.00	15.18	0.79	11.23	20.20	0.34	0.02	100
002-28-1d_pxrim	51.60	0.17	0.62	0.01	15.12	0.69	11.25	20.18	0.33	0.03	100
002-28-2b_pxrim	51.44	0.14	0.65	0.00	15.10	0.80	11.33	20.20	0.32	0.03	100
002-31-1a_pxrim	51.26	0.18	0.73	0.00	16.41	0.86	10.99	19.19	0.33	0.04	100
002-31-1c_pxrim	51.62	0.13	0.65	0.00	15.33	0.78	11.18	19.95	0.31	0.03	100
002-31-2a_pxrim	51.56	0.17	0.60	0.00	15.37	0.73	11.23	20.03	0.28	0.04	100
002-34-1b_pxrim	51.37	0.16	0.61	0.01	15.81	0.76	10.95	19.95	0.35	0.03	100
002-41-1b_pxrim	51.48	0.18	0.61	0.01	15.66	0.71	10.99	20.00	0.35	0.01	100
002-43-1b_pxrim	51.48	0.16	0.64	0.00	15.49	0.72	11.18	19.95	0.33	0.04	100
002-43-2b_pxrim	51.68	0.20	0.66	0.01	15.49	0.76	11.15	19.73	0.29	0.04	100
006-04-1a_pxrim	51.69	0.16	0.57	0.00	15.28	0.68	11.28	19.96	0.33	0.05	100
006-06-1a_pxrim	51.54	0.18	0.66	0.00	15.45	0.71	11.27	19.88	0.30	0.01	100
006-06-2a_pxrim	51.54	0.17	0.61	0.00	15.41	0.74	11.13	20.07	0.29	0.03	100
006-12-1b_pxrim	51.40	0.18	0.62	0.00	15.64	0.87	11.05	19.93	0.28	0.03	100
006-27-1a_pxrim	51.80	0.16	0.64	0.00	15.11	0.69	11.20	20.02	0.32	0.05	100
006-35-1b_pxrim	51.53	0.21	0.63	0.02	15.37	0.70	11.11	20.08	0.33	0.02	100
006-35-2a_pxrim	51.52	0.18	0.61	0.00	15.61	0.74	11.11	19.92	0.30	0.02	100

Sample	SiO2	TiO2	Al2O3	Cr2O3	FeO	MnO	MgO	CaO	Na2O	K2O	TOTAL
006-43-1c_pxrim	51.80	0.18	0.63	0.01	14.98	0.85	11.28	19.91	0.32	0.04	100
006-44-1c_pxrim	51.74	0.19	0.64	0.00	15.26	0.78	11.09	19.96	0.31	0.03	100
008-08-1b_pxrim	51.11	0.22	0.64	0.00	16.51	0.83	10.73	19.63	0.33	0.00	100
008-09-1a_pxrim	51.26	0.20	0.66	0.01	16.08	0.75	10.94	19.75	0.32	0.03	100
008-09-1c_pxrim	51.51	0.17	0.60	0.01	15.51	0.69	11.09	20.09	0.30	0.03	100
008-10-1a_pxrim	51.63	0.15	0.62	0.00	15.37	0.76	11.05	20.06	0.32	0.04	100
008-11-1a_pxrim	51.64	0.13	0.61	0.00	15.41	0.71	11.25	19.92	0.31	0.02	100
008-12-1b_pxrim	51.35	0.19	0.63	0.01	15.56	0.70	11.17	20.06	0.32	0.02	100
008-12-2a_pxrim	51.23	0.17	0.60	0.00	15.79	0.75	11.09	20.01	0.31	0.05	100
008-13-1b_pxrim	51.58	0.19	0.63	0.00	15.34	0.77	11.13	20.04	0.31	0.01	100
008-19-1b_pxrim	51.38	0.20	0.58	0.02	15.34	0.71	11.25	20.20	0.28	0.04	100
008-24-1b_pxrim	51.52	0.18	0.60	0.01	15.05	0.72	11.42	20.15	0.32	0.03	100
008-24-1d_pxrim	51.32	0.18	0.63	0.00	15.61	0.69	11.37	19.86	0.30	0.02	100
008-25-1a_pxrim	51.53	0.17	0.61	0.00	15.46	0.71	11.09	20.09	0.31	0.02	100
008-26-1b_pxrim	51.55	0.18	0.64	0.00	15.38	0.76	11.14	20.02	0.30	0.03	100
008-29-2c_pxrim	51.74	0.18	0.72	0.01	14.46	0.62	11.79	20.06	0.36	0.05	100
008-29-3a_pxrim	51.53	0.14	0.66	0.00	16.09	0.82	11.19	19.22	0.32	0.03	100
008-31-1a_pxrim	51.33	0.15	0.64	0.00	16.01	0.79	11.12	19.61	0.34	0.01	100
008-34-1a_pxrim	51.63	0.19	0.59	0.00	15.05	0.71	11.29	20.16	0.34	0.04	100
008-37-1b_pxrim	51.52	0.15	0.60	0.03	15.49	0.66	11.13	20.07	0.32	0.04	100
008-37-1d_pxrim	51.46	0.15	0.66	0.00	15.30	0.72	11.27	20.10	0.31	0.03	100
008-41-1b_pxrim	51.57	0.18	0.63	0.00	15.10	0.80	11.22	20.14	0.32	0.04	100
008-42-1a_pxrim	51.56	0.19	0.66	0.01	15.77	0.76	11.02	19.69	0.32	0.03	100
KB-YS-12_1e_rim_1	51.90	0.15	0.63	0.00	15.33	0.72	10.85	20.09	0.31	0.02	100
KB-YS-12_1e_rim_2	51.84	0.19	0.72	0.00	15.20	0.73	10.81	20.23	0.26	0.00	100
KB-YS-12_1f_rim_1	51.68	0.21	0.68	0.00	15.74	0.76	10.83	19.78	0.30	0.02	100
KB-YS-12_1f_rim_2	52.32	0.22	0.68	0.00	14.92	0.72	10.92	19.94	0.27	0.01	100
KB-YS-12_2f_rim_1	51.68	0.12	0.64	0.00	15.04	0.71	11.42	20.06	0.31	0.02	100
KB-YS-12_2f_rim_2	51.89	0.19	0.63	0.00	14.79	0.72	11.29	20.18	0.28	0.03	100
KB-YS-13_1c_rim_1	52.32	0.18	0.68	0.01	14.58	0.79	11.23	19.86	0.32	0.05	TOTAL
KB-YS-13_1c_rim_2	52.03	0.19	0.72	0.00	14.74	0.73	11.19	20.04	0.29	0.06	100
KB-YS-13_2d_rim_1	51.92	0.18	0.68	0.02	14.95	0.66	11.27	19.99	0.30	0.02	100
KB-YS-13_2d_rim_2	52.06	0.18	0.69	0.00	14.82	0.75	11.15	19.99	0.33	0.03	100
KB-YS-13_3a_rim_1	52.02	0.16	0.68	0.00	15.53	0.80	10.76	19.75	0.29	0.01	100
KB-YS-13_3a_rim_2	52.02	0.18	0.66	0.00	15.53	0.79	10.77	19.74	0.28	0.02	100
001-03-1e_cpxcore	50.36	0.17	0.58	0.00	19.74	0.99	9.11	18.73	0.32	0.01	100
001-07-1a_cpxcore	50.22	0.21	0.64	0.01	19.91	1.04	8.94	18.66	0.33	0.02	100
001-07-1a_cpxcore	50.44	0.18	0.62	0.03	19.66	0.96	8.94	18.84	0.31	0.01	100
001-18-1a_pxcore	50.26	0.21	0.58	0.00	20.40	1.05	8.71	18.46	0.32	0.01	100
001-29-1a_pxcore	50.40	0.19	0.58	0.00	19.53	0.94	9.20	18.83	0.30	0.03	100

Sample	SiO2	TiO2	Al2O3	Cr2O3	FeO	MnO	MgO	CaO	Na2O	K2O	TOTAL
001-29-2a_pxcore	50.26	0.19	0.57	0.00	19.94	1.00	8.91	18.82	0.31	0.00	100
001-30-2a_pxcore	50.20	0.20	0.59	0.01	19.90	0.95	8.89	18.92	0.32	0.03	100
001-30-3a_pxcore	50.37	0.21	0.62	0.01	18.92	0.92	9.60	19.04	0.29	0.02	100
002-05-1a_pxcore	50.57	0.19	0.61	0.02	18.57	0.98	9.76	18.97	0.32	0.02	100
002-16-1a_pxcore	50.43	0.21	0.57	0.00	19.72	0.96	9.17	18.59	0.30	0.04	100
002-28-1a_pxcore	50.30	0.16	0.54	0.01	20.35	1.02	8.67	18.63	0.30	0.01	100
002-28-2a_pxcore	50.47	0.20	0.54	0.00	18.82	0.94	9.70	18.98	0.32	0.01	100
002-41-1a_pxcore	50.40	0.17	0.56	0.00	19.47	0.96	9.38	18.73	0.31	0.01	100
002-43-1a_pxcore	50.54	0.17	0.55	0.02	19.73	0.95	9.13	18.56	0.32	0.03	100
002-43-2a_pxcore	50.46	0.21	0.57	0.00	19.83	1.07	8.94	18.58	0.31	0.02	100
006-04-1c_cpxcore	51.22	0.19	0.60	0.00	16.64	0.78	10.63	19.62	0.31	0.01	100
006-04-1d_cpxcorecore	51.35	0.18	0.61	0.00	15.74	0.78	11.10	19.92	0.31	0.02	100
006-04-1e_cpxcorecorecore	51.37	0.15	0.59	0.00	15.73	0.71	11.12	20.00	0.30	0.02	100
006-12-1a_pxcore	50.16	0.21	0.60	0.00	20.60	1.05	8.56	18.49	0.33	0.00	100
006-43-1a_pxcore	50.19	0.17	0.54	0.00	20.74	1.07	8.68	18.29	0.31	0.00	100
006-44-1a_pxcore	50.25	0.21	0.55	0.00	20.34	0.96	8.89	18.48	0.32	0.01	100
006-44-1b_pxcorecore	51.28	0.16	0.61	0.00	16.56	0.82	10.66	19.58	0.32	0.01	100
008-08-1a_pxcore	50.20	0.22	0.56	0.00	20.98	1.07	8.46	18.23	0.28	0.00	100
008-12-1a_pxcore	50.52	0.22	0.56	0.00	19.15	0.86	9.64	18.69	0.35	0.00	100
008-13-1a_pxcore	50.36	0.19	0.58	0.00	20.24	1.03	8.83	18.45	0.29	0.03	100
008-19-1a_pxcore	50.46	0.18	0.60	0.00	19.21	0.98	9.46	18.76	0.34	0.00	100
008-24-1a_pxcore	51.35	0.40	1.30	0.02	13.08	0.66	12.57	20.29	0.33	0.01	100
008-26-1a_pxcore	52.93	0.21	0.72	0.00	9.00	0.39	14.70	21.64	0.41	0.00	100
008-26-1b_pxrim	51.55	0.18	0.64	0.00	15.38	0.76	11.14	20.02	0.30	0.03	100
008-29-2c_pxrim	51.74	0.18	0.72	0.01	14.46	0.62	11.79	20.06	0.36	0.05	100
008-29-3a_pxrim	51.53	0.14	0.66	0.00	16.09	0.82	11.19	19.22	0.32	0.03	100
008-31-1a_pxrim	51.33	0.15	0.64	0.00	16.01	0.79	11.12	19.61	0.34	0.01	100
008-34-1a_pxrim	51.63	0.19	0.59	0.00	15.05	0.71	11.29	20.16	0.34	0.04	100
008-37-1a_pxcore	50.20	0.21	0.56	0.00	20.76	1.09	8.57	18.31	0.29	0.00	100
008-41-1a_pxcore	50.77	0.19	0.59	0.00	19.02	0.86	9.46	18.83	0.28	0.01	100
KB-YS-12_1b_core	51.61	0.18	0.62	0.00	16.71	0.87	10.38	19.31	0.29	0.02	100
KB-YS-12_1c_core_1	51.37	0.17	0.61	0.01	18.08	0.95	9.69	18.81	0.28	0.02	100
KB-YS-12_1c_core_2	51.23	0.22	0.62	0.01	17.90	0.94	9.87	18.88	0.32	0.00	100
KB-YS-12_1d_core	51.59	0.17	0.64	0.00	17.19	0.83	10.00	19.29	0.28	0.00	100
KB-YS-12_1e_core	51.17	0.18	0.59	0.00	18.46	0.93	9.61	18.71	0.31	0.03	100
KB-YS-12_1f_core	50.87	0.17	0.59	0.01	19.21	0.99	9.28	18.59	0.30	0.01	100
KB-YS-12_2a_core	51.57	0.21	0.63	0.01	15.85	0.78	10.74	19.88	0.30	0.02	100
KB-YS-12_2c_core_1	50.90	0.21	0.60	0.01	18.69	0.90	9.56	18.83	0.29	0.01	100
KB-YS-12_2c_core_2	51.38	0.18	0.65	0.01	17.34	0.91	9.94	19.27	0.28	0.04	100
KB-YS-12_2f_core	50.86	0.23	0.61	0.00	19.76	0.94	8.79	18.55	0.26	0.01	100

B.1: continued

Sample	SiO2	TiO2	Al2O3	Cr2O3	FeO	MnO	MgO	CaO	Na2O	K2O	TOTAL
KB-YS-12_3d_core	51.52	0.18	0.65	0.03	16.55	0.76	10.42	19.58	0.31	0.00	100
KB-YS-12_3g_core	51.03	0.20	0.70	0.03	18.89	0.98	9.20	18.66	0.29	0.02	100
KB-YS-12_4b_core	51.05	0.18	0.59	0.01	19.07	0.94	9.08	18.75	0.33	0.00	100
KB-YS-12_4c_core	51.33	0.20	0.64	0.02	17.48	0.89	9.95	19.20	0.27	0.02	100
KB-YS-12_4d_core	50.80	0.20	0.55	0.00	20.29	1.03	8.48	18.36	0.28	0.01	100
KB-YS-13_1c_core	51.85	0.16	0.64	0.01	16.12	0.84	10.57	19.53	0.27	0.00	100
KB-YS-13_1d_core	51.94	0.21	0.67	0.00	15.50	0.82	10.87	19.70	0.28	0.01	100
KB-YS-13_1e_core	51.95	0.18	0.79	0.00	16.36	0.81	10.20	19.42	0.28	0.01	100
KB-YS-13_1h_core	51.34	0.25	0.77	0.01	17.67	0.93	9.88	18.84	0.29	0.01	100
KB-YS-13_2a_core	52.09	0.18	0.68	0.00	15.49	0.79	10.92	19.55	0.29	0.00	100
KB-YS-13_2b_core	51.58	0.22	0.62	0.00	16.61	0.89	10.42	19.35	0.29	0.02	100
KB-YS-13_2d_core	51.07	0.21	0.57	0.00	18.87	0.95	9.29	18.79	0.26	0.00	100
KB-YS-13_2e_core	51.31	0.19	0.60	0.01	17.74	0.94	10.03	18.87	0.31	0.00	100
KB-YS-13_2g_core	51.43	0.22	0.61	0.01	16.52	0.92	10.56	19.43	0.29	0.02	100
KB-YS-13_3a_core	51.71	0.18	0.66	0.00	16.05	0.84	10.67	19.59	0.28	0.02	100
KB-YS-13_3f_core	51.53	0.19	0.58	0.01	16.32	0.75	10.52	19.84	0.25	0.01	100
KB-YS-13_3g_core	51.92	0.14	0.57	0.01	16.62	0.97	10.06	19.42	0.28	0.02	100
KB-YS-13_4b_core	51.27	0.21	0.71	0.00	18.38	1.03	9.36	18.71	0.29	0.03	100
KB-YS-13_4c_core	52.03	0.27	0.79	0.00	14.94	0.74	11.32	19.64	0.28	0.00	100
KB-YS-13_4g_core	50.93	0.21	0.59	0.00	19.44	1.02	8.82	18.70	0.27	0.02	100
KB-YS-13_4h_core	51.53	0.24	0.80	0.00	16.06	0.91	10.93	19.22	0.30	0.02	100
KB-YS-13_4j_core	50.66	0.21	0.55	0.00	19.95	1.08	8.80	18.42	0.32	0.00	100

Table B.2: EPMA data: Liquid

Sample	SiO2	TiO2	Al2O3	Cr2O3	FeO	MnO	MgO	CaO	Na2O	K2O	TOTAL
001-03-1a_cpxrim	77.95	0.11	12.03	0.00	0.59	0.06	0.02	0.46	2.98	5.79	100
001-03-1c_cpxrim	77.85	0.14	12.18	0.01	0.48	0.00	0.03	0.41	3.34	5.56	100
001-04_1a_pxrim	77.17	0.08	13.10	0.00	0.40	0.02	0.01	0.74	5.87	2.62	100
001-04_1d_pxrim	77.83	0.16	12.18	0.00	0.65	0.00	0.01	0.35	3.18	5.64	100
001-07-1b_cpxrim	78.09	0.16	12.11	0.00	0.40	0.02	0.02	0.39	3.20	5.60	100
001-07-1d_cpxrim	77.78	0.17	12.25	0.00	0.75	0.03	0.07	0.36	2.79	5.81	100
001-10-1a_pxrim	78.20	0.15	12.07	0.01	0.45	0.04	0.02	0.51	2.87	5.67	100
001-10-1c_pxrim	77.92	0.16	12.11	0.01	0.50	0.04	0.02	0.50	2.95	5.79	100
001-10-1e_pxrim	77.58	0.16	12.07	0.00	0.69	0.00	0.01	0.48	3.29	5.72	100
001-23-1a_pxrim	78.11	0.15	12.08	0.00	0.31	0.05	0.01	0.39	3.22	5.66	100
001-23-1c_pxrim	78.07	0.15	12.05	0.00	0.33	0.00	0.02	0.36	3.21	5.81	100
001-29-1b_pxrim	78.05	0.17	12.09	0.00	0.44	0.06	0.02	0.39	2.91	5.87	100
001-29-2b_pxrim	77.98	0.17	12.09	0.00	0.38	0.02	0.02	0.38	3.22	5.73	100
001-30-1a_pxrim	77.92	0.15	12.16	0.00	0.50	0.02	0.01	0.39	2.99	5.86	100
001-30-2b_pxrim	78.20	0.18	12.10	0.02	0.46	0.01	0.02	0.39	2.60	6.02	100
001-30-3b_pxrim	77.62	0.14	12.08	0.00	0.91	0.06	0.01	0.41	3.04	5.74	100
001-30-4a_pxrim	77.94	0.14	12.15	0.00	0.43	0.09	0.02	0.41	3.13	5.70	100
002-02-1a_pxrim	77.81	0.15	12.14	0.00	0.55	0.03	0.03	0.46	2.92	5.90	100
002-05-1b_pxrim	77.82	0.18	12.07	0.00	0.42	0.09	0.02	0.46	3.20	5.74	100
002-05-2a_pxrim	77.90	0.13	12.13	0.00	0.46	0.06	0.02	0.50	3.15	5.65	100
002-13-1a_pxrim	77.83	0.13	12.26	0.01	0.39	0.00	0.02	0.46	3.28	5.63	100
002-27-1a_pxrim	77.88	0.16	12.13	0.00	0.42	0.04	0.03	0.47	3.24	5.64	100
002-27-2a_pxrim	77.83	0.16	12.05	0.00	0.54	0.06	0.02	0.46	3.06	5.81	100
002-28-1b_pxrim	78.00	0.18	12.08	0.00	0.45	0.04	0.02	0.43	3.14	5.67	100
002-28-1d_pxrim	78.09	0.15	12.15	0.00	0.32	0.09	0.02	0.40	3.03	5.76	100
002-28-2b_pxrim	78.05	0.20	12.08	0.00	0.33	0.04	0.02	0.35	3.18	5.74	100
002-31-1a_pxrim	77.99	0.16	12.07	0.00	0.33	0.03	0.03	0.42	3.17	5.80	100
002-31-1c_pxrim	78.05	0.16	12.06	0.01	0.35	0.04	0.03	0.45	3.15	5.70	100
002-31-2a_pxrim	78.07	0.15	12.07	0.00	0.40	0.04	0.01	0.45	3.16	5.66	100
002-34-1b_pxrim	78.03	0.17	12.11	0.00	0.59	0.03	0.01	0.40	2.82	5.82	100
002-41-1b_pxrim	77.70	0.16	12.05	0.01	0.69	0.00	0.02	0.45	2.99	5.92	100
002-43-1b_pxrim	78.39	0.15	11.96	0.00	0.46	0.04	0.01	0.30	3.03	5.66	100
002-43-2b_pxrim	78.07	0.16	12.09	0.00	0.60	0.00	0.02	0.46	2.98	5.61	100
006-04-1a_pxrim	78.00	0.15	12.05	0.00	0.58	0.00	0.03	0.29	3.12	5.76	100
006-06-1a_pxrim	76.55	0.15	12.69	0.02	1.08	0.07	0.02	0.38	4.11	4.91	100
006-06-2a_pxrim	77.56	0.16	11.87	0.01	1.19	0.04	0.02	0.37	3.11	5.66	100
006-12-1b_pxrim	77.85	0.16	12.01	0.00	0.55	0.02	0.00	0.46	3.12	5.83	100
006-27-1a_pxrim	78.11	0.15	11.98	0.00	0.46	0.01	0.02	0.46	3.03	5.78	100
006-35-1b_pxrim	78.16	0.17	12.04	0.01	0.38	0.08	0.03	0.40	3.11	5.62	100
006-35-2a_pxrim	77.89	0.16	11.99	0.01	0.66	0.02	0.02	0.43	3.13	5.67	100

B.2: continued

Sample	SiO2	TiO2	Al2O3	Cr2O3	FeO	MnO	MgO	CaO	Na2O	K2O	TOTAL
006-43-1c_pxrim	78.19	0.15	12.06	0.00	0.40	0.00	0.02	0.35	3.03	5.80	100
006-44-1c_pxrim	78.11	0.15	12.06	0.01	0.46	0.00	0.02	0.46	3.28	5.46	100
008-08-1b_pxrim	62.31	0.00	22.60	0.00	0.35	0.02	0.01	4.89	8.31	1.51	100
008-09-1a_pxrim	78.06	0.18	12.14	0.00	0.44	0.00	0.02	0.44	3.04	5.67	100
008-09-1c_pxrim	77.55	0.14	12.04	0.00	0.89	0.05	0.01	0.42	3.22	5.68	100
008-10-1a_pxrim	77.76	0.15	12.10	0.00	0.79	0.03	0.00	0.37	3.02	5.78	100
008-11-1a_pxrim	78.02	0.15	12.01	0.02	0.36	0.05	0.01	0.39	3.15	5.83	100
008-12-1b_pxrim	77.63	0.18	12.10	0.00	1.02	0.02	0.08	0.44	2.87	5.66	100
008-12-2a_pxrim	77.87	0.16	12.03	0.00	0.54	0.02	0.04	0.49	3.01	5.84	100
008-13-1b_pxrim	77.89	0.15	11.98	0.00	0.68	0.00	0.02	0.42	3.15	5.71	100
008-19-1b_pxrim	77.37	0.18	11.90	0.00	1.35	0.04	0.00	0.42	3.10	5.64	100
008-24-1b_pxrim	78.11	0.17	11.95	0.00	0.42	0.02	0.02	0.40	3.16	5.75	100
008-24-1d_pxrim	78.07	0.17	12.20	0.00	0.41	0.00	0.01	0.40	3.11	5.64	100
008-25-1a_pxrim	78.23	0.14	12.11	0.00	0.33	0.02	0.03	0.50	2.92	5.73	100
008-26-1b_pxrim	78.02	0.16	12.01	0.01	0.53	0.00	0.02	0.46	3.11	5.69	100
008-29-2c_pxrim	77.96	0.20	12.07	0.00	0.39	0.05	0.02	0.39	3.17	5.75	100
008-29-3a_pxrim	78.08	0.14	12.11	0.00	0.32	0.05	0.02	0.43	3.13	5.72	100
008-31-1a_pxrim	78.16	0.17	12.01	0.00	0.38	0.00	0.01	0.38	3.17	5.72	100
008-34-1a_pxrim	77.64	0.15	11.96	0.02	1.08	0.01	0.02	0.41	3.15	5.57	100
008-37-1b_pxrim	78.30	0.14	12.08	0.01	0.29	0.02	0.02	0.35	2.96	5.83	100
008-37-1d_pxrim	78.14	0.15	12.14	0.00	0.28	0.00	0.02	0.39	3.18	5.69	100
008-41-1b_pxrim	78.18	0.13	12.19	0.00	0.43	0.01	0.03	0.41	3.09	5.52	100
008-42-1a_pxrim	78.11	0.14	12.06	0.00	0.41	0.06	0.00	0.37	3.04	5.81	100
KB-YS-12_1e_rim_1	78.17	0.16	11.73	0.00	0.58	0.00	0.00	0.38	2.89	6.10	100
KB-YS-12_1e_rim_2	78.07	0.16	11.68	0.00	0.52	0.04	0.00	0.36	3.13	6.05	100
KB-YS-12_1f_rim_1	78.35	0.15	11.56	0.00	0.48	0.02	0.00	0.27	3.02	6.15	100
KB-YS-12_1f_rim_2	78.07	0.16	11.52	0.00	0.49	0.04	0.02	0.45	3.16	6.10	100
KB-YS-12_2f_rim_1	76.01	0.14	11.46	0.02	3.23	0.10	0.12	0.45	2.47	6.00	100
KB-YS-12_2f_rim_2	78.05	0.16	11.76	0.00	1.11	0.05	0.03	0.46	2.36	6.02	100
KB-YS-13_1c_rim_1	77.95	0.14	11.94	0.01	0.52	0.00	0.02	0.51	3.06	5.86	100
KB-YS-13_1c_rim_2	77.92	0.17	11.88	0.02	0.53	0.05	0.01	0.50	3.15	5.78	100
KB-YS-13_2d_rim_1	77.87	0.17	12.20	0.00	0.41	0.02	0.00	0.44	3.20	5.68	100
KB-YS-13_2d_rim_2	77.99	0.15	11.95	0.01	0.54	0.06	0.00	0.46	3.06	5.78	100
KB-YS-13_3a_rim_1	77.63	0.15	12.24	0.00	0.63	0.01	0.01	0.49	2.76	6.08	100
KB-YS-13_3a_rim_2	77.25	0.12	12.18	0.00	1.21	0.07	0.01	0.45	2.46	6.25	100